



Modeling of Particle Thermal Energy Reservoir for Solar Industrial Process Heat: Final Technical Report

Zhiwen Ma, Jeffery Gifford, Loiy Al-Ghussain, and Janna Martinek

National Renewable Energy Laboratory

**NREL is a national laboratory of the U.S. Department of Energy
Office of Energy Efficiency & Renewable Energy
Operated by the Alliance for Sustainable Energy, LLC**

This report is available at no cost from the National Renewable Energy Laboratory (NREL) at www.nrel.gov/publications.

Contract No. DE-AC36-08GO28308

Technical Report
NREL/TP-5700-86816
September 2023



Modeling of Particle Thermal Energy Reservoir for Solar Industrial Process Heat: Final Technical Report

Zhiwen Ma, Jeffrey Gifford, Loiy Al-Ghussain, and Janna Martinek

National Renewable Energy Laboratory

Suggested Citation

Ma, Zhiwen, Jeffrey Gifford, Loiy Al-Ghussain, and Janna Martinek. 2023. *Modeling of Particle Thermal Energy Reservoir for Solar Industrial Process Heat: Final Technical Report*. Golden, CO: National Renewable Energy Laboratory. NREL/TP-5700-86816. <https://www.nrel.gov/docs/fy23osti/86816.pdf>.

**NREL is a national laboratory of the U.S. Department of Energy
Office of Energy Efficiency & Renewable Energy
Operated by the Alliance for Sustainable Energy, LLC**

This report is available at no cost from the National Renewable Energy Laboratory (NREL) at www.nrel.gov/publications.

Contract No. DE-AC36-08GO28308

Technical Report
NREL/TP-5700-86816
September 2023

National Renewable Energy Laboratory
15013 Denver West Parkway
Golden, CO 80401
303-275-3000 • www.nrel.gov

NOTICE

This work was authored by the National Renewable Energy Laboratory, operated by Alliance for Sustainable Energy, LLC, for the U.S. Department of Energy (DOE) under Contract No. DE-AC36-08GO28308. Funding provided by the U.S. Department of Energy Office of Energy Efficiency and Renewable Energy Solar Energy Technologies Office. The views expressed herein do not necessarily represent the views of the DOE or the U.S. Government.

This report is available at no cost from the National Renewable Energy Laboratory (NREL) at www.nrel.gov/publications.

U.S. Department of Energy (DOE) reports produced after 1991 and a growing number of pre-1991 documents are available free via www.OSTI.gov.

Cover Photos by Dennis Schroeder: (clockwise, left to right) NREL 51934, NREL 45897, NREL 42160, NREL 45891, NREL 48097, NREL 46526.

NREL prints on paper that contains recycled content.

Acknowledgement

This work was authored by the National Renewable Energy Laboratory (NREL), operated by Alliance for Sustainable Energy, LLC, for the U.S. Department of Energy (DOE) under Contract No. DE-AC36-08GO28308. This material is based upon work supported by the U.S. Department of Energy's Office of Energy Efficiency and Renewable Energy (EERE) under the Solar Energy Technologies Office Award Number 38394. We also acknowledge the support from the Office of Technology Transitions through the Technology Commercialization Fund (TCF) under project number TCF-21-24775.

We thank our industry collaborators including Alumina Energy, Babcock & Wilcox, and Modelon for their support. We also appreciate the technical inputs from NREL colleagues, William Hamilton and Jing Wang, for the modeling tool development. Finally, we are grateful for the manuscript reviews by Mr. Timothy Fuller, Thomas Flynn, Ty Neises, and the editing efforts by Deanna Cook, Mike Meshek, and Patrick Hayes of the NREL Communications Office.

List of Acronyms

CFD	computational fluid dynamics
CSP	concentrating solar power
CST	concentrating solar thermal
DNI	direct normal irradiation
DOE	U.S. Department of Energy
FEA	finite element analysis
GRG	generalized reduced gradient
ENDURING	Economic Long-Duration Electricity Storage by Using Low-Cost Thermal Energy Storage and High-Efficiency Power Cycle
HEATER	Heat Exchanger and Thermal Energy Reservoir
HX	heat exchanger
LCOH	levelized cost of heat
LMP	locational marginal price
MfiX	Multiphase Flow with Interphase eXchanges
PFB	pressurized fluidized bed
PPA	power purchase agreement
PV	photovoltaics
ROM	reduced-order model
SAM	System Advisor Model
SIPH	solar industrial process heat
SVM	Searles Valley Minerals, Inc.
TES	thermal energy storage
TMY	typical meteorological year
USD	U.S. dollars

Executive Summary

Industrial process heat is a leading source of carbon emissions in the United States. To achieve decarbonization goals and reduce costs, solar industrial process heat (SIPH) systems have been investigated as a means of providing a carbon-free heat supply. Particle thermal energy storage (TES) could supplement solar resources (i.e., concentrating solar thermal and photovoltaics) to enable a high capacity factor (> 90%), carbon-free heat source. Particle TES has been considered due to its low-cost storage medium and capability to support a wide range of temperatures. This report provides technical details of developing a component and system modeling tool for a unique particle TES platform to assist the adoption of SIPH technology.

The system modeling platform was developed in the Modelica-based Modelon Impact software. Modelica is base software of modeling language that is acausal and object-oriented. These features of the language are useful in the development of a highly flexible and adaptable tool that are needed to accommodate the wide range of potential industrial process heat applications. A SIPH model with a particle TES modeling library was created that contains new component models that were validated against high-fidelity models and/or industry partner data. After the component model development, integrated system models were built with real-time system controllers that enable transient, annual simulations. These simulations are useful for analyzing system performance, configurations, and operations as well as observing nuanced transients. The system models were wrapped with Python program by exporting a functional mock-up unit. The Python program enables (1) integration of the Modelica-based performance model with other tools (e.g., the SolarPILOT and System Advisor Model financial models) and component cost functions and (2) sensitivity analysis and techno-economic analysis.

The cost functions for the SIPH system were developed as part of the techno-economic analysis for this project. This analysis optimally sized the SIPH system for a specific use case and six system design scenarios encompassing various combinations of concentrating solar thermal, photovoltaic, and grid electricity. The analysis investigated possible conditions to achieve a levelized cost of heat that could be competitive to that of natural gas. The project included sensitivity analysis to solar capital costs, average grid prices, and grid backup independence parameters.

The technical work explored SIPH configurations and applications to understand design factors and system configurations relevant to particle TES through the development and use of simulation and analysis tools. The modeling tools aim to assist the design of SIPH systems and to assess techno-economic potentials for decarbonizing industrial processes.

Table of Contents

1	Introduction	1
1.1	Project Goals.....	2
1.2	Modeling Tool Architecture and Solver Introduction.....	3
1.3	Report Organization.....	6
2	Component Model Development and Validation	7
2.1	Electric Particle Heater	7
2.1.1	Modeling Approach	7
2.1.2	Validation.....	9
2.2	Solar Particle Receiver and SolarPILOT Integration.....	10
2.2.1	Modeling Approach	10
2.2.2	Modelon Impact Model Validation.....	14
2.3	Particle Storage Silo.....	16
2.3.1	Storage Modeling Approach	16
2.3.2	Validation.....	19
2.4	Particle-Air, Pressurized, Fluidized Bed Heat Exchanger (PFB HX).....	21
2.4.1	Modeling Approach	21
2.4.2	Validation.....	25
2.5	Particle Steam Generator	25
2.5.1	Modeling Approach	25
2.5.2	Validation.....	27
3	SIPH Applications and System Modeling	29
3.1	SIPH Applications and System Configurations	29
3.2	System Simulation	31
4	Techno-Economic Analysis and Case Study of HEATER System Configurations	34
4.1	Cost Analysis Method.....	35
4.1.1	Component Cost and Operating Cost Assumptions.....	35
4.1.2	Annual Performance Analysis	37
4.1.3	Component Size Selection	39
4.2	Cost Uncertainties and Sensitivity Analysis	40
4.3	Case Study and Techno-Economic Analysis Results.....	40
4.4	Model Integration.....	44
5	Conclusion	49
6	References	50
Appendix SIPH Case Studies		52
A.1.	Case Definitions.....	52
A.1.1.	Bauxite Calcination (CS1)	52
A.1.2.	Industry Hot Air Supply (CS2)	52
A.1.3.	Cogeneration (CS4).....	53
A.2.	Parametric Sensitivity Ranges	54
A.3.	Results.....	54
A.3.1.	CS1: Bauxite Calcination.....	54
A.3.2.	CS2: Industrial Hot Air Supply.....	58
A.3.3.	CS4: Cogeneration	61

List of Figures

Figure 1. Comparison of industrial process heat where TES eliminates thermal energy conversion: Less complexity, equipment cost, efficiency losses.....	1
Figure 2. Diagram of supplying industrial process heat with solar energy sources with particle TES.....	2
Figure 3. Software architecture for component modules and HEATER system models.....	4
Figure 4. Modelon Impact interface and major functional menus.....	5
Figure 5. Modelon Impact’s compiler generates system of equations automatically for solver.....	5
Figure 6. Summary of component model library developed and validation procedure in this project.....	7
Figure 7. Geometry representation (a), simple test model (b), and mathematical energy balance on a discretized volume for particle heater (c).....	8
Figure 8. Comparison of 1D temperature profiles predicted by the high-fidelity MFiX and Modelon Impact-based ROM of the electric particle heater at two different surface angles (θ) and friction coefficients (μ).....	10
Figure 9. Receiver model composition (a) and its icon representation in Modelon Impact (b).....	10
Figure 10. Diagram of the receiver model connected with a heliostat field model in Modelon Impact.....	12
Figure 11. An initial result of the receiver model for a summer day test run.....	13
Figure 12. Software framework of the integration of Modelon Impact and SolarPILOT (Graphic by NREL).....	13
Figure 13. Solar field efficiency determined by SolarPILOT as a function of solar azimuth and elevation angles for a 100-MWth field in Denver, Colorado.....	15
Figure 14. Comparison of absolute field efficiency error as a function of elevation angle using the linear and Akima spline interpolation methods.....	15
Figure 15. Graphical representation of the mathematical description of both the volume and insulation model that comprise a single containment model.....	17
Figure 16. Fully packaged particle storage array model with connection points (class) and individual components and structure that comprise the particle storage array model (subclass).....	20
Figure 17. T^* of the particle storage silo over a 7-day cooling process.....	20
Figure 18. PFB HX concept developed at NREL (a) and computational fluid dynamics (CFD) model of the PFB HX concept design (b).....	22
Figure 19. Comparison of (a) gas-phase bed pressure drop and (b) effectiveness predicted by high-fidelity CFD and Modelon Impact-based models of the PFB HX with 10% error bars.....	25
Figure 20. Top-level steam generator model (left) and structure of the component model (right).....	26
Figure 21. Illustration of a design of a particle steam generator from Babcock & Wilcox, which provided validated data.....	27
Figure 22. Babcock & Wilcox design steam temperature versus modeled steam temperature in Modelon Impact.....	28
Figure 23. Four charging configurations of hybridizing CST and PV (or grid power) through solar receiver and electric charging particle heater.....	30
Figure 24. Discharge stored energy to (a) hot particles, (b) hot air, and (c) hot water or steam in various industry uses conditions.....	30
Figure 25. Industrial steam generation (a) system diagram and (b) system model in Modelon Impact.....	31
Figure 26. Results produced by the steam generation Modelon Impact system modeling tool for a system with 24-hr (blue) and 100-hr (yellow) storage durations: (a) nominal solar input over a 14- day window of an annual simulation (same for both cases), (b) nominal storage level across the entire year, and (c) cumulative hours of time where backup (i.e., grid heating or fossil fuels) would be required to meet constant load demand.....	32
Figure 27. Base case grid electricity price signal (\$/MWh).....	37
Figure 28. Sensitivity of LCOH to CSP, TES, and PV sizing for (a) base case cost assumptions and (b) reduced PV capital cost (570 \$/kWe).....	42

Figure 29. Cost breakdown of optimal CSP/ TES (Scenario 4) SIPH subsystems required for industrial steam supply case study	43
Figure 30. Monthly thermal energy delivered by the energy sources in the optimal CSP/ TES (Scenario 4) SIPH system designed for industrial steam supply case study.....	43
Figure 31. Potential reduction in the LCOH of the optimal CSP/ TES (Scenario 4) SIPH system designed for industrial steam supply case study	44
Figure 32. Sensitivity of the LCOH of the optimal CSP/ TES (Scenario 4) SIPH system designed for industrial steam supply case study to the variation in main economic parameters	44
Figure 33. System analysis flow chart for enhancing system modeling capabilities	45
Figure 34. Example of results from the Modelica annual performance model run through the Python framework in Figure 33 with the system sizing from Scenario 4 in Table 13	46
Figure 35. Example of sensitivity analysis using similar cost inputs as shown in Figure 28(b): (a) simplified annual analysis and LCOH calculation as shown in Section 4.1, (b) simplified annual analysis and LCOH from the SAM Single Owner financial model, and (c) Modelica annual performance analysis and LCOH from the SAM Single Owner financial model	47
Figure 36. Example of optimization results using the same models and conditions as Fig. 35(c)	48
Figure A-1. Cost breakdown of optimal CSP/ TES (Scenario 2) SIPH subsystems required for bauxite calcination case study.....	55
Figure A-2. Monthly thermal energy delivered by the energy sources in the optimal CSP/ TES (Scenario 2) SIPH system designed for bauxite calcination case study	55
Figure A-3. Potential reduction in the LCOH of the optimal CSP/ TES (Scenario 2) SIPH system designed for bauxite calcination case study	56
Figure A-4. Sensitivity of the LCOH of the optimal CSP/ TES (Scenario 2) SIPH system designed for bauxite calcination case study to the variation in main economic parameters.....	57
Figure A-5. Cost breakdown of optimal CSP/ TES (Scenario 2) SIPH subsystems required for industrial hot air supply case study	60
Figure A-6. Monthly thermal energy delivered by the energy sources in the optimal CSP/ TES (Scenario 2) SIPH system designed for industrial hot air supply case study	60
Figure A-7. Potential reduction in the LCOH of the optimal CSP/ TES (Scenario 2) SIPH system designed for industrial hot air supply case study	60
Figure A-8. Sensitivity of the LCOH of the optimal CSP/ TES (Scenario 2) SIPH system designed for industrial hot air supply case study to the variation in main economic parameters	61
Figure A-9. Cost breakdown of optimal CSP/ TES (Scenario 2) SIPH subsystems required for cogeneration case study	62
Figure A-10. Monthly thermal energy delivered by the energy sources in the optimal CSP/ TES (Scenario 2) SIPH system designed for cogeneration	62
Figure A-11. Potential reduction in the LCOH of the optimal CSP/ TES (Scenario 2) SIPH system designed for cogeneration case study.....	62
Figure A-12. Sensitivity of the LCOH of the optimal CSP/ TES (Scenario 2) SIPH system designed for cogeneration case study to the variation in main economic parameters	63
Figure A-13. Effect of oversizing the power cycle on the LCOH of the optimal configurations.....	64

List of Tables

Table 1. Receiver Design Parameters: Notations, Units, and Values	11
Table 2. Key Subset of SolarPILOT Parameters Set by Modelon Impact and Corresponding Default Values.....	14
Table 3. Annual Solar Field Efficiency Errors Using Modelon Impact’s Three Interpolation Methods....	15
Table 4. Annual Energy per Solar Field Area Calculated Using SolarPILOT and Modelon Impact Using Linear and Akima Spline Interpolation.....	16
Table 5. Scenarios Using Steam, Hot Air, and Hot Particles for Industrial Processes	29
Table 6. PV/CSP/TES Scenarios Evaluated in this Project	34
Table 7. Descriptions of Terms Used in the LCOH Calculation	35
Table 8. Empirical Formulas and Base Case Cost Inputs Used to Estimate the Capital Cost of SIPH Components.....	36
Table 9. Operation and Maintenance Costs of SIPH Components	37
Table 10. Base Case Performance Parameters.....	39
Table 11. Overview of Optimization Problem Adopted in this Study.....	40
Table 12. Value Ranges Used to Assess Sensitivity of the SIPH Systems.....	40
Table 13. Optimal Configurations of SIPH for Industrial Steam Supply Case Study	42
Table A-1. Optimal Configurations of SIPH for Bauxite Calcination Case Study.....	54
Table A-2. Overview of the Optimal CSP/TES (Scenario 2) SIPH Subsystems Sizing and Capital Costs	55
Table A-3. Optimal Configurations of SIPH for Bauxite Calcination Case Study with the Grid Dependency Constraint (<5%).....	57
Table A-4. Optimal Configurations of SIPH for Industrial Hot Air Supply Case Study.....	58
Table A-5. Overview of Optimal CSP/TES (Scenario 2) SIPH Subsystems Sizing and Capital Costs	59
Table A-6. Optimal Configurations of SIPH for Industrial Hot Air Supply Case Study With the Grid Dependency Constraint (<5%).....	59
Table A-7. Optimal Configurations of SIPH for Cogeneration Case Study	61
Table A-8. Optimal CSP/TES (Scenario 2) SIPH Subsystems Sizing and Capital Costs	63

1 Introduction

Industrial sectors of the United States produced 23% of the country’s greenhouse gas emissions in 2021 [1]. Industrial emissions often come primarily from on-site combustion to generate high-temperature heat to drive various processes (e.g., thermal treatment, chemical reactions, and melting) and on-site power production, and heavy uses of cheap easily accessible fossil fuels make decarbonization difficult. Pathways considered to achieve carbon neutrality include electrification by renewable power coupled with batteries or carbon-free heat sources (e.g., hydrogen and thermal energy storage). One potential carbon-free heat source is using solar resources plus thermal energy storage (TES) [2,3].

Figure 1(a) shows industrial process heat ranges and potential renewable energy supply with three storage methods. This project was based on a particle TES platform to develop a system code named Heat Exchanger and Thermal Energy Reservoir (HEATER) for assessing solar industrial process heat (SIPH). Figure 1(b) shows a comparison among batteries, hydrogen, and TES. TES is one step to industrial process heat and shows significant advantages for SIPH over batteries and hydrogen from both cost and simplicity. One barrier is the competition by fossil fuels that are traditionally used in industrial process heat with infrastructures already being developed. Thus, deployment of a HEATER system likely starts from niche applications that directly bring economic and environmental benefits to a user.

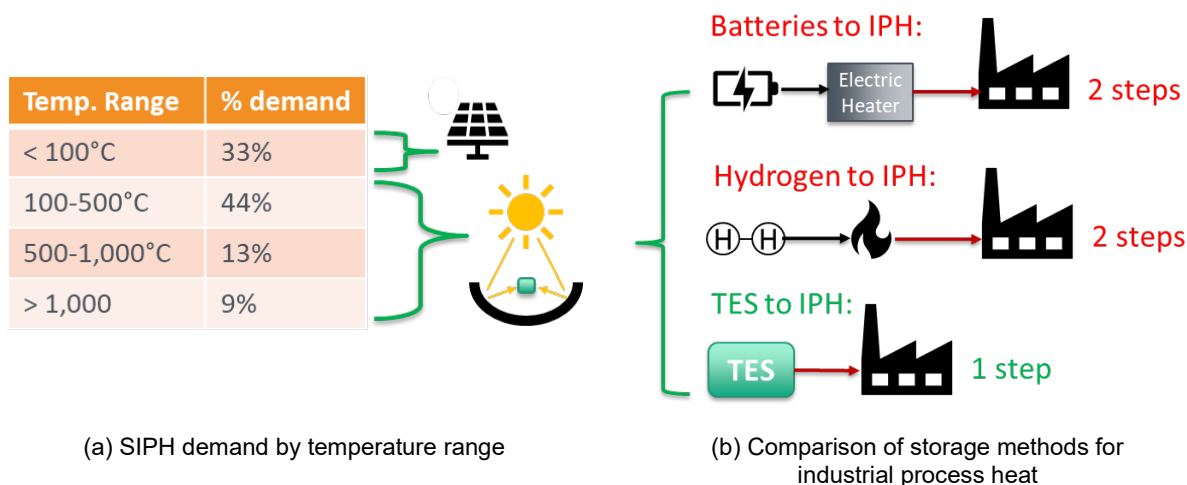


Figure 1. Comparison of industrial process heat where TES eliminates thermal energy conversion: Less complexity, equipment cost, efficiency losses

To enable wider commercial deployment, SIPH must achieve optimal cost decreases, performance improvements, and technical maturity. The energy cost model can be the first effective proxy to evaluate the cost competitiveness of zero-carbon solutions at different capacity factors in order to demonstrate a cost goal that can displace fossil fuels. This analysis is critical because the capital and levelized energy costs for zero-carbon process heat systems change significantly with configuration (power to heat or power to heat and power) duration (8–24 hours or 24+ hours), and the industrial process is sensitive to capital investment.

As with any emerging energy technologies, SIPH may not be immediately cost-effective in all industry sectors. However, certain applications can be promising with both economic and environmental appeals. One such application is bauxite mining to produce alumina for aluminum production. Hot air is used in alumina refining to clean raw bauxite particles for primary metal smelting. Alumina refining is a core step to producing virgin aluminum. It is a complex process that can be facilitated by concentrating solar power (CSP) and solar photovoltaics (PV). The HEATER system for SIPH can provide particle heating, hot air, steam, and power.

1.1 Project Goals

In this project, an SIPH tool was developed that integrates concentrating solar thermal (CST), photovoltaic (PV), particle TES for industrial process heat (industrial process heat) applications. We also studied performance, configurations, and potential economic opportunity in specific industrial cases of the solar plus particle-based TES to help facilitate adoption.

NREL and its partners aimed to develop a uniform particle TES platform to provide reliable industrial process heat supply over a wide range of temperatures for different industry applications. NREL worked with industry partners to commercialize the TES system, including discharging heat exchangers that can integrate with a CST system for heat supply. The heat-carrying medium can be hot water, air, or steam to serve typical industrial processes ranging from mining, material, and food processing to plant operations, and other applications. The proposed flow diagram for a system to supply industrial process heat shown in Figure 2(a) is the basis of software development to support the particle TES applications.

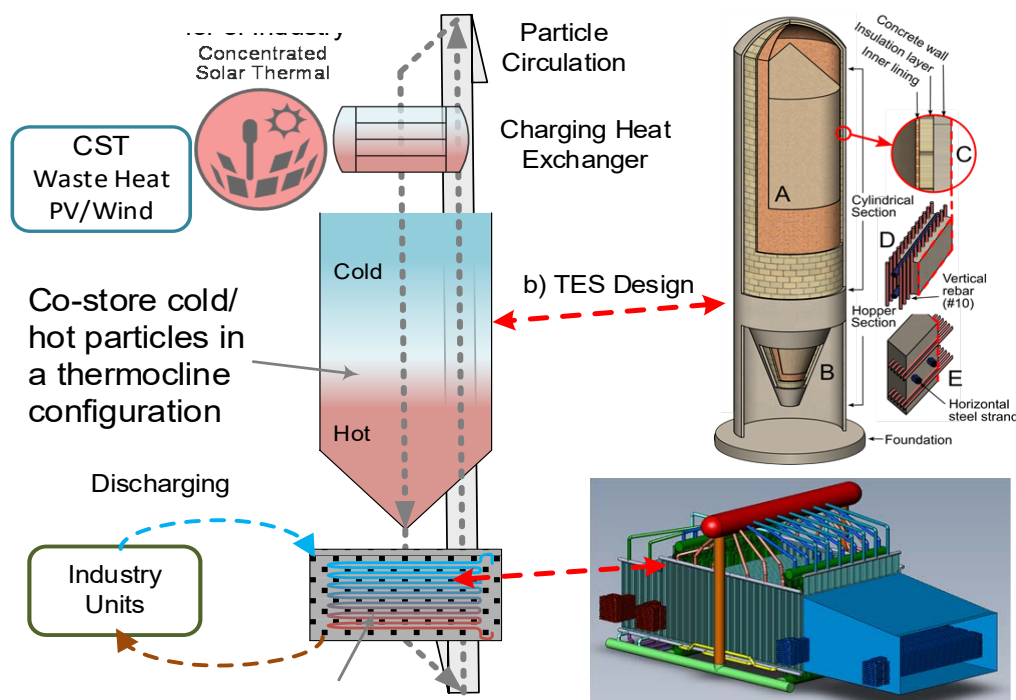


Figure 2. Diagram of supplying industrial process heat with solar energy sources with particle TES

The particle TES (b) silo and (c) steam boiler, two major components, are shown on the right. Graphic by NREL.

A key objective of the industrial process heat development is energy system and component designs and modeling tools that are capable of evaluating particle TES commercialization and deployment potentials. The HEATER system modeling tool based on Modelon Impact software can help industry adopt renewable energy sources with energy storage for industrial process heat to reduce the carbon footprint. Meanwhile a techno-economic analysis tool has been developed to assess the economic opportunities for certain industrial applications.

We performed a broad survey of literature and industry uses of SIPH to prioritize the software capabilities. Process heating is diversified in temperature ranges, capacities, and directly linking to manufacturing settings [3]. The thermal energy for these processes is most-often derived from fossil fuels (coal or natural gas) or electricity with significant process end-use losses and upstream carbon emissions. Despite the significant emission reductions possible, replacing fossil fuels with renewable energy and TES, certain technical, economic, and reliability challenges must be overcome. Thus, a software tool must be able to simulate industry loads, operation processes, economic returns, and it must be easy to use and adaptable to specific applications (e.g., location, end-use, scale, and temperatures).

Also, the modeling tool development reflects the need to handle the complexity of industrial process and applications and needs of end users. In addition, we developed a techno-economic analysis methodology and conducted such an analysis to inform and facilitate pathways for SIPH applications. The techno-economic analysis investigates application potentials and broad impacts of SIPH systems to supply reliable, carbon-free industry heat.

1.2 Modeling Tool Architecture and Solver Introduction

Figure 3 shows the software architecture integrating component mass and energy balances, component sizing tools, system configurations with CST and/or electric heat from PV. Some components will interface with existing NREL tools such as SolarPILOT for CST performance and design and NREL's System Advisor Model (SAM).

The SIPH system modeling tool was built on the Modelica-based modeling software Modelon Impact [4]. Modelica is a system modeling language that is object-oriented, transient, acausal, and hierarchical [5]. The language has been used to examine a range of different systems across fields [6–9]. The language functions through the development of libraries of component models that can be interchanged and connected as modular units to create fully integrated system models. These libraries can be shared across platforms.

A primary technical goal of the project was to develop—and validate against high-fidelity models—a library of individual component models in Modelon Impact that can be configured into various SIPH models. The library is comprised of a suite of components that could be useful in modeling SIPH systems that use solid particles as the storage medium (i.e., solar particle receiver, electric particle heater, particle storage silo, particle-air and particle steam heat exchangers, and particle skip hoists). Additional components for modeling SIPH systems (e.g., steam turbines and pumps) can be imported from existing libraries inside Modelon Impact, the open-source Modelica base library, or other open-source libraries found in the literature (e.g., SolarTherm [8]).

The Modelon Impact user interface contains a user-specific workspace (upper left in Figure 4). It can be comprised of entirely custom component models, new controllers, models that were modified from the existing Modelon Impact library, and fully integrated system models. The existing Modelon Impact library (lower left in the figure) contains both the open-source Modelica Standard Library and proprietary Modelon Impact libraries of component and system models. These libraries also contain useful functions.

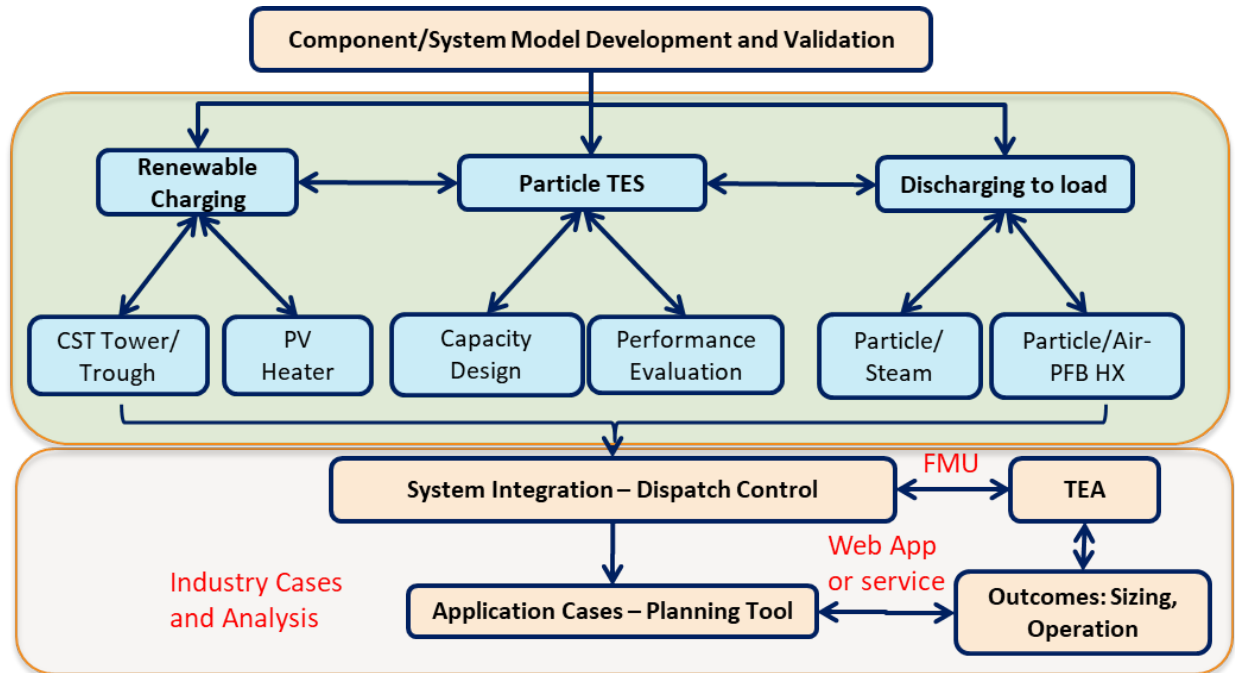


Figure 3. Software architecture for component modules and HEATER system models

Graphic by NREL

FMU: functional mock-up unit
 PFB HX: particle-air, pressurized, fluidized bed heat exchanger
 TEA: techno-economic analysis.

The user interacts with the system model in the center of the interface either through a graphical or code view. The graphical layer shown in Figure 4 is useful for building connections between components, establishing configurations, and defining parameter values (right side of the figure). The code layer is useful for constructing new components, defining the appropriate physics (e.g., variables, parameters, and equations), and performing basic functions. The full suite of development pathways was leveraged in this project to develop a unique library of component and system models for SIPH with particle TES systems.

In the Modelica language’s architecture, the system of equations and variables are packaged within each module. Each module is then (most-often) internally balanced (i.e., equal number of knowns and unknowns) once given boundary conditions for “ports.” Ports are how modules interact with modules and can be flow, electrical, thermal, real and Boolean signals, among others. If two ports are connected, their state variables are defined to be equivalent. For example, in a thermal connection, the state variables are temperature and heat flow rate.

Models are solved through compilation of the Modelica code. An example of the generation of the system of equations and variables for a simple tank model is shown in Figure 5. The compiler and solver are Modelon Impact-specific software. Several open-source and proprietary compilers and solvers for Modelica code exist. The automated equation generation is a unique feature of the software that enables solving a connected system without going through line-by-line source code writing and discretizing conservation equations manually, which can be prohibitively complicated and error prone, especially as system size and configuration options grow.

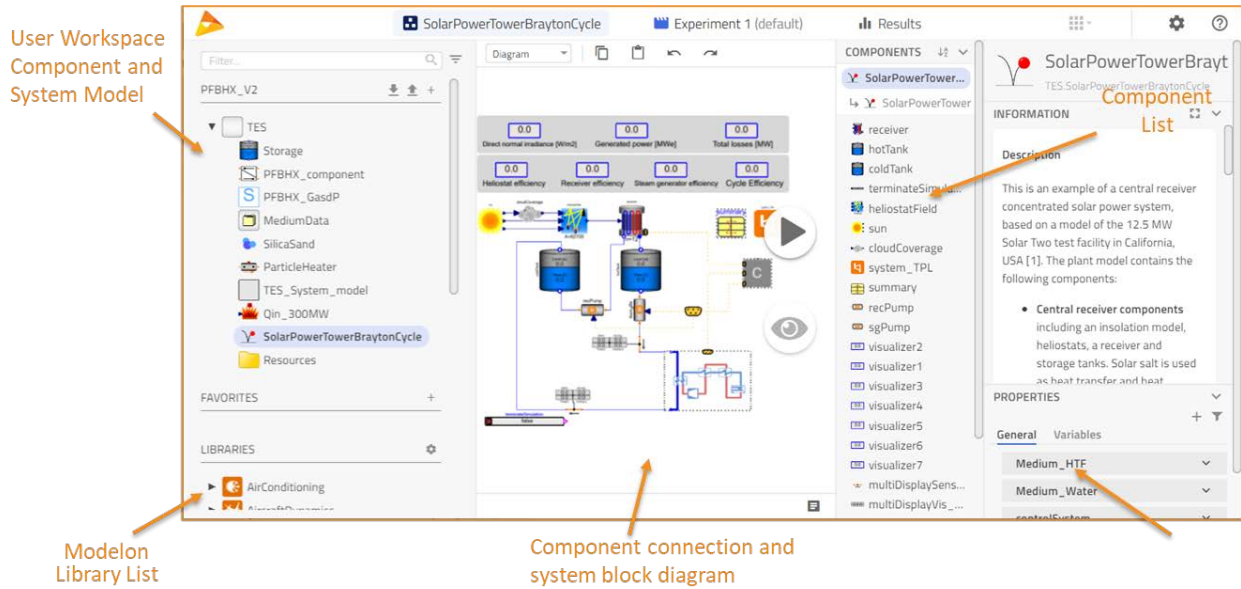


Figure 4. Modelon Impact interface and major functional menus

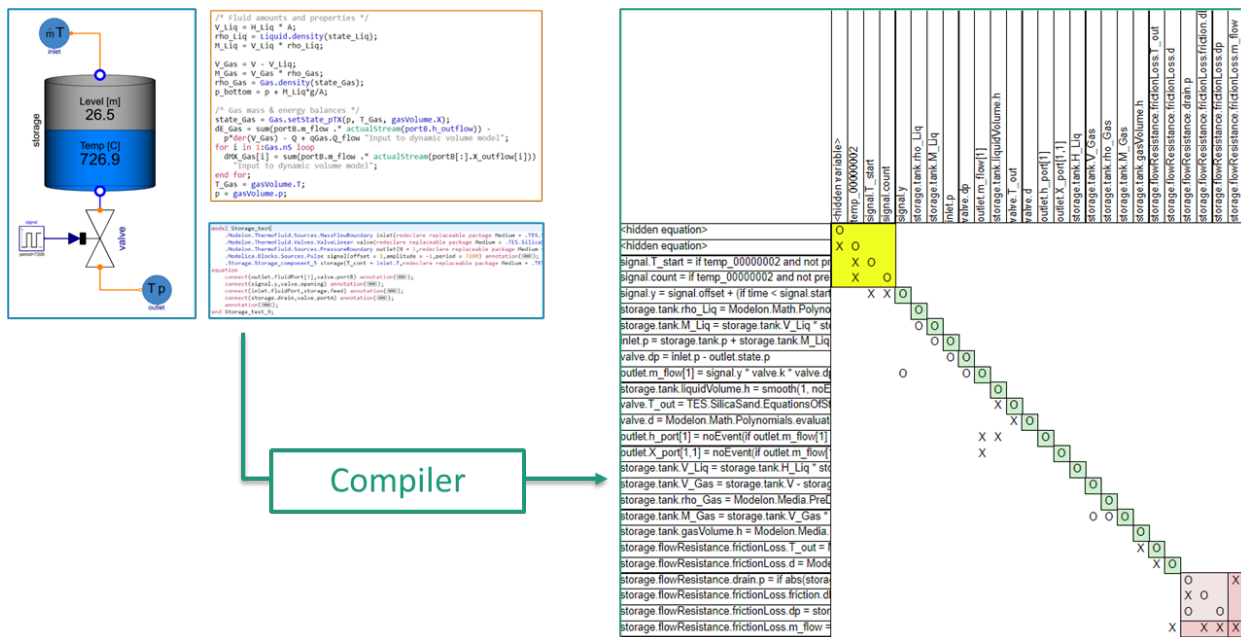


Figure 5. Modelon Impact's compiler generates system of equations automatically for solver

1.3 Report Organization

The rest of this report is organized as follows: Section 2 focuses on the development and validation of the individual component models that are required for the Modelon Impact-based industrial process heat design tool. Section 3 demonstrates the integration of the individual component models to create an integrated system modeling tool using an industrial heated steam supply application. Section 4 presents the development of the techno-economic analysis methodology and the evaluation of the economic cost of using SIPH systems to provide carbon-free heat for four different common use cases.

2 Component Model Development and Validation

The project began with the development and validation of component models in Modelon Impact that are needed to create SIPH integrated system models. Figure 6 shows an overview of the new component library and validation procedure. Individual component models in Modelon Impact are reduced-order model (ROM) versions of existing, benchmarked, higher-fidelity models. It is too computationally expensive to run high-fidelity models (e.g., a computational fluid dynamic simulation) when trying to run system-level models, which focus on system design, configuration, and performance evaluation. Therefore, the project ensured the ROM can accurately predict the most important performance metrics of each component while greatly reducing computational cost.

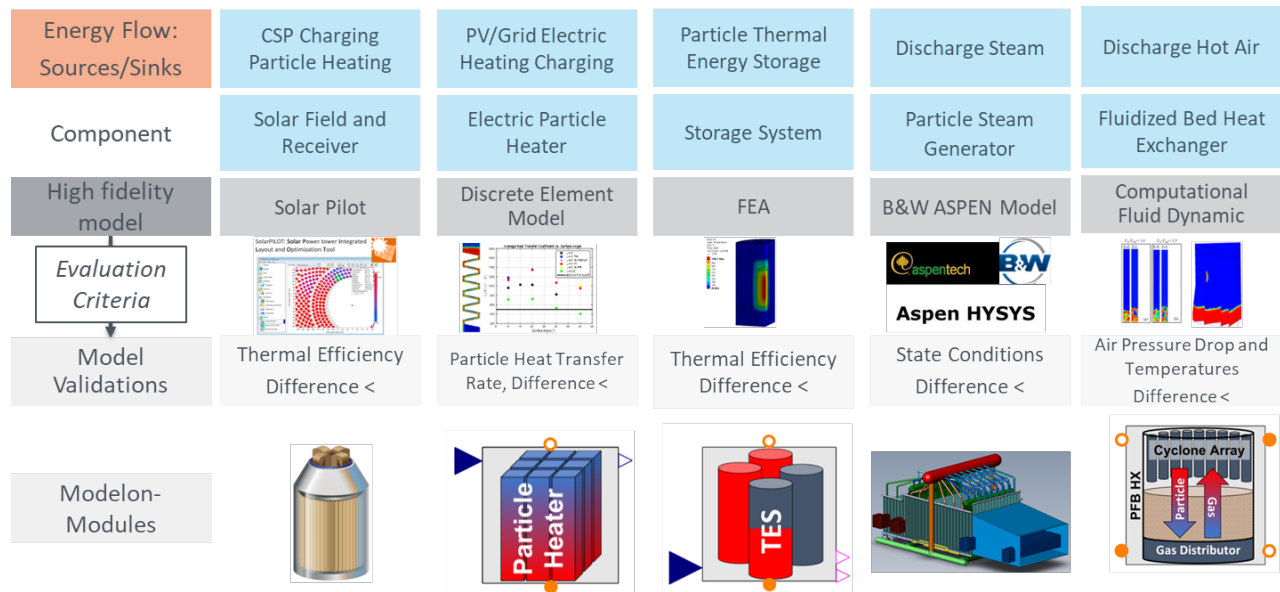


Figure 6. Summary of component model library developed and validation procedure in this project

2.1 Electric Particle Heater

An electric particle heater model was developed to enable interfacing with solar PV, wind, other electric generation technologies, and the grid for charging the particle TES system. The electric particle heater was based on an open-flow, electric resistive heating component.

2.1.1 Modeling Approach

In the SIPH system, particles are driven by gravity in a non-plug flow regime; therefore, the momentum balance is not of focus in the component model. The heater is modeled as a square discretized pipe with heat transferred based on wall temperature T_w , heat transfer coefficient α_i , and heat transfer area terms A_i ; see Figure 7(c).

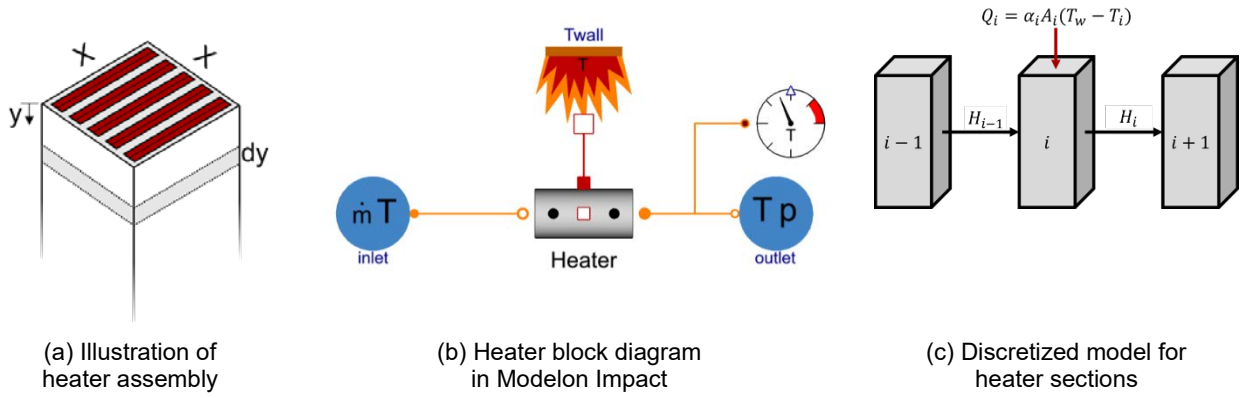


Figure 7. Geometry representation (a), simple test model (b), and mathematical energy balance on a discretized volume for particle heater (c)

The governing mass and energy balance equations for a single heater are described here. The pipe has dimensions of $X \times X \times L$ (e.g., 1 m x 1 m x 2 m); see Figure 7(a). The 1D pipe is divided into N volumes of equal volume; N is an input parameter of the component model with a default value of 10. The particle medium “flowing” through the pipe is of constant density and therefore the mass and mass flow rate of each volume is constant:

$$m = m_i, \dot{m} = \dot{m}_i, \forall i. \quad (1)$$

The energy balance for the i^{th} volume is as follows:

$$\frac{dU_i}{dt} = H_{i-1} - H_i + \alpha_i A_i (T_w - T_i), \forall i \quad (2)$$

where, assuming constant mass m_i , incompressible fluid $v_i = C$, and no pressure change $P_i = C$, the internal energy of the i^{th} volume U_i is defined as:

$$\frac{dU_i}{dt} = m_i \frac{dh_i}{dt}, \forall i \quad (3)$$

The rate of energy flows in and out of the i^{th} volume are defined as:

$$H_i = \dot{m} h_i \quad (4)$$

The enthalpy of the i^{th} volume is solely a function of temperature for an incompressible fluid (e.g., particle medium):

$$h_i(T_i) = \int_{T_{ref}}^{T_i} c_p(T) dT, \forall i \quad (5)$$

The heat transfer coefficient α_i [W/m²-K] is an input parameter that is defined based on results of a high-fidelity, discrete element method model built in the MFiX (Multiphase Flow with Interphase eXchanges) software [10]. Schirck et al. [10] found the heat transfer coefficient to vary with assumed friction coefficient and heating element surface angle. Therefore, the ROM employs a look-up table for the appropriate heat transfer coefficient based on the user-specified

values of the friction coefficient and heat element surface angle parameters. The heat transfer area term A_i [m²] is the same in all volumes and defined based on the input parameter \bar{A} [m²/m³]. \bar{A} is defined as the heat transfer area per unit volume and is calibrated based on the high-fidelity model. The relationship between \bar{A} and A_i is as follows:

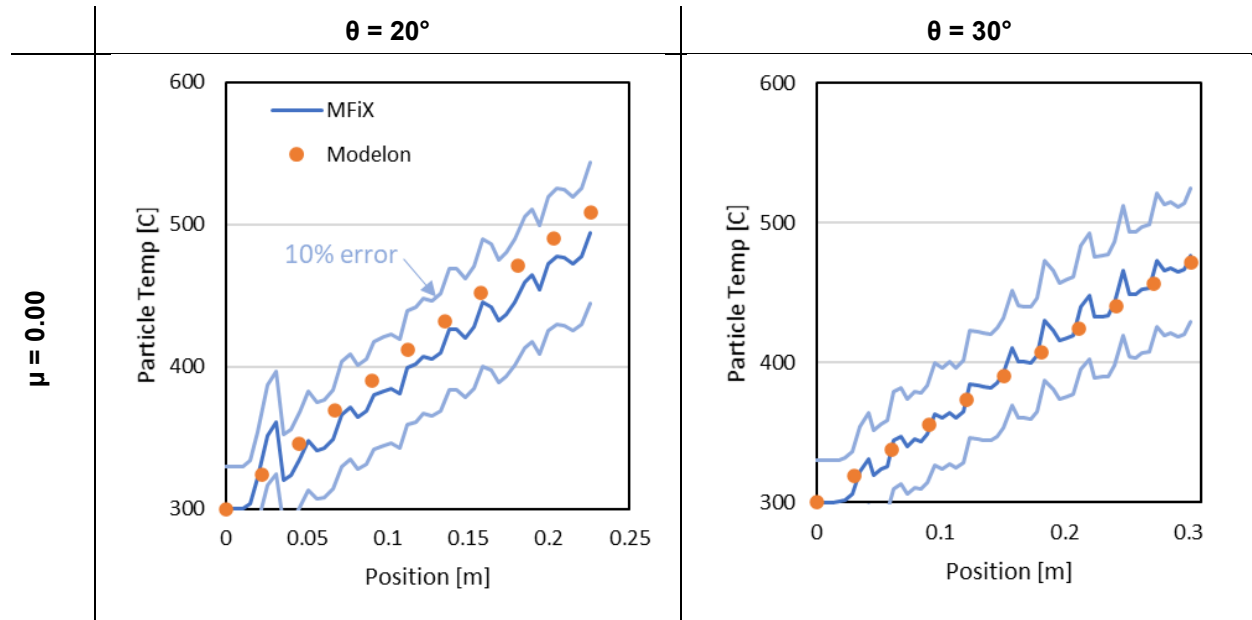
$$A_i = \bar{A} \left(\frac{X^2 L}{N} \right) \quad (6)$$

Therefore, the total heat transfer area in the heater scales with interior volume of heater and the i^{th} volume has $(1/N)^{\text{th}}$ of the total heat transfer area. The wall temperature T_w is controlled by a proportional–integral–derivative controller to meet a target outlet temperature with maximum wall temperature limitations defined by the heating element material.

2.1.2 Validation

A high-fidelity, discrete element method model of the particle heater served as a basis for the Modelon Impact-based particle heater model. The discrete element method model, which was built in MFiX, simulated the actual electric particle heater flow geometry and was able to measure the average heat transfer coefficient. The predicted temperature profiles through the particle heater output by the two models were compared to validate the Modelon Impact-based ROM.

The temperature profiles were compared for two surface angles and two friction coefficients of the hexagonal heating elements (total of four cases). The results can be found in Figure 8. For all four cases examined, the Modelon Impact-based ROM was within 10% of the MFiX results; doing so validated the ROM prediction of the performance of the electric particle heater.



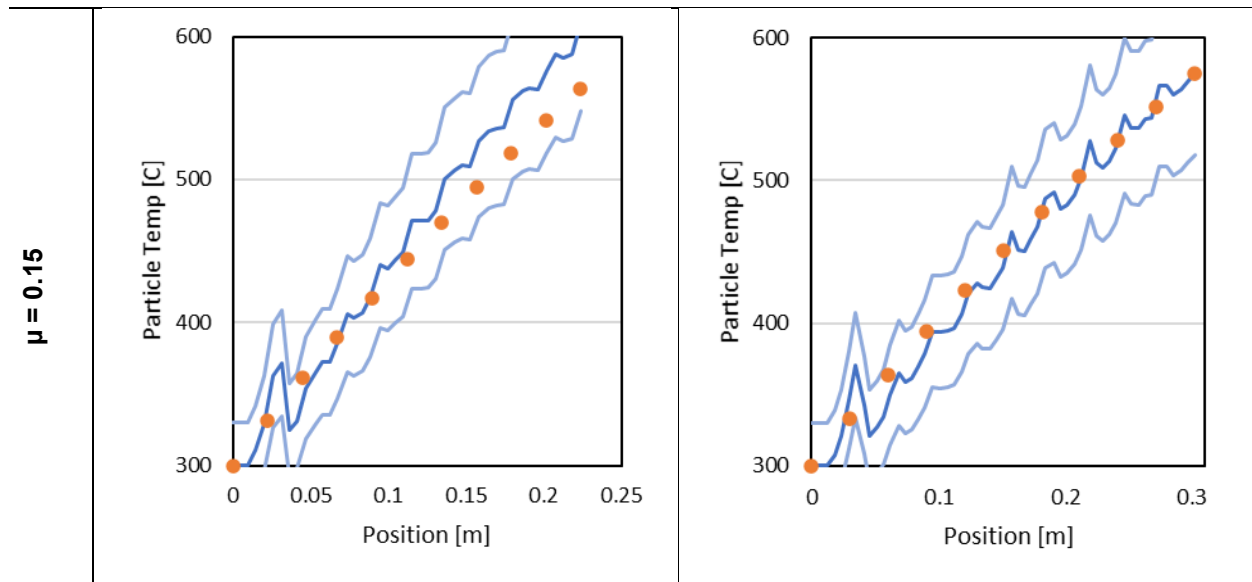


Figure 8. Comparison of 1D temperature profiles predicted by the high-fidelity MFiX and Modelon Impact-based ROM of the electric particle heater at two different surface angles (θ) and friction coefficients (μ)

2.2 Solar Particle Receiver and SolarPILOT Integration

2.2.1 Modeling Approach

The receiver was modeled as a zero-dimensional (0D), steady-state design. The receiver model consisted of two major parts: the receiver wall and the particle fluid as shown in Figure 9(a). The solar incidence on the receiver wall, the radiative and convective heat loss from the wall to the ambient, the heat transfer between the wall and the particles, as well as the temperature variance from particle inlet to outlet were simulated within this receiver model. The geometry of this receiver was modeled as a cylinder, which can be seen from Figure 9(b). The icon figure of the receiver was adopted from the references [11,12].

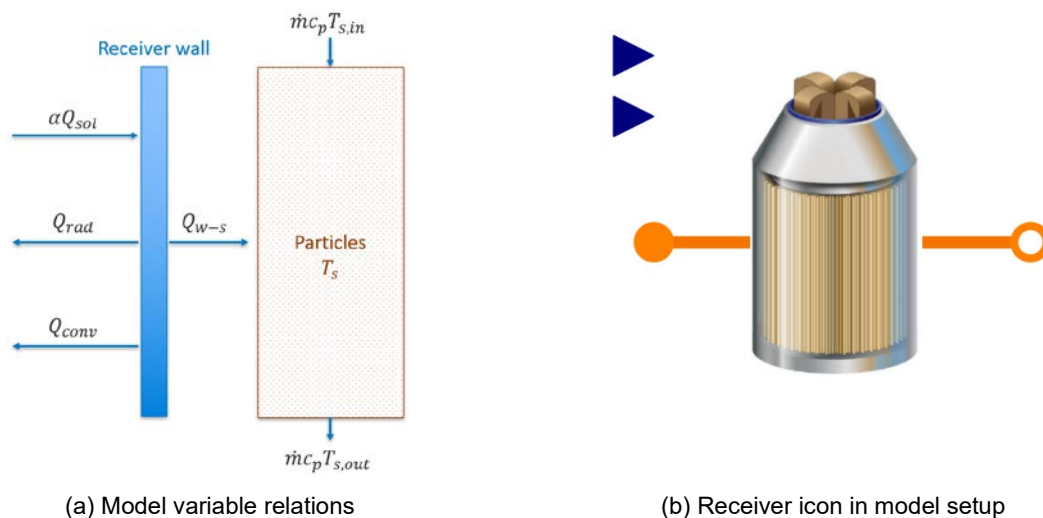


Figure 9. Receiver model composition (a) and its icon representation in Modelon Impact (b)

The design parameters of the receiver include the receiver height and diameter, receiver wall absorptance and emissivity, the view factor between the receiver and the ambient, natural convection heat transfer coefficient, and the heat transfer coefficient between the wall and the particles. The values of these parameters are listed in Table 1. Some of the parameters were adopted from the references [12].

Table 1. Receiver Design Parameters: Notations, Units, and Values

Design Parameter	Notation	Unit	Value
Receiver height	H	m	16
Receiver diameter	D	m	15
Wall absorptance	α	—	0.9
Wall emissivity	ε	—	0.9
View factor	F	—	1
Natural convection heat transfer coefficient	hconv	W/m ² -K	500
Solids-wall heat transfer coefficient	hw-s	W/m ² -K	400

The following equations establish the energy balance of the receiver wall and the particles. The energy balance of the receiver wall is given by:

$$\alpha \dot{Q}_{sol} - \dot{Q}_{rad} - \dot{Q}_{conv} - \dot{Q}_{w-s} = 0, \quad (7)$$

where the \dot{Q}_{sol} is the insolation power from the heliostat field to the receiver and α is the absorptance of the receiver wall; \dot{Q}_{rad} , \dot{Q}_{conv} , and \dot{Q}_{w-s} are the radiative heat loss, convective heat loss, and heat transfer between wall and particles respectively. \dot{Q}_{rad} can be calculated by:

$$\dot{Q}_{rad} = F\varepsilon\sigma A(T_w^4 - T_{amb}^4), \quad (8)$$

where T_w and T_{amb} are the wall temperature and ambient temperature respectively; F is the view factor; ε is the wall emissivity; σ is the Stefan–Boltzmann constant; A is the surface area of the receiver. \dot{Q}_{conv} is obtained by:

$$\dot{Q}_{conv} = h_{conv}A(T_w - T_{amb}), \quad (9)$$

where h_{conv} is the natural convection heat transfer coefficient. The heat transfer between the wall and particles is calculated by:

$$\dot{Q}_{w-s} = h_{w-s}A(T_w - T_s), \quad (10)$$

where h_{w-s} is the wall-solids heat transfer coefficient; T_s is the bulk solid temperature. The energy balance of the particles is ensured by the following equation:

$$\dot{Q}_{w-s} = \dot{m}c_p(T_{s,out} - T_{s,in}), \quad (11)$$

where \dot{m} represents the solid mass flow rate; c_p is the specific heat capacity of the particles; $T_{s,in}$ and $T_{s,out}$ are the inlet and outlet temperatures of the particles. To close the relationship between the unknowns, we assumed the bulk solid (particles) temperature T_s can be approximated by the average value of the inlet and outlet temperatures; the following equation reflects this assumption:

$$T_s = \frac{T_{s,out} + T_{s,in}}{2}. \quad (12)$$

In a 1D or 2D receiver model, this assumption can be replaced by discretized temperatures of each particle solid element and the heat transfer between the adjacent elements.

The above receiver model was implemented in Modelon Impact. Figure 10 shows the Modelon Impact of the implemented receiver model connected to a heliostat field model and models representing boundary conditions. In the figure, a simple sun model determines the sun position (elevation and azimuth) and the intensity of the direct normal insolation, which then serve as heliostat field model inputs. The cloud coverage model emulates the passing of the clouds blocking the sun. The weather model simulates the ambient temperature. The heliostat field module calculates the incident concentrated thermal power based on DNI, heliostat field area, and field efficiency, a function of solar position, calculated using SolarPILOT (the details of integrating software framework are presented in Figure 12 and described below) or defined directly by the user.

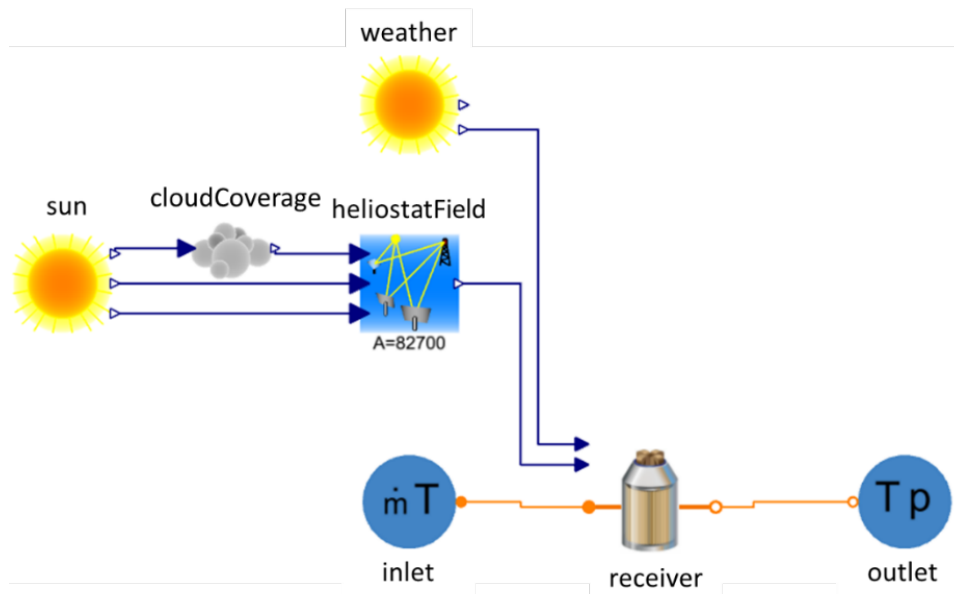


Figure 10. Diagram of the receiver model connected with a heliostat field model in Modelon Impact

For this test simulation, the heliostat field area and particle flow rate through the receiver were assumed to be 82,700 m² and 100 kg/s respectively. The test simulation results for a summer day test run are shown in Figure 11. The inlet temperature of the receiver is kept at 273 K, the outlet temperature changes with the receiver wall temperature throughout the day when the solar insolation first increases then decreases. It is noteworthy that the simulation results are based on hypothetical inputs and parameters.

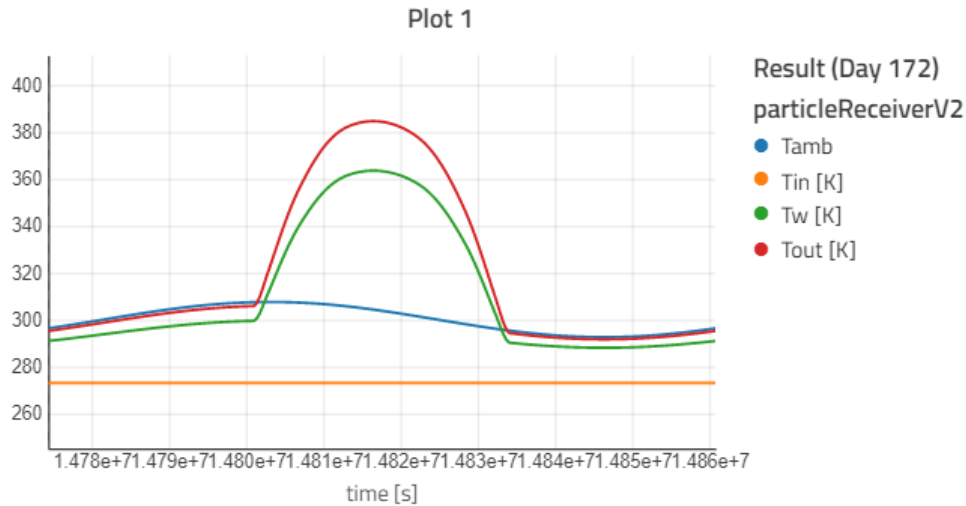


Figure 11. An initial result of the receiver model for a summer day test run

After the system model (Figure 10) compiles in Modelon Impact, the model initializes, during which the external SolarPILOT C functions are called. These C functions, embedded in a SolarPILOT library file, set the parameters required by SolarPILOT for running the simulations to generate a heliostat solar field efficiency matrix as a function of azimuth and elevation angles. Once Modelon Impact-specific parameters are set within SolarPILOT, SolarPILOT runs heliostat field performance simulations using a uniform sampling grid of azimuth and elevation angles.

Once simulations are complete, SolarPILOT writes the heliostat field efficiency matrix to a text file in a directory designated by Modelon Impact. It reads the heliostat field efficiency file into the system model where the efficiency matrix will be used as a look-up table during time-series system simulations. This process happens during the initialization stage (following the compiling step) in the Modelon Impact solution procedure.

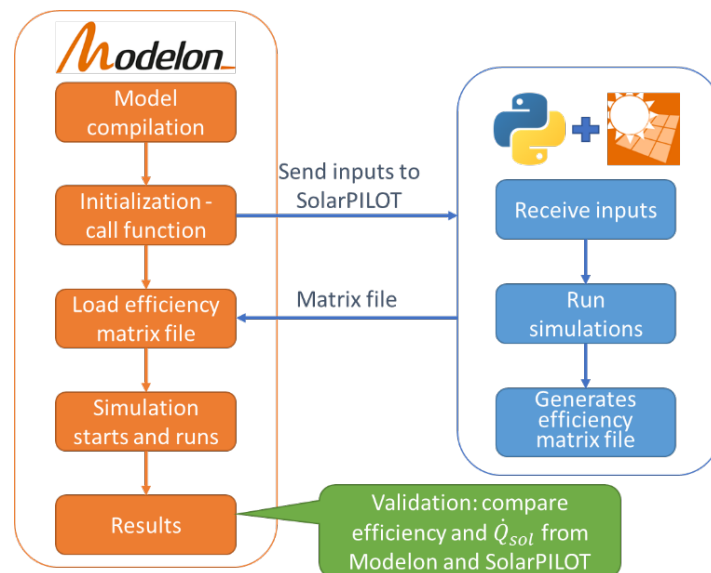


Figure 12. Software framework of the integration of Modelon Impact and SolarPILOT (Graphic by NREL)

The exchanged parameters between Modelon Impact and SolarPILOT and their default values are shown in Table 2. This table contains a minimum set of variables that Modelon Impact sets within SolarPILOT. SolarPILOT has numerous variables not presented in this table but are easily accessible to Modelon Impact users, thereby enabling customization. If certain values are not set from the Modelon Impact side, SolarPILOT default values are used.

Table 2. Key Subset of SolarPILOT Parameters Set by Modelon Impact and Corresponding Default Values

Description	Default value	Units
Weather file to use for analysis	USA CA Daggett (TMY2).csv	none
Sunshape model {0=point sun, 1=limb darkened sun, 2=square wave sun, 3=user sun}	1	none
Atmospheric attenuation model {0=25km Barstow, 1 = 5km Barstow, 2 = user defined}	0	none
Atmospheric attenuation coefficients for user-defined analysis	0.006789,0.1046,-0.0170,0.002845;0.01293,0.2748,-.03394,0;0.006789,0.1046,-0.0170,0.002845	none
Integer to specify the canting method {0=none, -1=Cant on-axis equal to slant range, 1=user-defined on-axis, 3=user-de	1	none
The focusing method {0=Flat, 1=Each at slant, 2=Average of group, 3=User defined}	1	none
Height of the heliostat structure	12.2	m
Width of the heliostat structure	12.2	m
Number of cant panels in the X direction	2	none
Number of cant panels in the Y direction	8	none
Ratio of mirror area to total area of the heliostat defined by wm x hm	0.97	none
Average reflectivity (clean) of the mirrored surface	0.95	none
Average soiling factor	0.95	none
Receiver diameter for cylindrical receivers	17.65	m
Height of the absorbing component	21.6	m
DNI value at which the design-point receiver thermal power is achieved	950	W/m ²
Design thermal power delivered from the solar field	670	MWt
Sun location when thermal power rating is achieved	0	none
Average height of the tower receiver centerline above the base heliostat pivot point elevation	195	m
Receiver absorptance	0.94	none
Full path name	N/A	N/A
Table name	N/A	N/A

Once the model initializes successfully, the Modelon Impact simulation runs and generates the time-series results. During the Modelon Impact simulation, the heliostat field model determines the field efficiency by interpolating the SolarPILOT generated efficiency matrix (based on the solar azimuth and elevation angles). The purpose of this interpolation is to reduce the computational expense of performing annual simulations compared to calling SolarPILOT for each time-step. SolarPILOT solar field configuration is a one-time heliostat layout that defines the CST system design.

2.2.2 Modelon Impact Model Validation

As mentioned, the Modelon Impact heliostat model uses an interpolation method of the SolarPILOT calculated efficiency matrix to determine the efficiency given a solar position (i.e., azimuth and elevation angles). To validate this approach, the solar field efficiency for an entire year using Modelon Impact's three interpolation methods was compared to SolarPILOT's calculated value. Modelon Impact's three interpolation methods include linear interpolation, constant segment method, and Akima spline method. Akima spline is a method for approximating the function between interpolation points using a piecewise cubic function. For the comparison, all time-steps where the solar elevation angle is less than 10 degrees (i.e., sunrise and sunset) were removed.

Table 3 presents annual solar field efficiency error metrics using Modelon Impact’s three interpolation methods compared to the SolarPILOT’s predicted values. The constant segment interpolation method resulted in the highest error values. Linear and Akima spline methods both performed very well with an average absolute error of less than 1%; however, Akima spline resulted in the lowest error values with an average absolute error of less than 0.1%.

Table 3. Annual Solar Field Efficiency Errors Using Modelon Impact’s Three Interpolation Methods

Error	Linear	Constant Segment	Akima Spline
Average Absolute Error [%]	-0.62	-3.33	-0.06
Absolute Error Standard Deviation [%]	0.61	8.15	0.18
Root Mean Squared Error [%]	0.87	8.80	0.19

Figure 13 presents the solar field efficiency determined by SolarPILOT as a function of solar azimuth and elevation angles for a 100 MW_t field located in Denver, Colorado. As expected, peak efficiencies occur near solar noon (i.e., azimuth equal to 0 degrees) and near the solar equinox because field cosine losses are minimum then. Conversely, the lowest efficiencies occur during early morning and late evening periods when the sun is low on horizon (i.e., elevation angles approaching 10 degrees). Typical concentrating heliostat fields cannot operate at elevations angles below this 10-degree threshold.

Figure 14 presents a comparison of absolute field efficiency error as a function of elevation angle using the linear and Akima spline interpolation methods. The Akima spline method results in a reduction of field efficiency absolute error compared to the linear interpolation method. Both methods result in the greatest error at low elevation angles. Additionally, this error decreases as elevation angle increases (Akima spline method error converges to near zero).

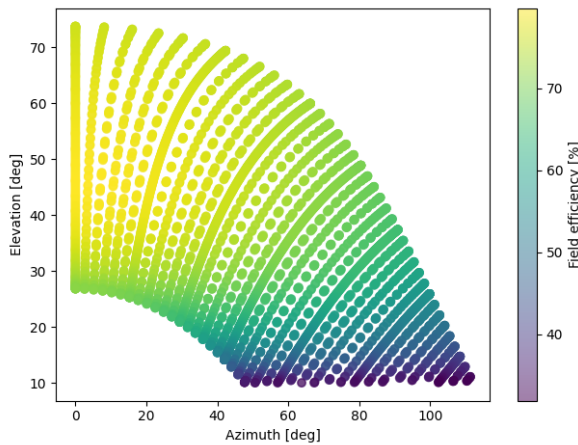


Figure 13. Solar field efficiency determined by SolarPILOT as a function of solar azimuth and elevation angles for a 100-MW_t field in Denver, Colorado

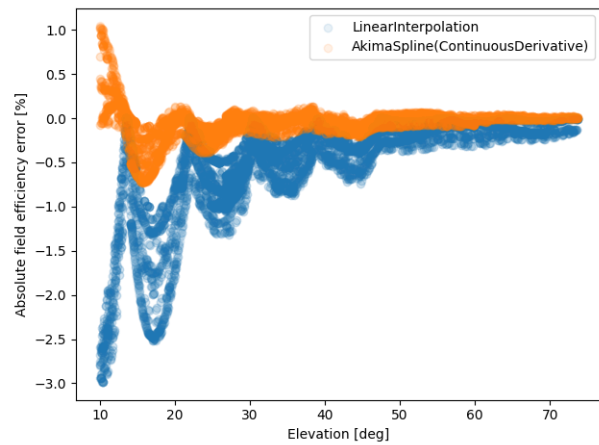


Figure 14. Comparison of absolute field efficiency error as a function of elevation angle using the linear and Akima spline interpolation methods

To evaluate how this impacts overall performance, the annual collected energy per unit area of solar field was calculated using Eq. (13).

$$E = \sum_t \eta_t^{sf} * DNI_t * \Delta_t \quad (13)$$

where E is the annual collected energy per unit area of solar field [kWh/m²], η_t^{sf} is the solar field efficiency predicted by either Modelon Impact interpolation or SolarPILOT directly [-], DNI_t is the direct normal irradiation (DNI) value given by a TMY (typical meteorological year) file of Denver, Colorado, (the location used for this analysis) (kW/m²), and Δ_t is the time-step (hr).

Table 4 presents the resulting calculations and relative error of the interpolation methods compared to SolarPILOT. The Akima spline interpolation method sufficiently predicts solar field efficiency and thereby energy to the receiver. Using the Akima spline method, the annual energy per solar field area with an error of -0.06% compared to calling SolarPILOT directly. Due to the lower errors, the Akima spline interpolation method was chosen for determining solar field efficiency from the SolarPILOT generated efficiency matrix during Modelon Impact time-series simulations.

Table 4. Annual Energy per Solar Field Area Calculated Using SolarPILOT and Modelon Impact Using Linear and Akima Spline Interpolation

Interpolation Method	Annual Energy per Solar Field Area (kWh/m ²)	Relative Error to SolarPILOT (%)
SolarPILOT	1,433.49	N/A
Linear	1,422.10	-0.795
Akima Spline	1,433.26	-0.060

2.3 Particle Storage Silo

The particle storage silo decouples the charging and discharging systems so that the output of the SIPH system does not need to directly match the solar resource profile. The SIPH tool models systems where the particles are stored in separate hot and cold silos (i.e., not a thermocline configuration). If single-silo, thermocline storage method is preferred, the particle storage silo model will require additional development.

2.3.1 Storage Modeling Approach

The particle storage silo model can be broken into two submodels: (1) the bulk particle volume model and (2) the storage containment model including thermal insulation and silo walls (see Figure 15). The bulk particle volume model comprises two dynamic volumes (particle and interstices gas volumes). These volumes are assumed to have unique homogeneous states (i.e., no thermal distribution). Energy, mass, and momentum balance equations are all needed in this model to resolve the particle storage temperature, state of charge, and pressure exerted at the outlet of particle storage silo.

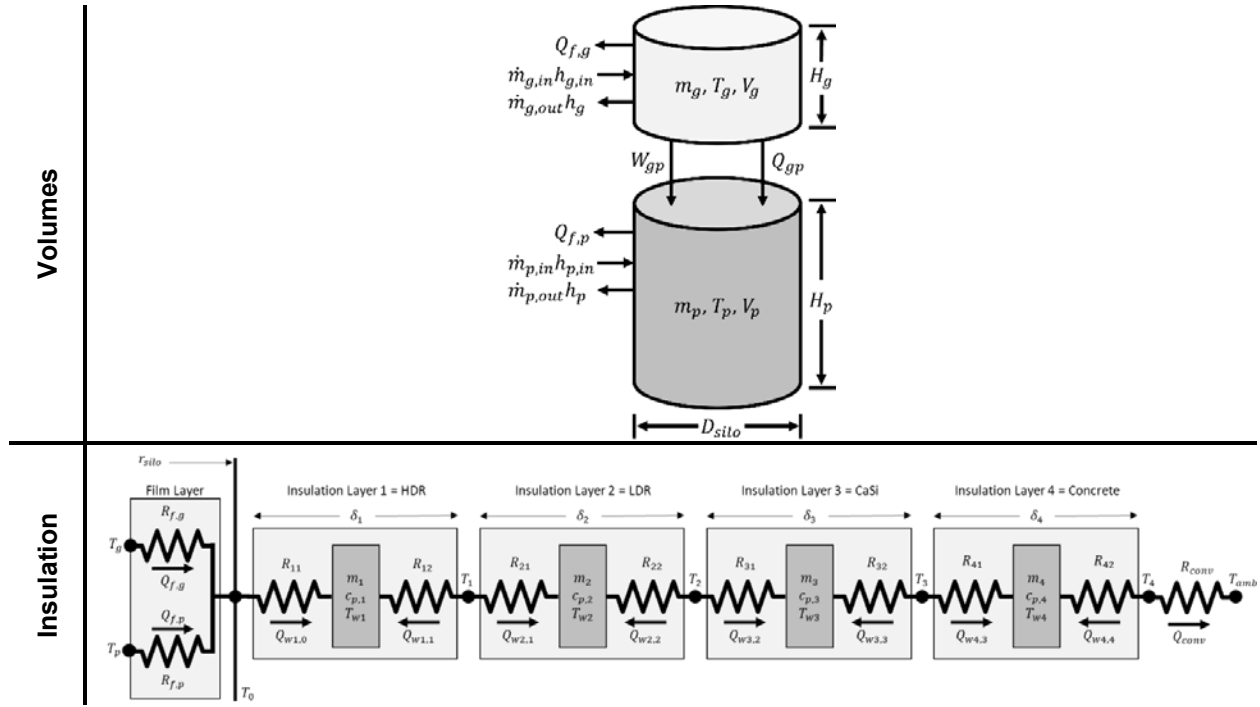


Figure 15. Graphical representation of the mathematical description of both the volume and insulation model that comprise a single containment model

The governing energy balance equations for the two volumes are as follows:

$$\frac{dE_g}{dt} = \dot{E}_g = \dot{m}_{g,in} h_{g,in} - \dot{m}_{g,out} h_g - W_{gp} - Q_{gp} - Q_{f,g} \quad (14)$$

$$\frac{dE_p}{dt} = \dot{E}_p = \dot{m}_{p,in} h_{p,in} - \dot{m}_{p,out} h_p + W_{gp} + Q_{gp} - Q_{f,p} \quad (15)$$

where:

$$W_{gp} = P \frac{dV_g}{dt} = P \left(-\frac{dV_p}{dt} \right) \quad (16)$$

$$Q_{gp} = h_{gp} A_c (T_g - T_p) \quad (17)$$

$$A_c = \frac{\pi}{4} (D_{silo})^2 \quad (18)$$

These equations are integrated over time from initial conditions (e.g., initial height of the particle medium, temperature of the two mediums) to solve for the current internal energy of each volume.

The particle inflow and outlet mass flow rates determine the current mass of particles (and therefore volume) in the silo. The combined volume of the gas and particle volumes is constant with the gas volume adjusting to fill the remaining space at constant pressure.

$$V_{silo} = A_c H_{silo} = A_c (H_p + H_g) = V_p + V_g = \text{constant} \quad (19)$$

The pressure at the particle outlet of the silo is computed by the gravitational weight of the particles stored in the silo:

$$P_{p,out} = P + \frac{m_p g}{A_c} \quad (20)$$

where P is the operating pressure of the tank (1 atm in this case) which is kept constant by the gas volume adjusting its mass by venting to or from an atmospheric reservoir (in proportion to its changing volume) as the volume occupied by the particles increases or decreases.

The dynamic volume models connect to the insulation thermal model through the film conduction heat flow terms in the energy balance equations for both volumes. The insulation thermal model is transient because of the thermal mass accounted for in the four insulation layer models.

There are three mechanisms of insulation between the bulk contents of the storage silo and ambient conditions (see Figure 15). First, there is a film layer comprised of two parallel resistances representing the film conduction of the gas g and particle p phases; this film layer has no thermal mass. Second, there is the primary insulation layers (a design with four insulation layers is shown in Figure 15). These layers have thermal mass such that they absorb, store, and release thermal energy throughout the simulation. Insulation layer j is assumed to have a mean temperature at the center of the given insulation layer T_{lj} . Lastly, there is the convective thermal resistance R_{conv} between the exterior wall of the particle storage silo and ambient. Gas and particle temperatures, T_g and T_p , respectively, are the connection points between the insulation and silo submodels. Ambient temperature T_{amb} is defined by the user and can be constant for transient based on a weather file.

The film layer thermal resistances are defined as follows:

$$R_{f,g} = \frac{\delta_{f,g}}{\pi D_{silo} H_g k_g} \quad (21)$$

$$R_{f,p} = \frac{\delta_{f,p}}{\pi D_{silo} H_p k_p} \quad (22)$$

The thermal resistance between node I and layer j is as follows:

$$R_{i,lj} = \frac{\ln \left[\frac{r_{silo} + \sum_{j=1}^{j-1} \delta_j + \frac{1}{2} [2 - (j - i)] \delta_j}{r_{silo} + \sum_{j=1}^{j-1} \delta_j + \frac{1}{2} [1 - (j - i)] \delta_j} \right]}{2\pi H_{silo} k_j} \quad \forall j \in J, i \in \{j - 1, j\} \quad (23)$$

Each insulation layer has two thermal resistance terms: one for the inner half of the cylindrical layer and one for the outer half of the cylindrical layer. The thermal mass of the insulation layer is defined to be located entirely at the midpoint through the insulation layer. The energy balance on insulation layer j is as follows:

$$m_j c_{p,j} \left(\frac{dT_{lj}}{dt} \right) = Q_{j-1,lj} + Q_{j,lj} \quad (24)$$

The thermal conductivity k_j , density ρ_j (in order to compute the mass of insulation layer j , m_j), heat capacity, $c_{p,j}$, of the material and the thickness, δ_j , in each insulation layer j is defined by the user.

The natural convection thermal resistance is defined as:

$$R_{conv} = \frac{1}{A_{silo} h_{conv}} \quad (25)$$

where A_{silo} is the total exterior surface area (top, side, and bottom) of the storage silo [m^2] and h_{conv} [W/m^2-K] is defined as the area-weighted average of the heat transfer coefficients for each side of the silo (top, side, and bottom), which are based on established correlations by default or can be specified explicitly by the user.

2.3.2 Validation

This ROM was validated using the approach shown in Figure 6 (page 7). An experimental TES bin built by the NREL ENDURING¹ team supported by the ARPA-E DAYS program had already validated a transient finite element analysis (FEA) model at experimental scales. The validated transient FEA model was used to simulate performance of a commercial-scale particle storage silo. The commercial-scale FEA model of the particle storage silo provided data with which the Modelica-based model was compared.

For the validation simulation, the initial insulation temperatures were assumed to be the same as the ambient temperature (20°C). The particle domain was initialized at a set temperature point and filled the storage volume. The top, side, and bottom natural convection heat transfer coefficients were the same for both models (7.0, 5.0, and 2.0 W/m^2-K respectively), in accordance with established natural convection correlations. Both models then simulated 7 days of cooling.

¹ ENDURING: Economic Long-Duration Electricity Storage by Using Low-Cost Thermal Energy Storage and High-Efficiency Power Cycle

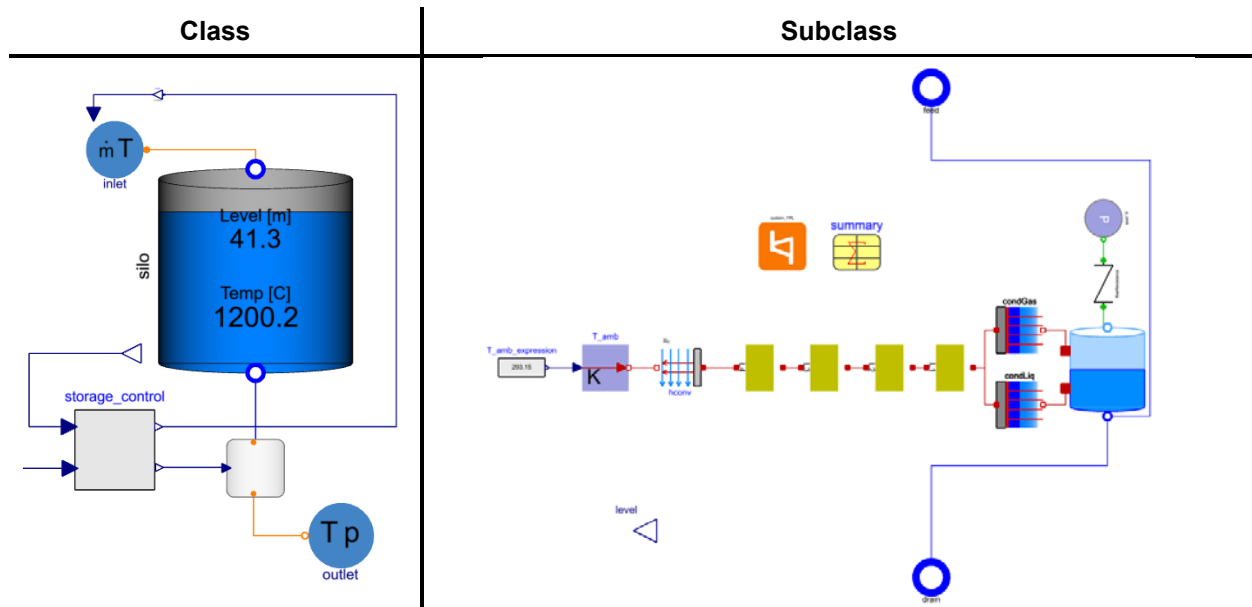


Figure 16. Fully packaged particle storage array model with connection points (class) and individual components and structure that comprise the particle storage array model (subclass)

The two models were compared on their prediction of a key metric: non-dimensional particle temperature over time:

$$T^*(t) = \frac{T_p(t) - T_{amb}}{T_p^0 - T_{amb}} \quad (26)$$

The results of this validation study are shown in Figure 17; the T^* predicted by the Modelon Impact TES model, the FEA model, and $\pm 10\%$ and $\pm 2\%$ error (based on the FEA model) are all shown. The Modelon Impact TES model is within 2% of the FEA model over the entire 7-day simulation.

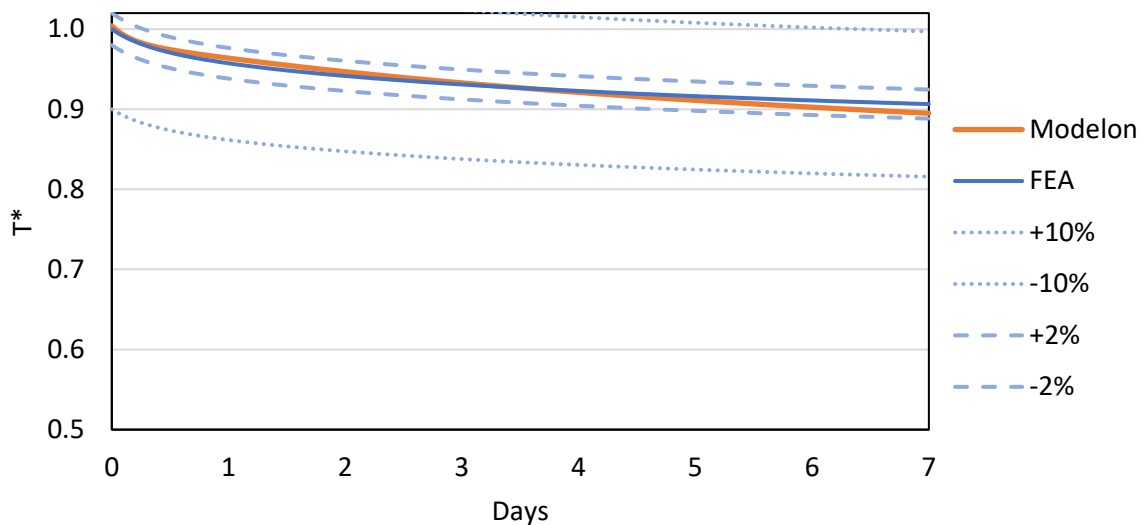


Figure 17. T^* of the particle storage silo over a 7-day cooling process

It is important to note that the T^* results shown in Figure 17 are not necessarily representative of the particle storage efficiency during normal operation. During normal operation, the insulation materials have greater thermal mass (e.g., the first refractory layer will not be starting at 20°C every time the storage silo charges; it will heat up over several operating cycles). However, this study still validated the Modelon Impact-based ROM of the particle storage silo by showing the thermal performance predicted by the ROM and the high-fidelity FEA model are the less than 2% difference.

2.4 Particle-Air, Pressurized, Fluidized Bed Heat Exchanger (PFB HX)

A particle-air, pressurized, fluidized bed heat exchanger (PFB HX) model was developed for SIPH systems that supply hot air for industrial processes such as moisture removal, drying, curing, and preheating air for kilns. Currently, hot air is often produced by burning natural gas, which is a source of air pollution and carbon emission and is hard to decarbonize. A CST with particle TES system using a PFB HX to discharge hot air could provide a potentially lower-cost source of hot air supply for industrial processes in high solar radiation regions, particularly raw material refining in mining-related applications such as iron ore mining, cement production, and alumina production.

The PFB HX modeled here entails direct-contact between the fluidizing gas and particles, thereby eliminating intermediate heat transfer surfaces and enabling highly effective heat transfer. Fluidizing gas and particles can achieve a counterflow configuration with gas and particle separation achieved through gravitation and cyclone separation; thus, it is an efficient and low-cost particle-air heat exchanger that could directly integrate with industry use cases that require continuous hot air supply when connecting with a particle TES system.

2.4.1 Modeling Approach

The PFB HX was modeled as a 0D counterflow heat exchanger. In the modeled system, heated particles enter from the hot storage silo and exit to a skip hoist that brings the cooled particles to the top of the cold storage silo. Air is compressed to the PFB HX operating pressure before entering the PFB HX. The PFB HX heats the air to near the particle inlet temperature due to the effective counterflow design. The heated, compressed gas exits the PFB HX and then passes through a cyclone separator array and any remaining entrained particles are removed.

Figure 18(a) shows an internal design of a PFB HX concept from the ENDURING project that could supply hot air for industrial processes using the hot particles [13]. The pressurized fluidized bed heat exchanger (PFB HX) accounts for mass, energy, and momentum balance. The model assumes steady-state operation with no internal mass or thermal inertia.

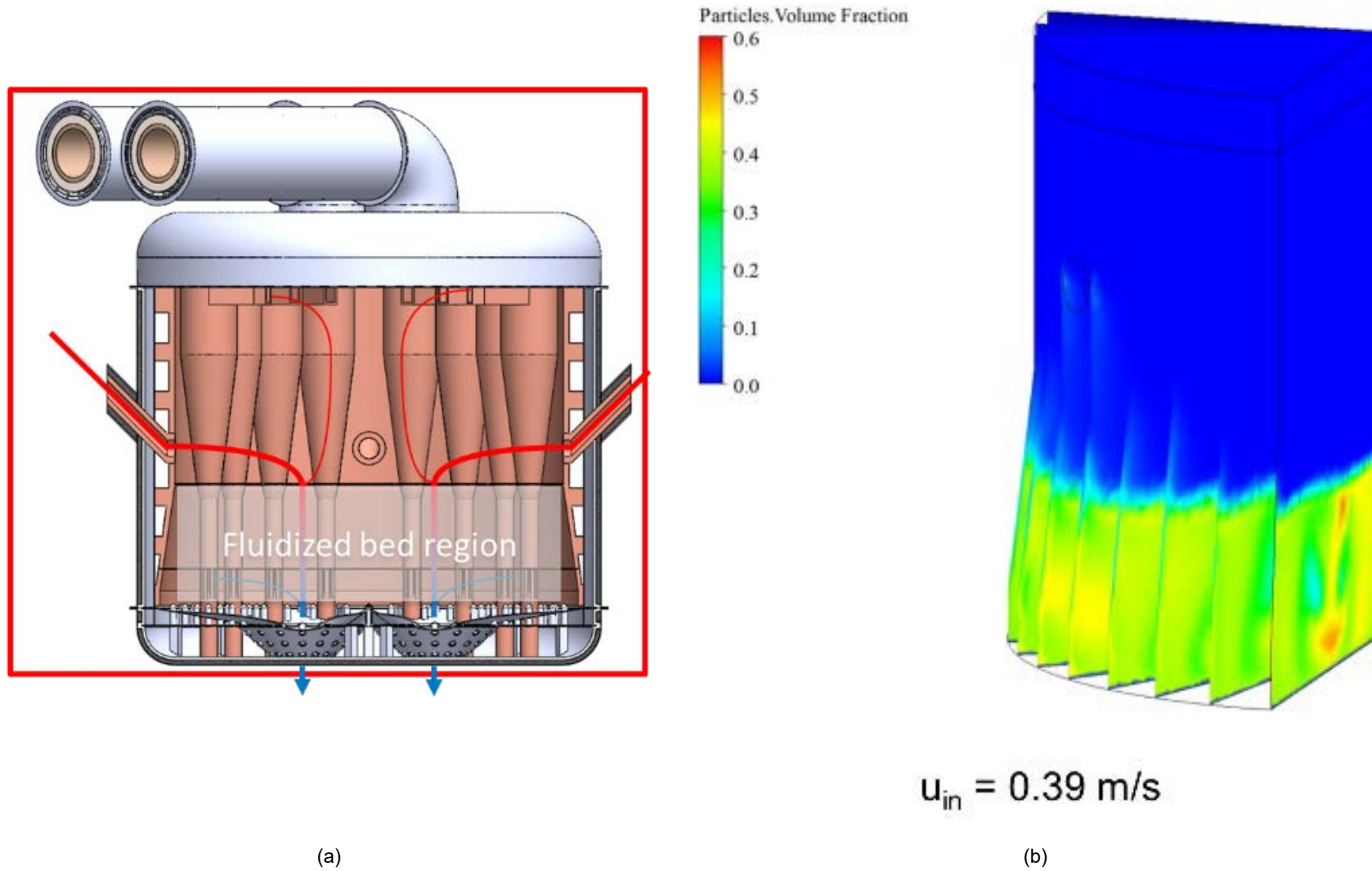


Figure 18. PFB HX concept developed at NREL (a) and computational fluid dynamics (CFD) model of the PFB HX concept design (b)

The energy balance assumes there is no thermal loss. Therefore, the energy balance for the particle and gas streams is as follows:

$$Q_{gp} = \dot{m}_p(h_{p,o} - h_{p,i}) \quad (27)$$

$$Q_{pg} = \dot{m}_g(h_{g,o} - h_{g,i}) \quad (28)$$

where $Q_{gp} = -Q_{pg}$. In this application, the heat transfer from particle to gas Q_{pg} is a positive value as the particle is the “hot” stream and the gas is the “cool” stream.

The heat transfer between the two media Q_{pg} is determined by the effectiveness of the heat exchanger ε which is computed by the following algorithm:

$$C_i = \dot{m}_i C_{p,i} \quad (29)$$

$$C_{min} = \min(C_p, C_g) \quad (30)$$

$$C_{max} = \max(C_p, C_g) \quad (31)$$

$$C = \frac{C_{min}}{C_{max}} \quad (32)$$

$$NTU = \frac{UA_{heat}}{C_{min}} \quad (33)$$

$$Q_{max,i} = \dot{m}_i [h_i(T_{p,in}) - h_i(T_{g,in})] \quad (34)$$

$$Q_{max} = \max(Q_{max,p}, Q_{max,g}) \quad (35)$$

$$\varepsilon = \begin{cases} \frac{NTU}{NTU + 1} & \text{if } C \approx 1 \\ \frac{1 - e^{-NTU(1-C)}}{1 - Ce^{-NTU(1-C)}} & \text{otherwise} \end{cases} \quad (36)$$

$$Q_{pg} = \varepsilon Q_{max} \quad (37)$$

The overall heat transfer coefficient U and the heat transfer area A_{heat} are input parameters and calibrated against the results from an existing, benchmarked CFD model of the PFB HX CFD.

The momentum balance equations are solved for both streams in this model. The particle stream is modeled as a frictionless pipe and therefore the pressure drop across the inlet and outlet is zero for the particle phase; the particle flow is driven solely by the skip hoist (i.e., a particle “pump”). The gas stream pressure drop is based on established correlations for fluidizing gas in fluidized beds. The mathematical description of this correlation is as follows:

$$dP_{g,bed} = \begin{cases} dP_{mf} & u_{in} \geq u_{mf} \\ \left(\frac{u_{in}}{u_{mf}}\right) dP_{mf} & u_{in} < u_{mf} \end{cases} \quad (38)$$

Gas bed pressure drop is constant once inlet gas velocity, u_{in} , has exceeded the minimum fluidization velocity, u_{mf} . Gas bed pressure drop at minimum fluidization, dP_{mf} , is equivalent to pressure drop due to the downward gravitational force of the particles:

$$dP_{mf} = \frac{m_{bed}g}{A_{bed}} = \rho_{bed,static}H_{bed,static}g \quad (39)$$

Minimum fluidization velocity can be calculated using the Ergun equation:

$$u_{mf} = \frac{(\psi d_p)^2}{150\mu} [g(\rho_s - \rho_g)] \frac{\varepsilon_{mf}^3}{1 - \varepsilon_{mf}} \quad (40)$$

where ρ_s is the solid particle density, ρ_g is the gas density at inlet conditions, g is the gravitational constant (9.81 m/s²), μ is gas viscosity at inlet conditions [N-s/m²], ψ is the particle shape factor, d_p is the Sauter Mean particle diameter, and ε_{mf} is the void fraction at minimum fluidization defined by:

$$\varepsilon_{mf} = \left(\frac{0.071}{\psi}\right)^{\frac{1}{3}} \quad (41)$$

The PFB HX includes gas-phase pressure losses due to the cyclone separator array. The model results determined the number of cyclones in the array. The cyclone separator array model is a standard flow resistance model. The actual gas-particle separation physics is omitted. Thus, the sole impact of the cyclone separator array is the pressure drop experienced by the gas upon exiting the primary heat transfer region of the PFB HX. The gas/particle pressure drop across the cyclone is given by:

$$dP_{g,cyclone} = \frac{1}{2} k_{tot} \rho_g u_{in,cyclone}^2 \quad (42)$$

The model has a cyclone array with n number of cyclones. Because gas streams pass through only one of n cyclones the total pressure drop of the gas stream is that of a single cyclone. The number of cyclones in the array just determines the quantity of gas (mass flow rate) that passes through a single cyclone; all cyclones are assumed to have the same mass flow rate (i.e., $1/n^{\text{th}}$ of the total gas mass flow rate goes through a single cyclone). The pseudo-friction factor k_{tot} for the cyclones is calculated by established correlations based on the geometry of the cyclone. All geometric parameters are available in this model. The PFB HX model is flexible and can consider a simple percentage loss for the cyclone separation array if the full geometric parameters are unknown to the user. Additional pressure losses (i.e., gas distributor and minor losses) are included as constant parameters as well.

The total pressure loss between the gas-phase inlet and outlet is therefore defined as:

$$dP_g = P_{g,in} - P_{g,out} = dP_{g,bed} + dP_{g,cyclone} + dP_{g,distributor} + dP_{g,minor} \quad (43)$$

2.4.2 Validation

The validation of the PFB HX model built in Modelon Impact used the results from the commercial-scale CFD model built during the ENDURING project. The Modelon Impact-based PFB HX model was validated for two key metrics: bed pressure drop and effectiveness. These metrics were chosen because they are the two most important metrics that impact overall system performance. Figure 19 shows the results of this comparison for both metrics over a range of inlet velocities. The Modelon Impact-based PFB HX model is well within 10% of the high-fidelity CFD model for all inlet velocities tested.

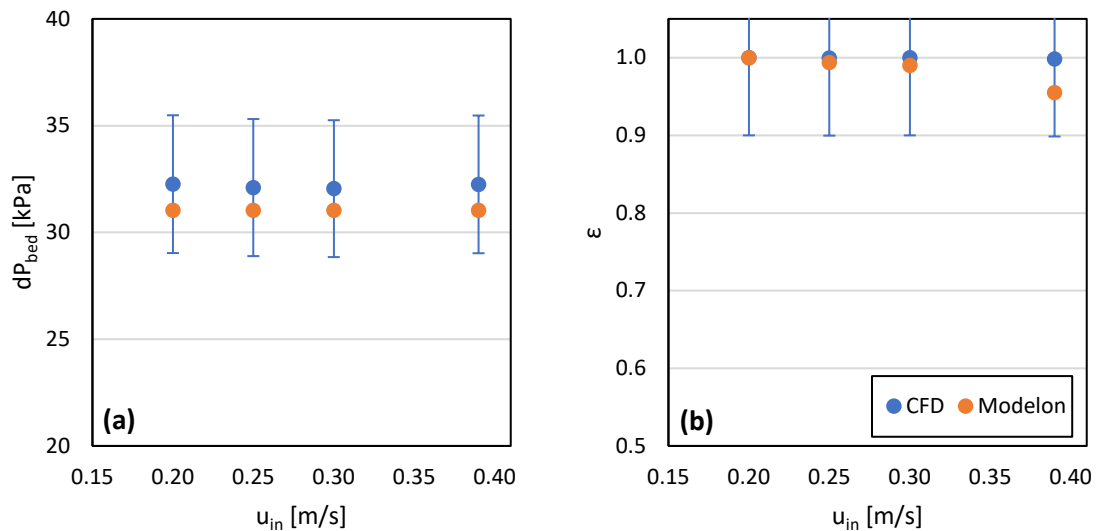


Figure 19. Comparison of (a) gas-phase bed pressure drop and (b) effectiveness predicted by high-fidelity CFD and Modelon Impact-based models of the PFB HX with 10% error bars

2.5 Particle Steam Generator

As mentioned, a common SIPH application is the supply of hot steam. Because steam can be used directly, used as a heat transfer media, and used for combined heat and power, a particle steam generator provides a way for the particle-based TES system to integrate with this major SIPH application.

2.5.1 Modeling Approach

The steam generator model is composed of three counterflow heat exchangers, a drum volume, and a recirculation pump. The full, flattened model is represented by the icon in the left box of Figure 20. The detailed structure and connections of sub-components is shown in the right box of Figure 20.

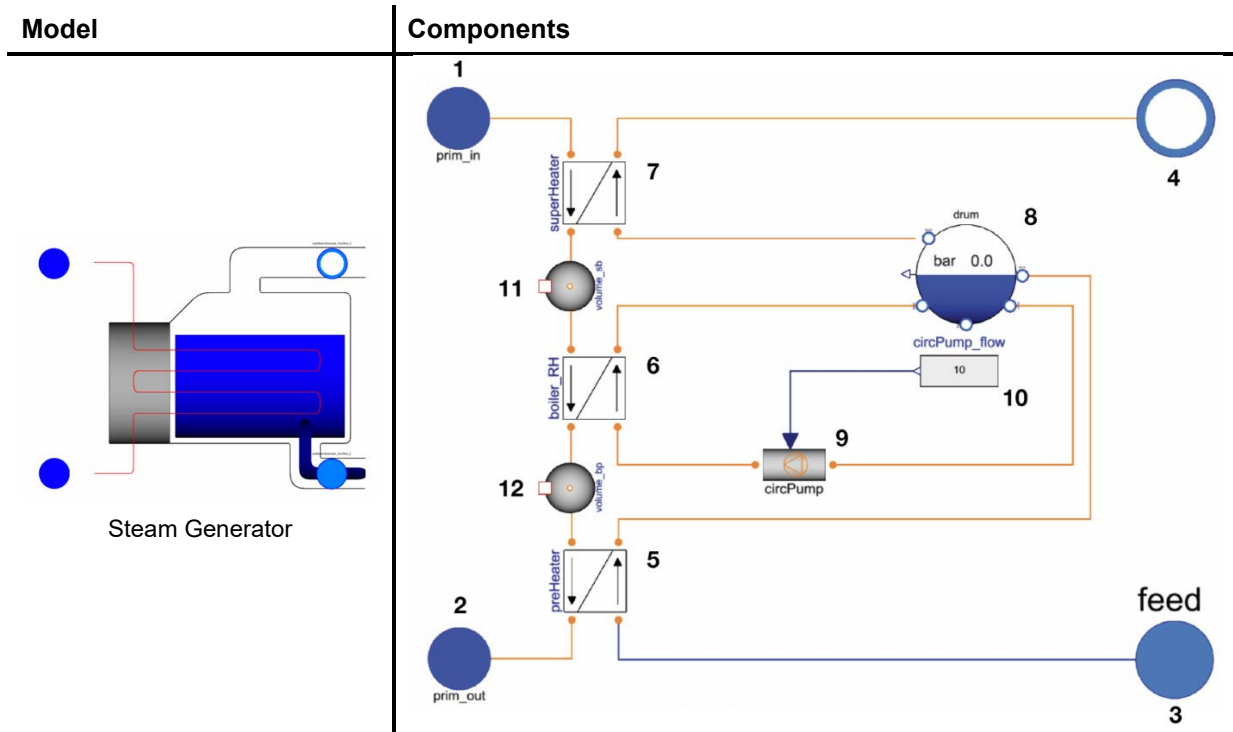


Figure 20. Top-level steam generator model (left) and structure of the component model (right)

Mass flow, pressure, and enthalpy boundary conditions for the water are prescribed with the feed (3 in the figure) and steam (4) port components. Similar boundary conditions for the silica sand are prescribed with the prim_in (1 in the figure) and prim_out (2) port components. Heat is transferred from the sand into the water through a series of three heat exchangers: a preheater, a boiler, and a superheater. Between the preheater and superheater, the boiler heats two-phase water in a constant circulation loop, which is regulated by a circulatory pump with a fixed mass flow rate. A steam drum is used to separate steam from the two-phase water mixture. Each heat exchanger is a counterflow configuration between the water and particle mediums, and each one uses the same effectiveness-NTU (number of transfer units) algorithm as the particle-to-air heat exchanger. However, these heat exchangers do not have a direct-contact approach; instead the water and particle mediums are separated by piping. The pipes contain the water medium, and the particle medium is on the exterior of the pipes.

The heat transfer coefficient in each of heat exchanger is defined as the composite of convection between the particle and pipe walls and the water and pipe walls and conduction through the pipe walls.

$$U = \frac{1}{R''} \quad (44)$$

$$R'' = \frac{1}{U_{particle-wall}} + \frac{\partial_{wall}}{k_{wall}} + \frac{1}{U_{water-wall}} \quad (45)$$

where $U_{particle-wall}$ and $U_{water-wall}$ is the convective heat transfer coefficients [W/m²-K] between the pipe wall and the particle and water medium respectively, ∂_{wall} is the thickness of the wall [m], and k_{wall} is the thermal conductivity of the wall material [W/m-K]. All these are parameters of the individual heat exchangers in the particle-based steam generator model with defaults prescribed based on industry partner values.

2.5.2 Validation

The steam generator component was validated based on boundary condition and parametric data from a previous collaboration with Babcock & Wilcox. The Babcock & Wilcox data are the result of an economic and performance analysis of a similar steam generator, seen in Figure 21. The Babcock & Wilcox steam generator used silica sand as the particle medium. That model explored different superheated steam production scenarios, based on the mass flow of both the silica sand and the inlet feedwater.

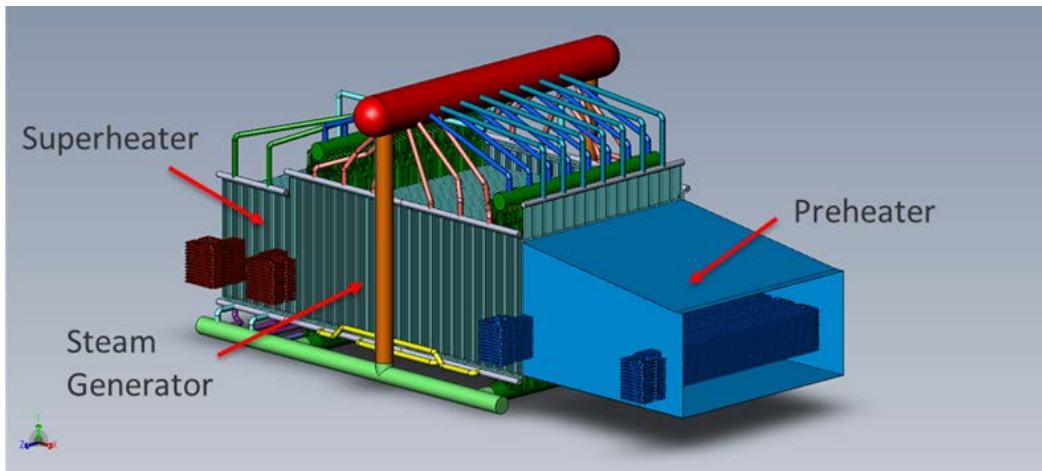


Figure 21. Illustration of a design of a particle steam generator from Babcock & Wilcox, which provided validated data

To test the validity of the steam generator, six design “configurations” were modeled based on prevalidated data sourced from a DOE-supported SunShot project partnered between NREL and Babcock & Wilcox. These data provided the boundary conditions required to compute the mass balance equations: \dot{m}_{sand} , $T_{sand,in}$, $T_{sand,out}$, \dot{m}_{water} , $h_{water,in}$, $h_{steam,out}$. Here $h_{water,in}$ and $h_{steam,out}$ are determined from the steam tables, based on the given temperature and pressure of the water at the system inlet and outlet. As shown in Figure 22, the ROM steam generator predicts an outlet steam temperature within 1% of the temperature from Babcock & Wilcox design configurations.

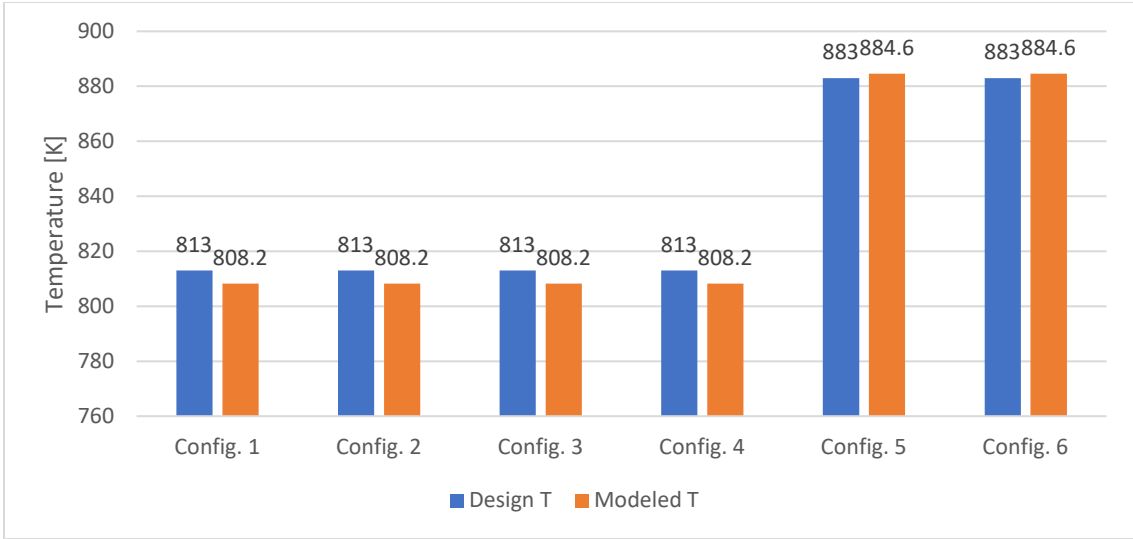


Figure 22. Babcock & Wilcox design steam temperature versus modeled steam temperature in Modelon Impact

3 SIPH Applications and System Modeling

With the library of component models developed and validated, integrated system models could be created in Modelon Impact. However, before building a system model, we first identified application and operation conditions to be used for system simulation and techno-economic analysis.

3.1 SIPH Applications and System Configurations

Most industry heat uses pressurized steam or hot water. Some processes need hot air for drying or curing. Mining and material processing may heat and cool particulate types of materials. Industry use cases were collected through a literature review and industry surveys to establish the particle TES configurations for the SIPH system. Table 5 summarizes use cases for SIPH. The charge processes for various cases all rely on heating particles and then storing the heated particles in insulated containment. The SIPH system was designed to meet industrial process load with discharge method being considered in operation.

Table 5. Scenarios Using Steam, Hot Air, and Hot Particles for Industrial Processes

Heating Media	Applications	SIPH Discharge	Notes
Hot particles	Preheating ores for steel, alumina, cement production	Direct heating and discharge	Heating particles as direct usage
Hot air	Material Processing: from drying to materials separation	Pressurized fluidized bed	Only open cycle, such as curing or drying
Steam	Broad from food processing to enhancing oil recovery, refinery	Particle/steam boiler	Open versus close steam loop and use
Cogeneration	Most common in needing steam, hot water, and power	Particle/steam boiler	May have grid connection for service

Various charging modes involving solar energy of CST and PV possible (Figure 23). PV may be collocated with CST, and grid renewable electricity would be connected as a renewable energy source and electric price signal for charging. PV or grid electricity charges TES by an electric particle heater, which has been developed in the NREL ENDURING project supported by the ARPA-E DAYS program. The electric heater and solar particle receiver can be arranged in parallel (C.2) or series (C.3); both configurations would require distinct operations and controls to ensure the desired particle charge temperature is achieved. Direct heating particles from a particle solar receiver can be effective and efficient, but it is most often only used in solar tower configurations. Line-focus solar field technology such as parabolic troughs or linear Fresnel systems often uses liquid heat transfer fluids. To couple with particle TES, a liquid-particle heat exchanger may be needed to heat particles from solar heat.

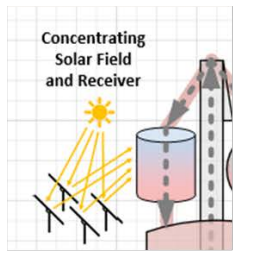
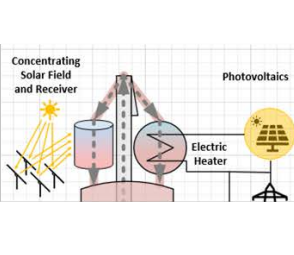
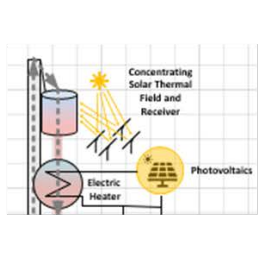
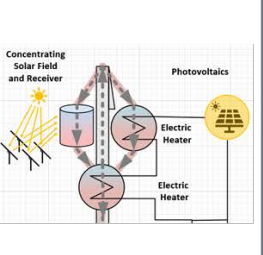
	C.1 CST heating only	C.2 CST parallel PV Heating	C.3 PV topping CST	C.4 PV Top-Parallel CST
Pros	<ul style="list-style-type: none"> A low-cost approach for full spectrum solar flux Heat-to-heat conversion minimizes intermediate heating and devices. 	<ul style="list-style-type: none"> Flexible with CST as option for areas with low Solar DNI. 	<ul style="list-style-type: none"> Adding exergy value of heating 	<ul style="list-style-type: none"> Combining C.1, C.2, C.3 cases
Cons	<ul style="list-style-type: none"> Geographic restriction to high DNI areas 	<ul style="list-style-type: none"> Electric heating be a more expensive energy source 		<ul style="list-style-type: none"> More charge and control devices
Illustrations				

Figure 23. Four charging configurations of hybridizing CST and PV (or grid power) through solar receiver and electric charging particle heater

Figure 24 shows exemplary discharging paths for hot particles, hot air, hot water, and steam. Heating particles and discharging hot particles are direct processes of charging/discharging heat and need minimal equipment and is likely the lowest-cost storage for SIPH. Direct heating particles can help clean up particles by removing moisture or low-volatility materials and to preheat temperatures for subsequent processes. Using processing materials as storage media as shown in Figure 24(a) also saves materials and interface heat exchangers for low thermal losses and costs. Particle heating can support particulate material processing such as cement production, steel ore mining, and alumina refining.

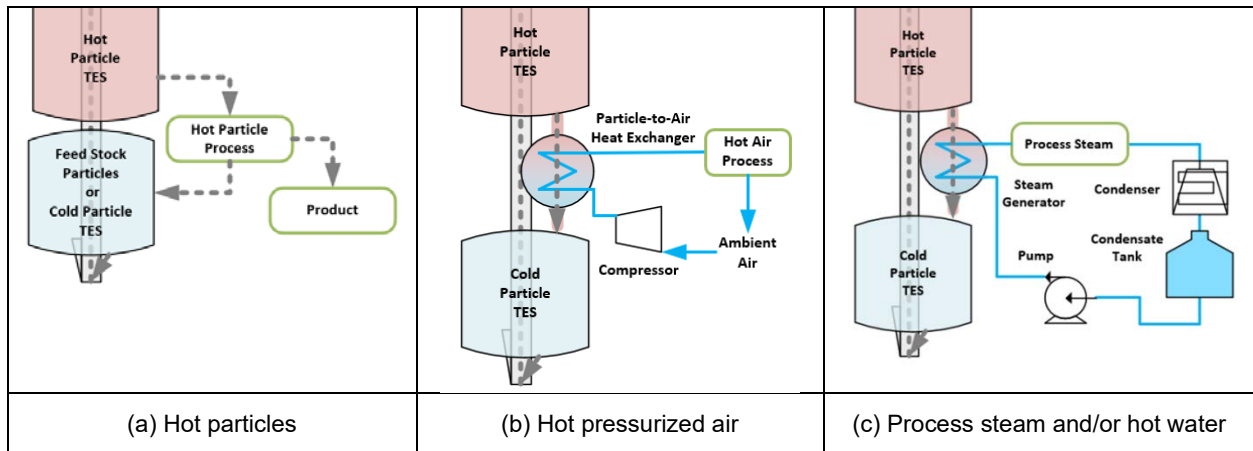


Figure 24. Discharge stored energy to (a) hot particles, (b) hot air, and (c) hot water or steam in various industry uses conditions

Figure 24(b) shows the supply of hot air from particle TES. Heating air by a direct air/particle contact pressurized fluidized bed (PFB) heat exchanger (HX) was developed by the NREL project team in the ARPA-E DAYS and proved it is a feasible technology. It is also highly efficient and cost-effective because it eliminates interface heat transfer surfaces. Hot air supply can have broad industry uses in drying, curing, or preheating air for kiln or furnace heating processes. Figure 24(c) shows the supply of hot water or pressurized steam from a particle/water

heater or particle/steam boiler. Hot water or pressurized steam is a leading industrial use case and, therefore, the focus of the system modeling demonstration below.

3.2 System Simulation

Two integrated system models were developed to provide heated steam and power. Figure 25(a) and (b) show the heated steam system and its equivalent in Modelon Impact respectively. This system configuration has parallel charging from CST and solar PV resources (see the description of C.2 in Figure 23). The Modelon Impact model does not have a grid connection in this instance.

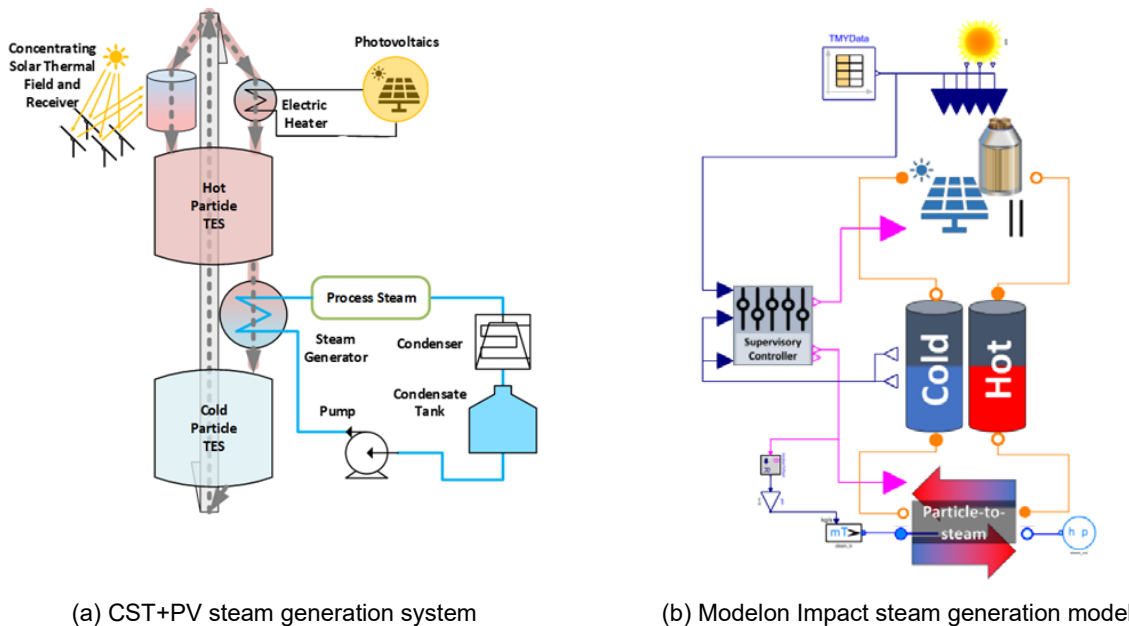


Figure 25. Industrial steam generation (a) system diagram and (b) system model in Modelon Impact

A new supervisory controller was developed to provide continuous steam supply at desired temperatures and pressures throughout an entire year without any foresight. The controller monitors real-time storage levels and solar resources to manage the flow of particles. The storage silos act as a buffer between the solar resource charging transients and the ideally steady discharging flow rate. The real-time controller approach provides insight into system operations and nuanced results about the ability of the given system design to meet load continuously throughout the year. A base set of results from the heated steam system is presented below.

Two system durations were examined: 24-hr and 100-hr. 100-hr energy storage durations have been shown in the literature to be needed to meet most baseload demand for electrical power plants from variable renewable resources such as solar [14]. The model simulated an entire year of operation. Figure 26(a) shows the solar resource profile over a 14-day window of the entire year that was used for both durations examined.

Figure 26(b) shows how the storage level changes throughout the year based on the controller’s logic that manages charging and discharging based on real-time signals. Both cases are

initialized at only a 10% state of charge and operate near a full state of charge throughout the middle of the year (i.e., day 100 to day 250). The 100-hr case's large storage capacity results in the system missing fewer hours in the last 2 months of the year than the 24-hr case; see Figure 26(c). The 24-hr and 100-hr cases miss the steam load demanded of them a total of 456 hours and 373 hours throughout the year respectively.

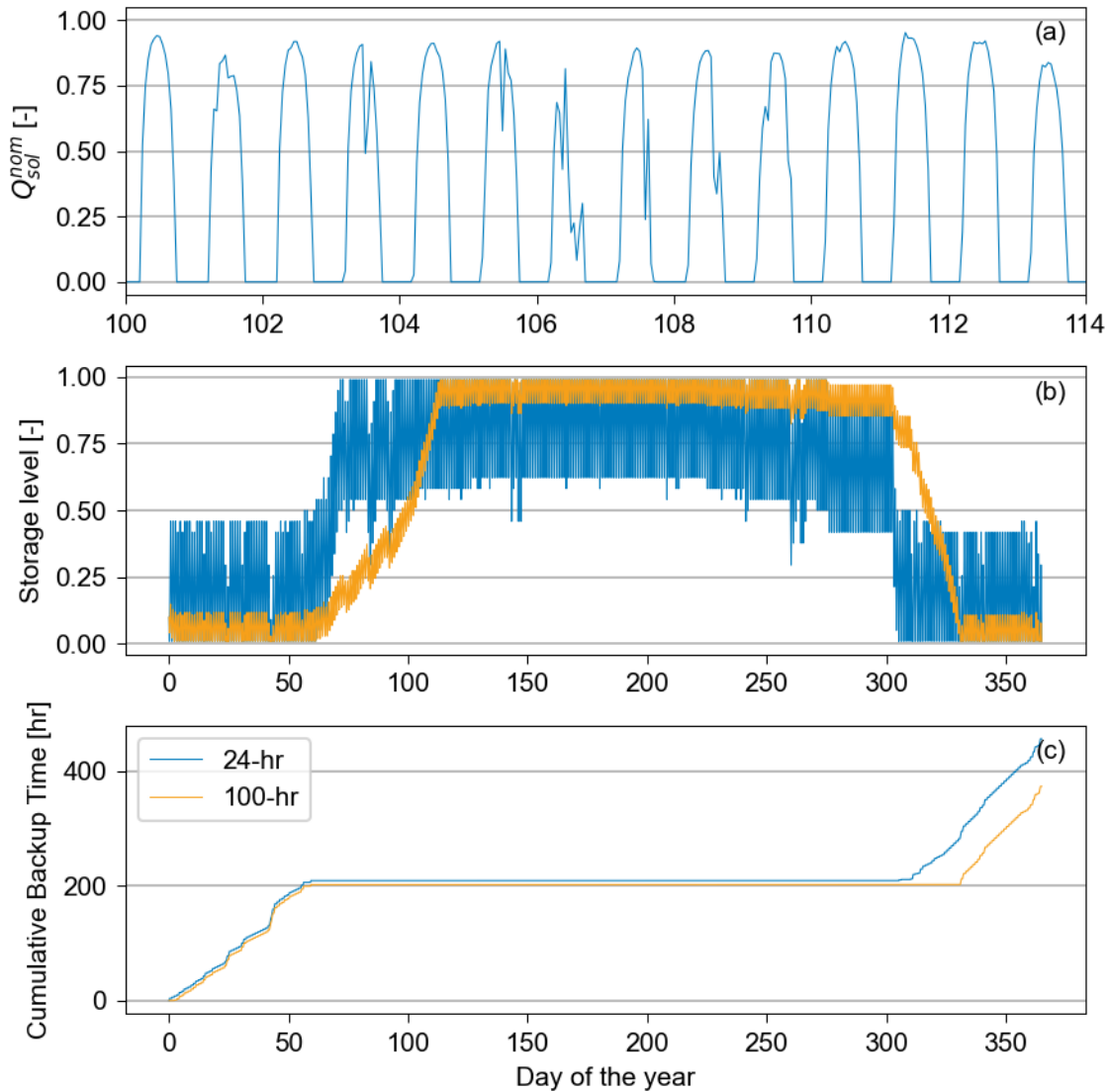


Figure 26. Results produced by the steam generation Modelon Impact system modeling tool for a system with 24-hr (blue) and 100-hr (yellow) storage durations: (a) nominal solar input over a 14-day window of an annual simulation (same for both cases), (b) nominal storage level across the entire year, and (c) cumulative hours of time where backup (i.e., grid heating or fossil fuels) would be required to meet constant load demand

The results show the Modelon Impact system modeling tool provides nuanced data (i.e., subhourly) about when the load cannot be achieved. The challenge of sizing the SIPH system will be determining the marginal cost of missing load versus the marginal cost of increasing storage capacity and solar generation. To serve the desired load 24/7, the SIPH system must be designed with enough storage capacity to serve the longest duration of low solar energy generation and to be feasible at the same time. These results illustrate that individual component models have been successfully integrated, a system controller has been developed, and transient system modeling tool can provide useful insight into system operation and performance. To enhance the tool's capabilities, Python code was developed to wrap around the Modelon Impact model through a functional module unit. It is an executable that can be exported from Modelon Impact, used without the need for a license, and ease connection with external codes and software.

4 Techno-Economic Analysis and Case Study of HEATER System Configurations

To evaluate techno-economic aspects of HEATER energy systems, an Excel-based, optimal sizing and costing tool was developed. It was used to optimally size six system technology compositions (Table 6), henceforth called scenarios, for various case studies. To set up the energy system capacity and meet process demands, a Searles Valley Minerals, Inc. (SVM) site was used as the basis for these analyses. The SVM facility is in southeast California just south of Death Valley National Park. This site receives annually 2,822 kWh/m² and 2,107 kWh/m² of direct normal and global horizontal solar irradiance respectively. With an abundant solar resource and available land area of approximately 250 acres, the site is an ideal case study location for this technology.

Table 6. PV/CSP/TES Scenarios Evaluated in this Project

Scenario	CSP	PV	TES	TES Charging by Grid	Grid as Backup
1	yes	yes	yes	yes	yes
2	yes	no	yes	yes	yes
3	yes	yes	yes	no	yes
4	yes	no	yes	no	yes
5	no	no	yes	yes	yes
6	no	no	no	no	yes

Scenarios 1 and 2 include full grid connection with charging TES. Scenarios 1 and 2 allow the system to additionally charge thermal storage from grid electricity during any hours in which the price falls below a designated cutoff. The model accounts for tradeoffs between capital cost for oversized CSP, PV, and/or TES components and the cost of grid electricity by minimizing the levelized cost of heat (LCOH) of the system. The cases are highly dependent on the grid. Scenarios 3 and 4 fulfill the heat demand via the combined on-site CSP, PV, electric heater, and TES system, and they draw electricity from the grid only during those hours in which the CSP/PV/TES system cannot meet the demand. Scenarios 5 and 6 do not include CSP or PV assets, and only use grid electricity either with or without TES. In Scenario 6, the system must simply pay the current cost of grid electricity in all hours, while in Scenario 5 the system charges TES from the grid in any hour below a designated price threshold, uses the stored TES when available, and reverts to grid backup when TES is depleted. All scenarios presume the price of grid electricity is fixed at any given hour and that there is no feedback between electricity utilization and electricity price.

Note that the results for all scenarios are sensitive to assumptions regarding hourly cost of grid electricity. Here recent historical data for locational marginal price (LMP) price near the SVM site were used to define the time variation of electricity price; however, this can be expected to change as the composition of the grid shifts toward a greater fraction of renewable technologies.

4.1 Cost Analysis Method

The tool seeks to minimize the LCOH of the system via selection of the CSP capacity, PV capacity, and TES capacity for each scenario. LCOH was defined as:

$$LCOH = \frac{C_{tot} + \sum_{y=1}^{LS} \frac{O\&M}{(1+d)^y} + \sum_{y=1}^{LS} \frac{\sum_{h=1}^{8760} GT^h \times E_{th,grid}^h / \eta_{heater}}{(1+d)^y}}{\sum_{y=1}^{LS} \frac{\sum_{h=1}^{8760} D_{th}^h}{(1+d)^y}} \quad (46)$$

Table 7 describes each term in the LCOH calculation alongside base case input assumptions.

Table 7. Descriptions of Terms Used in the LCOH Calculation

Parameter	Description	Data Source or Assumed Base Case Value
C_{tot}	Summation of capital costs for all system components	Component cost inputs and cost functions in Table 8
$O\&M$	Operation and maintenance costs	Component operation and maintenance assumptions in Table 9
D_{th}^h	Hourly thermal demand	Defined by the required heat load profile for the case study
$E_{th,grid}^h$	Hourly electricity drawn from the grid	Calculated by the annual model
GT^h	Hourly cost for grid electricity purchases	Historical hourly LMP for the SVM site in 2021, modified as shown in Eq. (47)
GT_{PPA}	Median grid electricity price	0.04 \$/kWh
LS	Lifespan of the system	25 years [15]
d	Nominal discount rate	10% [13]

The hourly price of grid electricity was set via Eq. (47):

$$GT^h = (LMP^h / \text{median}(LMP^h)) \times GT_{PPA} \quad (47)$$

where LMP^h is the historical hourly marginal electricity price, which was obtained from the California Independent System Operator [16] for the location of SVM (Node SEARLES_7_N004) in 2021.

4.1.1 Component Cost and Operating Cost Assumptions

Table 8 provides the base case cost assumptions for all system components. Base case-specific costs of the solar components (CSP heliostat field, CSP receiver, PV field) are similar to the U.S. U.S. Department of Energy (DOE) SunShot 2030 “high-performance” case [17]. Cost functions for the particle heater, TES, skip hoist, and discharging components were derived by iterating detailed component design calculations described in [13] over a range of unit capacity, pressure, and temperature conditions. The functions shown in Table 8 were fit to the resulting set of calculated costs. Note that the total capital cost used in the LCOH calculations here accounts for

only the bare-erect component costs, and it does not include estimates for site, building, system integration, contingency, EPC cost, debt costs, sales tax, etc.

Table 8. Empirical Formulas and Base Case Cost Inputs Used to Estimate the Capital Cost of SIPH Components

System	Subsystem	Empirical Formulas
CSP Field	Heliostat	$C_{hel} = SC_{hel} \times A_{hel}$, where $SC_{hel} = 80$ \$/m ² , which accounts for site preparation, land cost and heliostat cost [17]
Particle Receiver	Receiver	$C_{rec} = SC_{rec} \times Cap_{CSP}$, $SC_{rec} = 124$ \$/kWth [18]
	Tower	$C_{tower} = C_{tower, fixed} \times e^{(0.0124 \times H_{tower})}$, here $C_{tower, fixed} = 1194000$ \$ and H_{tower} is the tower height which was found using SolarPilot [19]
PV	—	$C_{PV} = SC_{PV} \times CAP_{PV}$ where $SC_{PV} = 773.7$ \$/kW [17]
Particle Heater	Heating wire	$C_{wire} = 21192CAP_{heater}$
	Insulation material	$C_{insulation} = 291.71CAP_{heater}$
	Refractory material	$C_{refractory} = 344.67CAP_{heater}$
	Control box	$C_{control} = 0.2 \times (C_{refractory} + C_{insulation} + C_{wire})$
TES	Silo containment	$C_{const} = 217930.89Cap_{silo}^{0.26}$
	Insulation material	$C_{insulation} = a \times T_h - b$ $a = -4.86 \times 10^{-6} \times Cap_{silo}^2 + 0.54897 \times Cap_{silo} + 323.42$ $b = -0.001 \times Cap_{silo}^2 + 153.065 \times Cap_{silo} + 97539.568$
	Media	$C_{media} = 35Cap_{silo}$
Skip Hoist	—	$C_{skip} = a \times \dot{m}_{part}^2 - b \times \dot{m}_{part} + c$ $a = 10.352 \times \ln(H) - 36.649$ $b = 8.3029 \times H - 462.64$ $c = 1787.962 \times H + 294134.6$
PFB HX	Pressure Vessel (FBPV)	$C_{FPV} = a \times Cap_{CSP}^b \times 0.43^b$ with $a = 1599.6 \times P + 566.06$ and $b = -0.0086 \times P^2 + 0.0532 \times P + 1.4323$
	HX	$C_{HX} = 108574 \times Cap_{CSP}^{0.9223} \times 0.43^{0.9223}$
	Cyclone	$C_{cyc} = 1477.9 \times Cap_{CSP} \times 0.43 - 426.12$
	Piping	$C_{piping} = (a \times Cap_{CSP} \times 0.43 + b)^2 \times L$ with $a = 0.1121 \times P + 1.4667$ and $b = -1.451 \times P^2 + 19.82 \times P + 8.661$
Particle Steam Boiler	U-tube HX	$C_{SB} = (4.22P^2 + 30.8P + 1157) \times A_{SB} + 250.92P^2 + 1831.9P + 68784$
Power Cycle	Including balance of power	$C_{power} = Cap_{power} \times SC_{power}$ with SC_{power} equals to 745 USD/kW

Base case assumptions for the operation and maintenance of the various components are listed in Table 9.

Table 9. Operation and Maintenance Costs of SIPH Components

System	Operation and Maintenance Cost	Reference
CSP	9 \$/kW _{th}	[17]
PV	5 \$/kWe	
Other Components	5% of their capital cost	N/A

Figure 27 illustrates the base case grid electricity price signal used in the case study. The price signal was taken from historical LMP data for the California Independent System Operator for a node near the SVM site and then scaled to a median price of 0.04 \$/kWh based on Eq. (47). Note that the scale is saturated at 0.15 \$/kWh for visibility and high price outliers exist in the data.

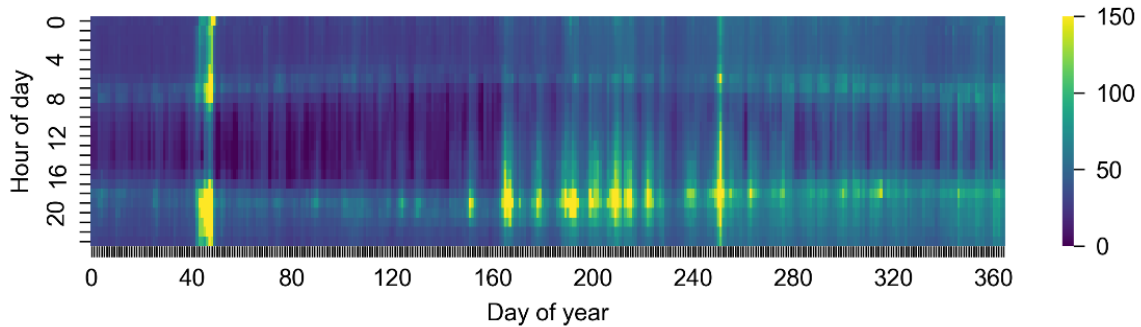


Figure 27. Base case grid electricity price signal (\$/MWh)

4.1.2 Annual Performance Analysis

For any given heat demand profile and set of component sizing parameters (e.g., CSP field and receiver capacity, PV capacity, TES capacity), a simplified hourly time-series annual performance was analyzed to estimate the hourly production from the CSP and PV technologies, TES charging/discharging, and grid electricity requirements and costs. Ideally, the Modelica system models described above would be used for this annual performance analysis; however, the simplified approach described here was initially adopted as the Modelica models were under development in parallel with this analysis. Section 4.4 describes progress toward the integration of the Modelica performance models and the techno-economic analysis.

All time-series annual performance calculations were based on 2021 solar resource data for the SVM site. The electrical energy produced by PV system ($E_{PV,el}$) was estimated using:

$$E_{PV,el} = \eta_{PV,Ref} \times \left(1 - \beta_{Ref} \times (T_{PV} - T_{Ref,STC})\right) \times I_T \times A_m \times \eta_{misc} \quad (48)$$

where $\eta_{PV,Ref}$ is the reference PV module efficiency, β_{Ref} is the temperature coefficient of the PV module, T_{PV} is the estimated PV cell temperature, $T_{Ref,STC}$ is the reference cell temperature at standard test conditions, A_m is the total area of the PV panels in the plant, and η_{misc} accounts for

miscellaneous losses including inverter and shading losses. The total solar radiation incident on the PV module (I_T) is the sum of normal and diffuse components and estimated using the equations below where DNI is the direct normal irradiance, DHI is the diffuse horizontal irradiance, β is the fixed PV module tilt angle, and θ is the time-dependent incidence angle.

$$I_{b,t} = DNI \times \cos(\theta) \quad (49)$$

$$I_{d,t} = DHI \times \frac{1 + \cos(\beta)}{2} \quad (50)$$

The electrical energy produced by the PV system was converted to thermal energy assuming a fixed heater efficiency (η_{heater}).

The CSP output was estimated based on the DNI, total heliostat reflective area (A_{hel}), time-dependent solar field optical efficiency (η_{CSP}), and an assumed fixed receiver thermal efficiency ($\eta_{rec,therm}$).

$$E_{CSP,th} = DNI \times A_{hel} \times \eta_{CSP} \times \eta_{rec,therm} \quad (51)$$

The solar field layout and efficiency were determined via NREL's SolarPILOT software. The field performance was simulated at a set of zenith and azimuth angles over the course of the year, and the field efficiency was then interpolated to an hourly time-series similar to the interpolation shown in Figure 13 and Figure 14 (page 15). As it was infeasible to fully couple the field layout and efficiency calculations to iterations over CSP capacity in the Excel-based tool, a field layout was simulated for a single CSP field/receiver thermal capacity for each scenario, and component capacities were selected assuming the same field efficiency would apply to all CSP thermal capacities considered in that scenario. This simplification does not fully account for the change in field efficiency that results from a change in CSP thermal capacity, but it is a reasonable first approximation when applied over a limited range. A more comprehensive coupling of field performance with component sizing optimization was implemented in the Python-based tool as described in Section 4.4. The CSP receiver thermal output calculated from Equation (51) was reduced in the first time period of operation after a period of zero DNI (for receiver startup) and in the last time period of operation before a period of zero DNI (for receiver shutdown) using fixed ramp rates ($t_{CSP,start}$, $t_{CSP,shutdown}$).

The available PV/heater and CSP thermal output in any hour was first used to satisfy the heat demand in that hour, and excess heat generation was used to charge thermal storage (subject to the thermal storage capacity limit). Stored thermal energy was subject to a thermal loss defined by a fixed fraction of the stored thermal capacity per hour ($f_{TES,loss}$), and thermal energy was dispatched during any time period in which insufficient PV/heater and CSP thermal output was available to meet the heat demand. Excess PV and CSP thermal output that would exceed the TES capacity was curtailed, and it provided no value to the system. In Scenarios 1, 2, and 5, the thermal storage was also charged from the grid during any hour with unused TES capacity in which the electricity price was below a given price threshold. Note that the operational strategy in these grid-charging scenarios does not give any consideration to future PV and CSP availability, and thus the model cannot choose to forego current grid-charging in favor of anticipated future PV or CSP thermal output that is expected to fill the TES capacity later in the

day. This operational simplification will likely result in underutilization of the on-site solar resources, and future work could enhance these operational strategies via forward-looking optimization approaches. This simplified annual performance model provides the $E_{th,grid}^h$ term in the LCOH calculation.

Base case operational assumptions are provided in Table 10. All CSP field design and performance parameters not specified here were set to SolarPILOT default values, and the grid-charging price cutoff shown in Table 10 is only applied to Scenarios 1, 2, 5, and 6.

Table 10. Base Case Performance Parameters

PV and Electric Heater		CSP and TES	
Parameter	Value	Parameter	Value
$\eta_{PV,Ref}$	0.216	Heliostat size	6 m x 6 m
Tilt angle	47°	$\eta_{rec,therm}$	90%
β_{Ref}	0.0034 1/K		
$T_{Ref,STC}$	25°C		
η_{misc}	0.85	$t_{CSP,start}$	12 min
η_{heater}	0.99	$t_{CSP,shutdown}$	12 min
Grid-charging price cutoff (if included)	0.02 \$/kWh	$f_{TES,loss}$	0.025% per hour

4.1.3 Component Size Selection

The CSP field, PV array, and TES capacity were sized by minimizing the calculated LCOH for each scenario, subject to constraints on the total available land area. All scenarios have the same objective and constraints but the available set of sizing variables differ (see Table 11). The selected values of the sizing variables change depending on the system technologies and configuration for each Scenario. The sizing that minimizes the calculated LCOH was found using the GRG (generalized reduced gradient) nonlinear solver tool in Excel.

The total land area A_{total} is the overall area of PV and CST tower and was estimated by:

$$A_{total} = A_{hel} \times SFLM + \frac{A_{SPV}}{GCR_{PV}} \quad (52)$$

where $SFLM$ is the solar field land multiplier which accounts for the total area of the CST tower system and is assumed a value of 1.6 with real value depending on solar field size and layout, A_{PV} is the PV total module's area and GCR_{PV} is the ground coverage ratio, which is assumed to be 0.3 based on the defaults in SAM, and A_{avail} is that total available land at SVM (250 acres).

Table 11. Overview of Optimization Problem Adopted in this Study

Scenario	System Configuration	Variables	Objective	Constraints
1	PV+CST+TES	$A_{hel}, CAP_{PV}, Cap_{TES}$	Min(LCOH)	$A_{total} \leq A_{avail}$
2	CST+TES	A_{hel}, Cap_{TES}		
3	PV+CST+TES+Grid	$A_{hel}, CAP_{PV}, Cap_{TES}$		
4	CST+TES+Grid	A_{hel}, Cap_{TES}		
5	Grid+TES	Cap_{TES}		
6	Grid	—		

4.2 Cost Uncertainties and Sensitivity Analysis

In addition to the base case cost parameters listed in Table 8 and Table 9, a sensitivity analysis was conducted to assess the influence of the capital cost of the main subsystems and the power purchase agreement (PPA) grid tariff within the ranges of these parameters shown in Table 12. Note that the system design (i.e. the sizing of the CSP field, PV array, and TES capacity) was held constant during this sensitivity analysis, and thus the results shown here do not account for potential design changes that would result from higher- and lower-cost parameters.

Table 12. Value Ranges Used to Assess Sensitivity of the SIPH Systems

Factors	Min Cost	Max Cost	Unit	Reference
SC_{hel}	60	156	\$/m ²	[17]
SC_{PV}	570	1,115	\$/kW	
$C_{tower, fixed}$	726,000	1,649,000	\$	[19]
SC_{rec}	45	163	\$/kW _{th}	[19,20]
GT_{PPA}	0.01	0.08	\$/kW	[13]

Finally, we investigated the effect of increasing the grid-independency of the system on the techno-economic feasibility. Here and for that purpose, we introduced a new parameter called renewable energy fraction (F_{RES}), which we defined as the percentage of demand met by energy from renewable energy systems either directly or via the TES. To implement this in the model, $\geq 95\%$ F_{RES} was added as a constraint in Excel Solver, implying that only 5% of the heat could be derived from grid electricity. It should be noted that such a constraint is expected to affect all the RES/TES scenarios by increasing their capacities to reduce the dependency on the grid.

4.3 Case Study and Techno-Economic Analysis Results

The SVM site was used as the basis for the case study for steam supply. The SVM facility is one of the largest carbon-dioxide emitters in California and is interested in decarbonizing its manufacturing processes. The economic competitiveness and feasibility of the SIPH applications were mainly based on the DOE cost targets for carbon-free heat by 2030. In the case study considered here, the SIPH system was designed to cover SVM’s steam demand with the following assumptions:

- Constant steam mass flow rate (\dot{m}_{steam}) is 6.3 kg/s.
- Steam is supplied at 1.034 Mpa.
- Hot steam temperature (T_h) is 260 °C.
- Cold steam temperature (T_c) is 25 °C.
- Plant operates 24/7.

The required thermal load ($D_{th,3}$) is estimated using:

$$D_{th,3} = \dot{m}_{steam}(h_h - h_c)_{steam} \quad (53)$$

where h_h and h_c are the specific enthalpy for steam at T_h and T_c respectively. $D_{th,3}$ is estimated to be 18 MW_{th}.

Sizing the SIPH system is crucial to ensure techno-economic competitiveness by minimizing the LCOH while limiting the curtailment of CSP and PV generations. The capacities of each system that minimize the calculated LCOH for each scenario are shown in Table 13. Additionally, the benefits of using the grid to charge the TES during low tariff periods are evaluated. Finally, the LCOH of the proposed configurations is benchmarked against using electrical energy to run the particle heater directly with and without TES (Scenario 5 and Scenario 6 respectively). In each case, the hot particle temperature was assumed to be 750°C for TES sizing, TES insulation, and heat exchanger sizing and cost calculations.

For the base case input parameters and electricity price signal, the CSP/TES (Scenario 4) produced the lowest calculated LCOH (0.02639 \$/kWh_{th}) to supply steam as shown in Table 13. In Scenario 4, the grid is used only for running the electrical heater during the deficiency periods. Note that the CSP capacity is provided in terms of both the heliostat field area (the design parameter used in the optimization) and the corresponding maximum thermal output from the annual calculations. The 6.3 kg/s steam flow rate specified in the case study corresponds to an 18-MWt heat demand, and thus the CSP capacity in Table 13 corresponds to a solar multiple of approximately 3.7. Scenario 4 provides 93% of the heat demand from the on-site CSP/TES resources and only relies on grid backup for the remaining 7% of demand, whereas Scenario 2 charges TES from the grid whenever the price of grid electricity falls below 0.02 \$/kWh_{th}.

The similar CSP and TES sizing selected in Scenario 2 and Scenario 4 suggest the large heliostat field and receiver size are required to minimize use of more expensive grid electricity, and that the ability to charge from low-cost grid electricity (which, for the 2021 electricity price near the SVM site, typically occurs during mid-day hours with strong solar resource) does not provide cost benefits. Nevertheless, the simplified operational strategies used in Scenario 2, which force the system to charge from the grid below the 0.02 \$/kWh_{th} price threshold can result in preferential use of grid electricity and additional CSP curtailment, and can thereby produce the slightly higher LCOH and lower F_{RES} in Table 13. The balance between large on-site resources and grid backup can be expected to be sensitive to assumptions surrounding both grid electricity price and component costs.

Table 13. Optimal Configurations of SIPH for Industrial Steam Supply Case Study

Variable	Scenario 2	Scenario 4	Scenario 5	Scenario 6
A_{hel} (m ²)	94,060	100,384	—	—
CSP capacity (MW)	63	67	—	—
CAP_{PV} (MW)	—	—	—	—
TES Duration (hours)	32.48	26.62	6	—
F_{RES} (%)	0.86	0.93	—	—
LCOH (\$/kWh _{th})	0.0264	0.0264	0.0482	0.0457

Table 13 does not include the results from Scenario 1 or Scenario 3. In these scenarios, the system was allowed to include a PV array; however, the solver reduced the PV capacity to zero in order to minimize LCOH and thereby replicated the results of Scenario 2 and Scenario 4. These results are sensitive to the relative PV and CSP costs and are, in part, a result of aggressive CSP cost assumptions relative to current costs. Figure 28 illustrates sensitivity of LCOH to PV, CSP, and TES capacities (assuming fixed CSP field efficiency) at the base case cost assumptions (Table 8 and Table 9) and at reduced PV costs.

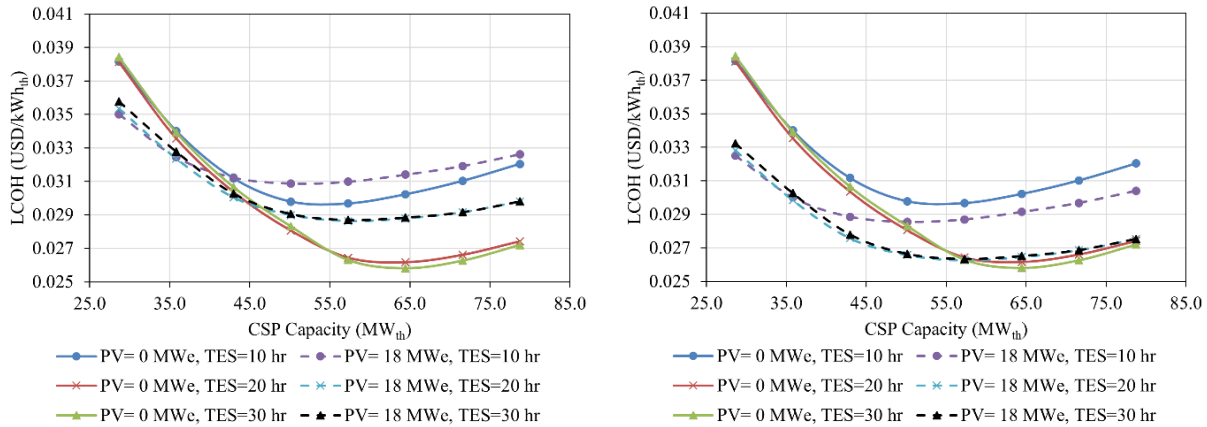


Figure 28. Sensitivity of LCOH to CSP, TES, and PV sizing for (a) base case cost assumptions and (b) reduced PV capital cost (570 \$/kWe)

As mentioned in Section 4.1.1, the base case capital costs used here do not account for contingency, EPC cost, or sales tax and thus may underestimate the true LCOH. If a 7% contingency cost, 13% EPC cost, and 5% sales tax on 80% of the total direct cost are included in the capital cost (based on default values from NREL’s SAM Version 2022.11.21 CSP molten salt power tower case), the LCOH for Scenario 4 in Table 13 rises from 0.029 \$/kWh_{th} to 0.0326 \$/kWh_{th}.

Looking at the cost breakdown of the SIPH system for Scenario 4 in Figure 29, more than 64% of the total cost is associated with the solar receiver and heliostat field costs. Grid electricity costs over the 25-year lifetime of the plant represent 17.25% of the total capital costs. TES accounts for only 9.1% of the capital expenditure despite a large TES capacity (26.62 hours), owing to the low cost of particle TES relative to traditional molten salt or other storage

technologies. The lower cost of particle TES facilitates the economic viability of the large TES capacity needed to support a high capacity factor.

The largest energy drawn from the grid is during winter as illustrated in Figure 30. In the winter months, the selected system sizing is insufficient to support full 24/7 operation during partially cloudy conditions and the system must commonly rely on grid backup during overnight hours, while in the summer, grid electricity is only required during prolonged periods of abnormally poor solar resource. However, the selected system sizing is sensitive to the assumed price signal as the LCOH minimization balances the capital cost of on-site CSP, PV, and TES components against the cost of grid backup. Higher assumed grid electricity prices would result in larger sizing of on-site resources.

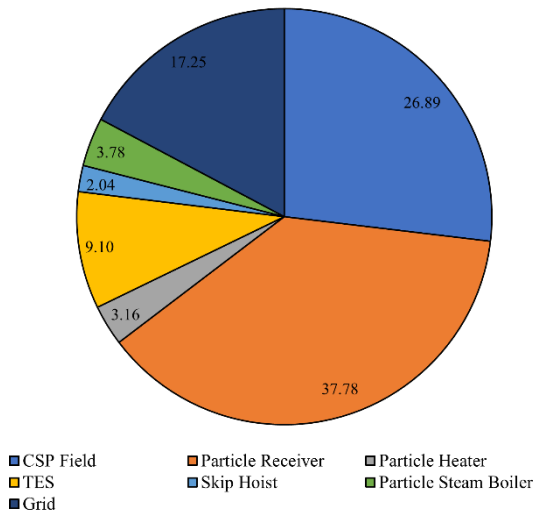


Figure 29. Cost breakdown of optimal CSP/ TES (Scenario 4) SIPH subsystems required for industrial steam supply case study

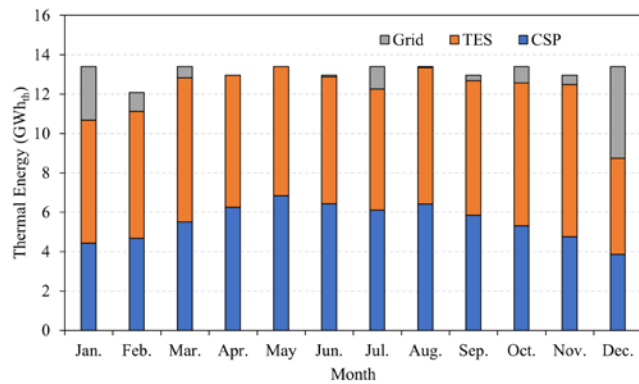


Figure 30. Monthly thermal energy delivered by the energy sources in the optimal CSP/ TES (Scenario 4) SIPH system designed for industrial steam supply case study

Figure 31 and Figure 32 shows the possible change in LCOH of a SIPH system for industrial steam supply based on cost reductions or cost increases in various components.

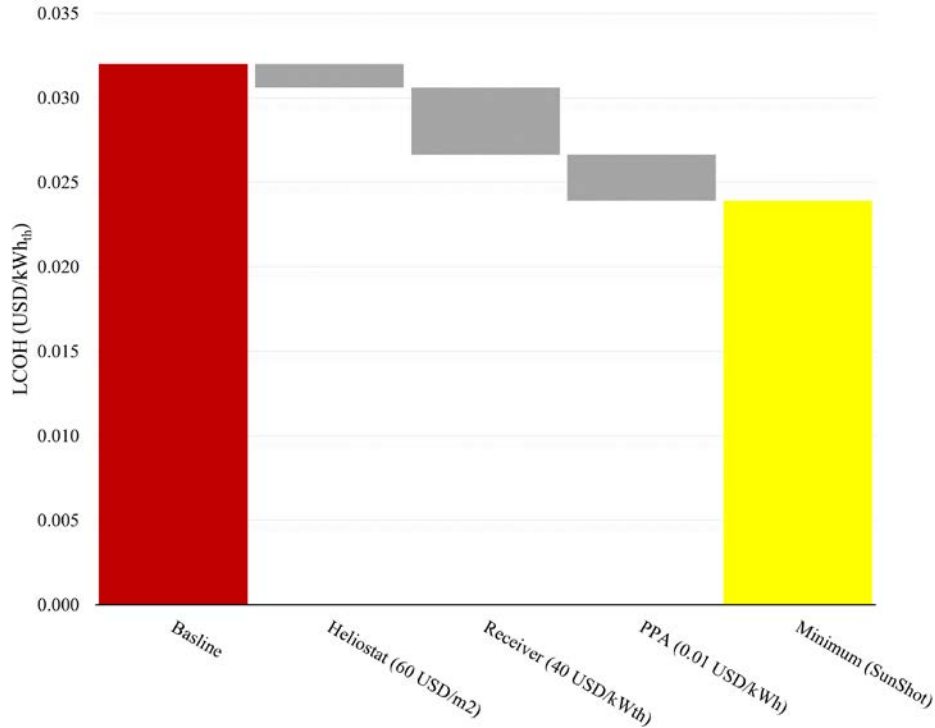


Figure 31. Potential reduction in the LCOH of the optimal CSP/ TES (Scenario 4) SIPH system designed for industrial steam supply case study

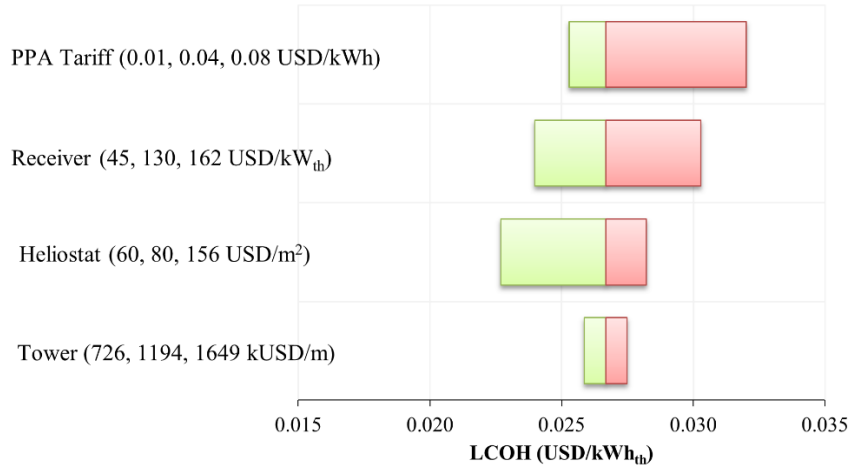


Figure 32. Sensitivity of the LCOH of the optimal CSP/ TES (Scenario 4) SIPH system designed for industrial steam supply case study to the variation in main economic parameters

4.4 Model Integration

The techno-economic analysis described in Sections 4.1–4.3 employed a simplified annual performance analysis designed to quickly estimate annual grid backup requirements based on the sizing of the CSP, PV, and TES components. Component sizing was selected to minimize LCOH for each scenario; however, coupling solar field design/efficiency calculations to the Excel-based tool was manually cumbersome and required simplifications described in Section 4.1.2. The computed LCOH is sensitive to numerous parameters, including component costs, grid

electricity prices, thermal demand, and others, with substantial uncertainty and variation between potential SIPH sites and future grid scenarios.

A Python-based modeling approach that can fully automate connections between models was developed to (1) facilitate evaluation of numerous potential cost scenarios that would be cumbersome to evaluate within the Excel-based tool and (2) expand the particle SIPH techno-economic analysis capability to include the Modelica performance models, established financial models in NREL’s SAM [21], established open-source optimization packages in Python, and automated sensitivity analysis across ranges of performance and cost model input parameters. The current setup only includes the case study for industrial steam supply described in Section 4.3; however, additional SIPH use cases could be included in the future.

Figure 33 is a flowchart of the capabilities and data flow for the improved features enabled through the integration within Python. This techno-economic analysis tool enables design assessment of the system, including both high-level sizing parameters (e.g., storage duration) and detailed component parameters (e.g., storage insulation). The techno-economic analysis tool uses the Python API for SolarPILOT (CoPylot) [22][23] for all solar field layout and efficiency calculations, interacts with the Modelica system model through a functional mock-up unit that can be executed via an open-source Python package (pyfmi), calculates component costs using the cost functions presented in Section 4.1.2, and connects with established SAM financial models via PySAM. Options were included to use either the annual performance calculated by the Modelica model or the annual performance from the simplified analysis described in Section 4.1.2, and to use either financial models from SAM or the simplified LCOH calculation described in Section 4.1. Finally, the tool was integrated with custom code to automate sensitivity analysis (using either user-defined sets of variable levels or random sampling based on Latin Hypercube or Monte Carlo methods) and optimization of system sizing parameters using an open-source Python optimization package (scikit-optimize).

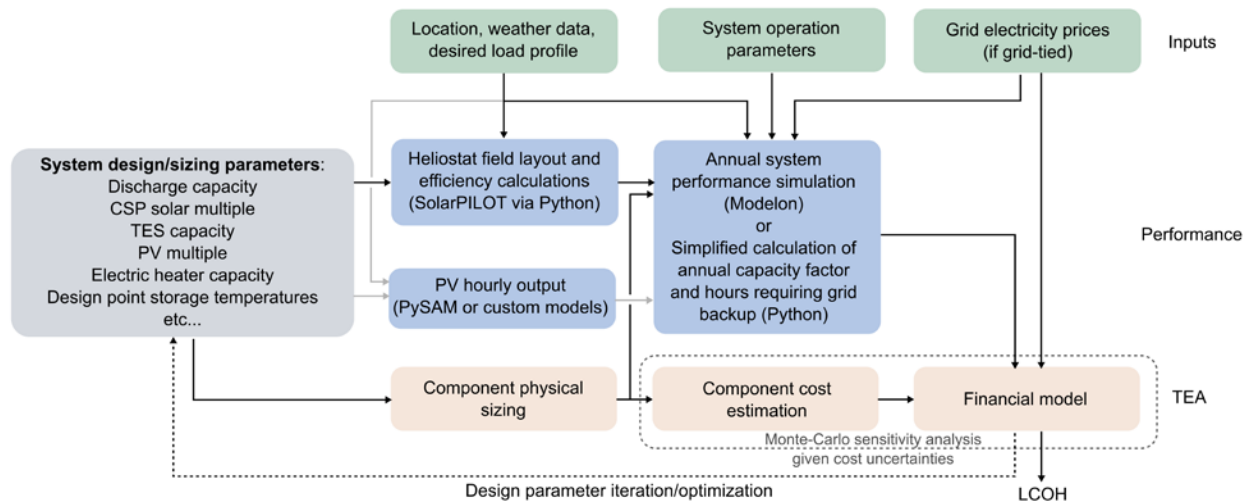


Figure 33. System analysis flow chart for enhancing system modeling capabilities

Figure 34 is an example of results from the Modelica annual performance model (evaluated through the Python framework described in Figure 33) based on the system sizing from Scenario 4 in Table 13.

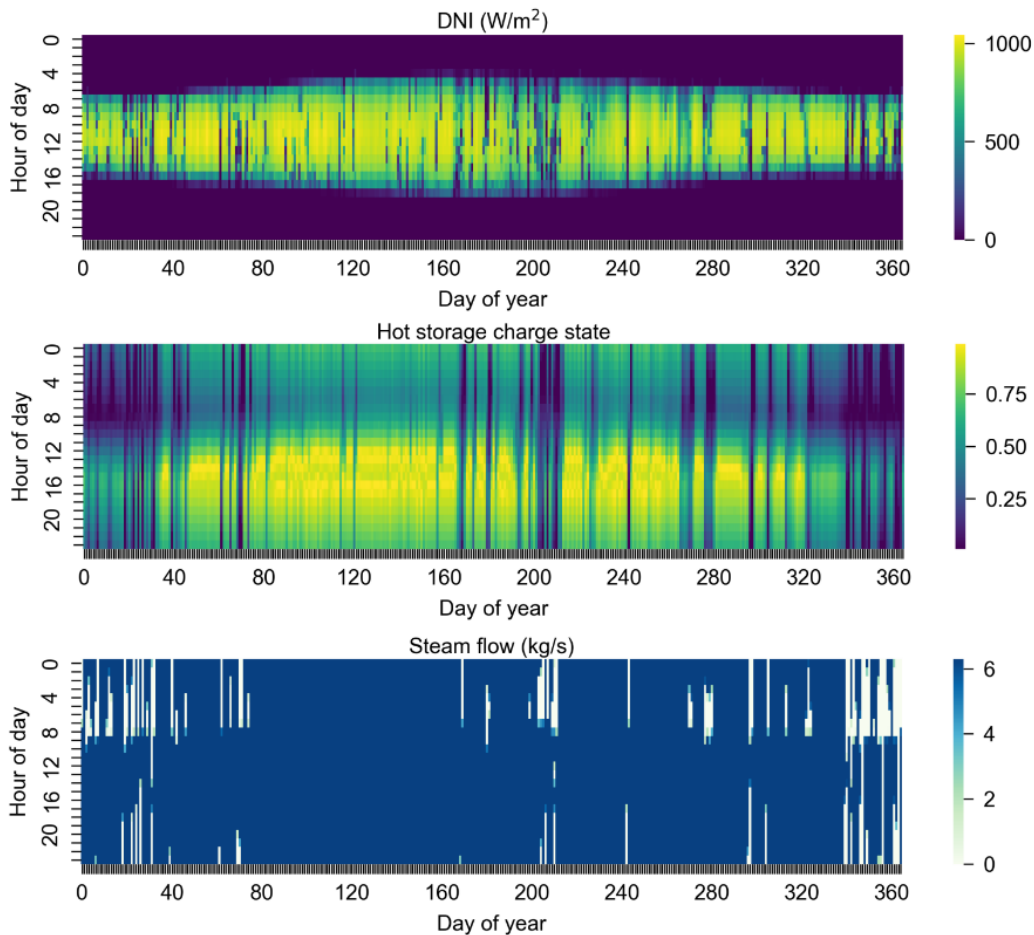


Figure 34. Example of results from the Modelica annual performance model run through the Python framework in Figure 33 with the system sizing from Scenario 4 in Table 13

The variable time-step results from the Modelica model were averaged into hourly arrays and Figure 34 shows the hourly-average DNI, hot storage charge state (as a fraction of total hot storage capacity), and steam flow rate before grid backup. The Modelica model does not currently explicitly simulate grid backup, and time periods with zero steam flow in Figure 34 are those in which grid electricity would be required to fulfill the steam demand.

Figure 35 provides an example sensitivity analysis evaluated via the Python code over ranges of CSP solar multiple (the ratio of CSP thermal capacity to the heat demand), thermal storage capacity, and PV solar multiple (PV SM, defined here as the ratio of the PV electrical capacity to the heat demand). In these calculations, the heliostat field layouts and field efficiencies were reevaluated for each unique heliostat field capacity via automated connection with SolarPILOT via the CoPylot API. Calculations were compared for the simplified annual analysis and LCOH calculation defined in Section 4.1 (Figure 35a), the simplified annual analysis coupled with the LCOH calculated using the SAM Single Owner financial model (Figure 35b), and the Modelica annual performance analysis coupled with the SAM Single Owner financial model (Figure 35c).

As expected, differences in annual performance analysis methodologies and financial analysis methodologies produced differences in calculated LCOH; however, similar trends are observed in each case and would lead to CSP, TES, and PV sizing selection similar to that shown in Section 4.3.

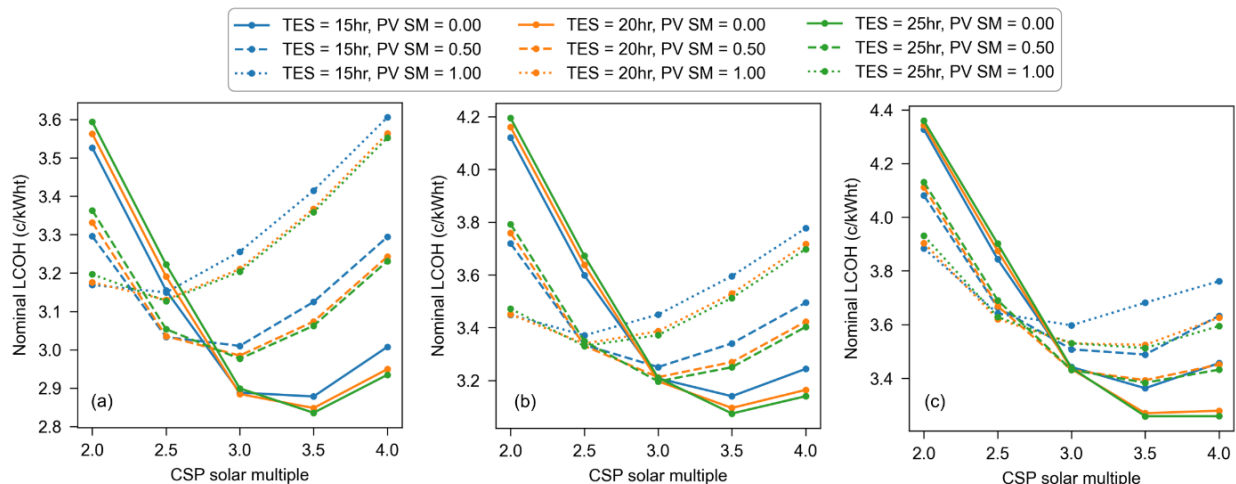


Figure 35. Example of sensitivity analysis using similar cost inputs as shown in Figure 28(b): (a) simplified annual analysis and LCOH calculation as shown in Section 4.1, (b) simplified annual analysis and LCOH from the SAM Single Owner financial model, and (c) Modelica annual performance analysis and LCOH from the SAM Single Owner financial model

Figure 36 is an example of system sizing optimization over three independent variables (CSP solar multiple, TES capacity, and PV multiple) using Bayesian optimization via the `gp_minimize` algorithm in the open-source Python package `scikit-optimize`. All model cost and performance inputs were identical to those used in Figure 35(c), and the calculation was based on the Modelica annual performance model coupled to the SAM Single Owner financial model. The objective function sought to minimize the calculated LCOH, and the Bayesian optimization algorithm was first initiated from a set of 10 randomly sampled sets of independent variable values and then allowed 20 subsequent iterations to improve on the best objective function value. Optimization algorithms designed for computationally expensive objective functions were selected because each objective function evaluation involves receiver tower height optimization, field layout, field efficiency calculations at a large set of zenith/azimuth angles, and annual performance simulation via the Modelica performance model. Figure 36(a) illustrates the progression of the best simulated objective function (LCOH) value after each iteration, while Figure 36(b–d) illustrate the sampled values of each of the independent variables with the initial randomly sampled values shown in black and the values tested by the optimizer shown in blue.

Though the example sensitivity analysis and optimization only explored high-level system sizing variables, the code can be used to iterate calculations on any input variable to the model, including for example location, heat demand, cost inputs, electricity price signals, financial model assumptions, and heliostat characteristics. Additional development is needed to (1) improve consistency between the physical component sizing and component performance in the Modelica performance model and the component cost functions, (2) improve system optimization performance, memory utilization, and computational efficiency, and (3) expand the calculations for SIPH use cases beyond the industrial steam supply case study described in

Section 4.3. Also, future SIPH development could consider expanding the tool to use recent developments in SolarPILOT specifically for falling particle receiver designs, integrating a future SAM particle CST SIPH performance model as an option for annual analysis, integrating dispatch optimization models that can more rigorously select operational strategies to minimize use and cost of grid electricity, and refining the Modelica model with additional component details and control strategies.

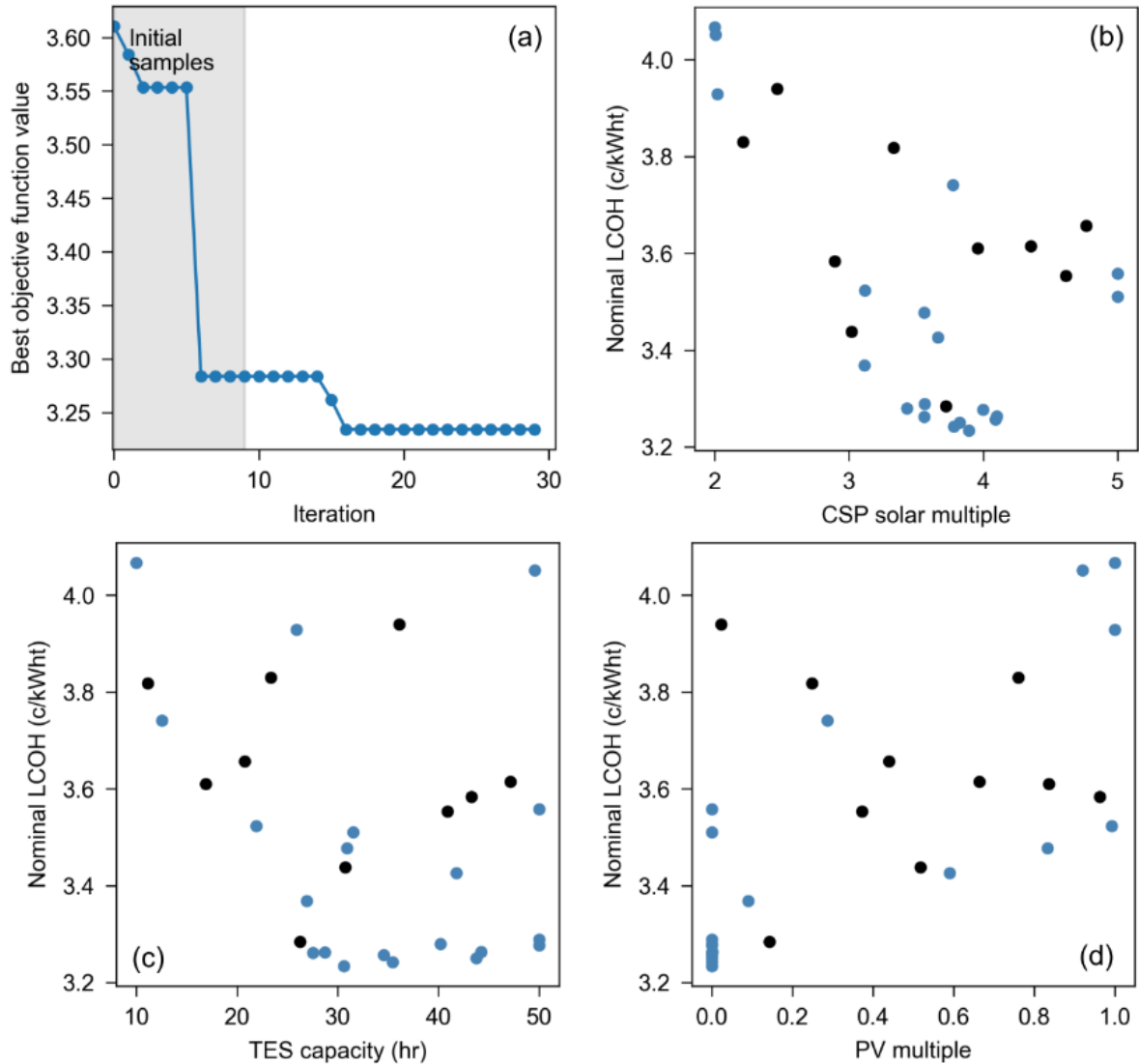


Figure 36. Example of optimization results using the same models and conditions as Fig. 35(c)

5 Conclusion

Industrial processes are diverse, can vary significantly for each plant, and impose challenges to standardize renewable integration and energy supply. To this end, we develop a thermal energy storage system as a uniform platform based on the Heat Exchanger and Thermal Energy Reservoir (HEATER) system to integrate renewable energy for SIPH applications. A modeling tool has been developed to assess the system configuration and economic potential. The modeling tool is based on commercial software Modelon Impact, with customized components of charging/discharging devices and particle-based thermal energy storage. With the component libraries in the Modelon Impact software, the modeling tool provides sufficient flexibility to adapt to various SIPH application for practical scenarios.

This project developed particle TES system configurations and modeling tools to support reliable industrial process heat from renewable energy (i.e., HEATER for SIPH). The particle TES using low-cost and stable silica sand as a storage medium can provide a wide temperature range and can integrate with renewable sources including CST, PV, and wind power to supply reliable carbon-free heat and power. The particle TES system and modeling tools could provide a low-cost TES solution integrated with renewable energy to reduce carbon emissions from a wide range of industrial processes currently heavily relying on fossil fuels.

The project developed a modeling tool based on Modelon Impact software for the particle TES system including charging/discharging heat exchangers integrated with a CSP system for SIPH supply relevant to an NREL IP portfolio including a solar particle receiver, heat exchangers, and the particle TES storage system. The project team works closely in bringing the particle TES technology to commercial use. Significant findings, conclusions, or developments that this project accomplished include:

- Completed Modelon Impact-Modelica models on key components of particle TES, charging devices of both particle receiver integration with CST and PV electric charge heater, and discharge PFB HX for hot air and particle/steam boiler.
- Performed model validation based on high-fidelity models or prior validated results.
- Developed an industry case study based on Searles Valley Minerals mining processes for supplying steam to eliminate coal by solar energy.
- Collaborated with Alumina Energy, Modelon Impact, and Babcock & Wilcox on industry applications, software tool development, and original equipment manufacturers.

6 References

- [1] U.S. Environmental Protection Agency, 2020, “Industry Sector Emissions” [Online]. Available: <https://www.epa.gov/ghgemissions/sources-greenhouse-gas-emissions#industry>. [Accessed: 01-Apr-2022].
- [2] U.S. Department of Energy, 2022, “Industrial Decarbonization Roadmap,” (September).
- [3] Schoeneberger, C. A., McMillan, C. A., Kurup, P., Akar, S., Margolis, R., and Masanet, E., 2020, “Solar for Industrial Process Heat: A Review of Technologies, Analysis Approaches, and Potential Applications in the United States,” *Energy*, **206**, p. 118083.
- [4] Modelon Impact, 2021, “Modelon Impact.”
- [5] Modelica Association, 2021, “Modelica Language” [Online]. Available: <https://modelica.org/modelicalanguage.html>.
- [6] Fu, Y., Zuo, W., Wetter, M., VanGilder, J. W., and Yang, P., 2019, “Equation-Based Object-Oriented Modeling and Simulation of Data Center Cooling Systems,” *Energy Build.*, **198**, pp. 503–519.
- [7] Fan, C., Hinkelman, K., Fu, Y., Zuo, W., Huang, S., Shi, C., Mamaghani, N., Faulkner, C., and Zhou, X., 2021, “Open-Source Modelica Models for the Control Performance Simulation of Chiller Plants with Water-Side Economizer,” *Appl. Energy*, **299**, p. 117337.
- [8] Scott, P., Alonso, A. de la C., Hinkley, J. T., and Pye, J., 2017, “SolarTherm: A Flexible Modelica-Based Simulator for CSP Systems,” p. 160026.
- [9] Hinkelman, K., Wang, J., Zuo, W., Gautier, A., Wetter, M., Fan, C., and Long, N., 2022, “Modelica-Based Modeling and Simulation of District Cooling Systems: A Case Study,” *Appl. Energy*, **311**, p. 118654.
- [10] Schirck, J., Ma, Z., and Morris, A., 2023, “Discrete Element Modeling of a Particle Heater for Energy Storage Systems,” *Powder Technol.*, **414**, p. 118084.
- [11] Ma, Z., and Martinek, J., 2018, “Analysis of Solar Receiver Performance for Chemical-Looping Integration with a Concentrating Solar Thermal System,” *Proceedings of the ASME 2018 Power and Energy Conference PowerEnergy2018, Lake Buena Vista, Florida, USA, Lake Buena Vista, Florida, USA*.
- [12] Martinek, J., Wendelin, T., and Ma, Z., 2018, “Predictive Performance Modeling Framework for a Novel Enclosed Particle Receiver Configuration and Application for Thermochemical Energy Storage,” *Sol. Energy*, **166**(April), pp. 409–421.
- [13] Ma, Z., Wang, X., Davenport, P., Gifford, J., and Martinek, J., 2022, “Preliminary Component Design and Cost Estimation of a Novel Electric-Thermal Energy Storage System Using Solid Particles,” *J. Sol. Energy Eng.*, **144**(3).

- [14] Ziegler, M. S., Mueller, J. M., Pereira, G. D., Song, J., Ferrara, M., Chiang, Y. M., and Trancik, J. E., 2019, “Storage Requirements and Costs of Shaping Renewable Energy Toward Grid Decarbonization,” *Joule*, **3**(9), pp. 2134–2153.
- [15] Al-Ghussain, L., Darwish Ahmad, A., Abubaker, A. M., and Hassan, M. A., 2022, “Techno-Economic Feasibility of Thermal Storage Systems for the Transition to 100% Renewable Grids,” *Renew. Energy*, **189**, pp. 800–812.
- [16] California ISO Open Access Same-time Information System (OASIS), “Locational Marginal Prices (LMP).”
- [17] Solar Energy Technologies Office, U. D. of E. (DOE), 2021, “2030 Solar Cost Targets.”
- [18] Davenport, P., Martinek, J., and Ma, Z., 2019, “Analysis of Concentrating Solar Thermal System to Support Thermochemical Energy Storage or Solar Fuel Generation Processes,” *ASME 2019 13th International Conference on Energy Sustainability*, American Society of Mechanical Engineers.
- [19] González-Portillo, L. F., Albrecht, K. J., Sment, J., Mills, B., and Ho, C. K., 2022, “Sensitivity Analysis of the Levelized Cost of Electricity for a Particle-Based Concentrating Solar Power System,” *J. Sol. Energy Eng. Trans. ASME*, **144**(3), pp. 1–8.
- [20] Ho, C. K., 2016, “A Review of High-Temperature Particle Receivers for Concentrating Solar Power,” *Appl. Therm. Eng.*, **109**, pp. 958–969.
- [21] System Advisor Model Version 2022.11.21 (SAM 2022.11.21). National Renewable Energy Laboratory. Golden, CO. [Sam.Nrel.Gov](http://sam.nrel.gov) .
- [22] Wagner, M. J., and Wendelin, T., 2018, “SolarPILOT: A Power Tower Solar Field Layout and Characterization Tool,” *Sol. Energy*, **171**, pp. 185–196.
- [23] Hamilton, W. T., Wagner, M. J., and Zolan, A. J., 2022, “Demonstrating SOLARPILOT’s Python Application Programmable Interface Through Heliostat Optimal Aimpoint Strategy Use Case,” *J. Sol. Energy Eng. Trans. ASME*, **144**(3), pp. 1–7.

Appendix SIPH Case Studies

This appendix includes additional results on industrial process heat case studies for reference. *Note that results in the appendix are preliminary for understanding various configurations but have not been validated.*

A.1. Case Definitions

In the main content of the report, we listed the SVM case with steam supply. In this project, we also investigated supplying hot particles, hot air, and steam/power cogeneration for industry applications, and we analyzed their levelized cost of [energy/electricity] based on four charge the configurations in Figure 23 (page 30) and three discharge configurations in Figure 24 and six scenarios listed in Table 6 (page 34). In the particle heating case, we used bauxite calcination as an example as Case Study 1 (CS1). We also studied hot air supply as CS2, and cogeneration for CS4 in addition to the steam supply (CS4) in the main part of the report.

A.1.1. Bauxite Calcination (CS1)

As with any emerging energy technologies, SIPH may not be immediately cost-effective in all industry sectors. However, certain applications can be promising with both economic and environmental benefits. One such applications is bauxite mining to produce alumina for aluminum production. Here we investigate the techno-economic feasibility of SIPH in bauxite calcination assuming:

- Specific energy consumption of 4 GJ/ton Alumina
- Alumina annual production of 200,000 ton
- Calcination temperature (T_h) of 1,100°C
- Cold particle temperature (T_c) of 25°C
- Bauxite specific heat capacity (Cp_{part}) of 1.045 kJ/kgK
- 24/7 plant operation.

The thermal load needed for the calcination process ($D_{th,1}$) for this case study is around 25.4 MW_{th} and hence the solar tower system capacity is sized to match this demand.

$$D_{th,1} = \dot{m}_{air} c_{p,bauxite} (T_h - T_c)_{bauxite} \quad (54)$$

A.1.2. Industry Hot Air Supply (CS2)

NREL developed heating air by a direct air/particle contact PFB HX technology in the ARPA-E DAYS program and proved it is a feasible technology. This case study assess a SIPH system for hot air supply with the following assumptions adopted from [15]:

- Constant air mass flow rate is 50 kg/s.
- Air is supplied at 1.5 Mpa.
- Hot air temperature (T_h) is 300°C.
- Cold air temperature (T_c) is 27 °C.

- Plant operates 24/7.

The required thermal load in this case study ($D_{th,2}$) is estimated using:

$$D_{th,2} = \dot{m}_{air}(h_h - h_c)_{air} \quad (55)$$

where h_h and h_c are the specific enthalpy for air at T_h and T_c respectively. $D_{th,2}$ is estimated to be 13.93 MW_{th}.

A.1.3. Cogeneration (CS4)

The cogeneration case study (CS4) matches the current heat and power SVM requirements. The SVM's SIPH system must generate 150,000 pph (pounds per hour) (18.9 kg/s) of superheated steam 24/7. This steam load can be broken down further to meet the specific needs of the SVM facility:

- 50,000 pph (6.3 kg/s) of 150 psi (10.34 bar) saturated steam used for heating
- 100,000 pph (12.6 kg/s) of superheated steam at 220 psi (15.17 bar) and approximately 260°C used to drive steam turbines that drive Ammonia compressors.

If the two products cannot be provided efficiently, the SIPH system can provide the full steam load (i.e., 150,000 pph) at the superheated condition of 220 psi and 260°C. In this case study, we focused on a SIPH system that delivers the single product of superheated steam at the conditions outlined. This full steam load is approximately 55 MW_{th} assuming the boiler feedwater comes in at 25°C.

Here, SIPH covers SVM's steam demand for heating and for electricity production (via a simple Rankine cycle) with the following assumptions:

- Constant steam mass flow rate (\dot{m}_{steam}) at 18.9 kg/s
 - 6.3 kg/s saturated steam for heating
 - 12.6 kg/s superheated steam for power generation
- Steam supplied at 1.034 Mpa for heating and at 1.517 Mpa power generation
- Hot steam temperature (T_h) of 260 °C
- Cold steam temperature (T_c) of 25 °C
- 24/7 plant operation.

The required thermal load ($D_{th,4}$) is estimated using:

$$D_{th,4} = \dot{m}_{steam}(h_h - h_c)_{steam} \quad (56)$$

where h_h and h_c are the specific enthalpy for steam at T_h and T_c respectively. $D_{th,4}$ is estimated to be 53.71 MW_{th}.

A.2. Parametric Sensitivity Ranges

In addition to the sensitivity analysis presented in the main part of the report, the LCOH was estimated with a 90% confidence level using Monte Carlo analysis with the following uncertainties [20] and assuming a normal distribution for the parameters:

- Capital cost $\pm 15\%$
- Operation and maintenance cost $\pm 5\%$
- Output energy $\pm 15\%$
- Discount rate $\pm 20\%$
- Lifespan $\pm 20\%$
- Power purchase agreement tariff $\pm 5\%$.

Finally, we investigated the effect of increasing the grid-independency of the system on the techno-economic feasibility. Here and for that purpose, we introduced a new parameter called renewable energy fraction (F_{RES}), which we defined as the percentage of demand met by energy from renewable energy systems either directly or via the TES. To implement this in the model, $\geq 95\% F_{RES}$ was added as a constraint in Excel Solver. It should be noted that such a constraint is expected to affect all the RES/TES scenarios by increasing their capacities to reduce the dependency on the grid.

A.3. Results

A.3.1. CS1: Bauxite Calcination

In this industrial application, the bauxite particles are used as the TES media, which are heated in the particle solar receiver and/or the electric heater depending on the availability of the energy from different sources and the scenario. Sizing the SIPH system is crucial to ensure techno-economic feasibility of the system by minimizing the LCOH and reducing the curtailment periods. The optimal capacities of each system in each configuration are shown in Table A-1. Additionally, the benefits of using the grid to charge the TES during low tariff periods are evaluated. Finally, the LCOH of the proposed configurations is benchmarked against using electrical energy to run the particle heater directly with and without TES (Scenario 5 and Scenario 6 respectively).

Table A-1. Optimal Configurations of SIPH for Bauxite Calcination Case Study

Variable	Scenario 2	Scenario 4	Scenario 5	Scenario 6
CAP_{CST} (MWth)	90	96	—	—
CAP_{PV} (MW)	0	0.00	—	—
TES Duration (hours)	39	38	7	—
TES Capacity (MWhth)	1,000	970	178	—
LCOH (USD/kWhth)	0.0243	0.0245	0.0473	0.0452
F_{RES} (%)	86.69	93.59	—	—

The results presented in Table A-1 indicate the CSP/TES system (Scenario 2) is the best SIPH configuration for the bauxite calcination case study with an LCOH of 0.0243 USD/kWh_{th} where the grid will be used to run the electrical heater as backup and to charge the TES during low tariff periods. Nevertheless, this LCOH of the best configuration is promising and more attractive than the LCOH if the thermal demand is met by the grid-powered heater. Note that Table A-1 does not include the results from Scenario 1 or Scenario 3. In these scenarios, the system was allowed to include a PV array; however, the solver reduced the PV capacity to zero in order to minimize LCOH and thereby replicated the results of Scenario 2 and Scenario 4 respectively. These results are sensitive to the PV and CSP costs and are, in part, a result of aggressive CSP cost assumptions relative to current costs.

The cost breakdown of the SIPH in Figure A-1 shows that about one-third of the total cost is associated with the particle receiver, which is followed by the cost of the CSP field; the electricity purchased from the grid throughout the system’s lifespan represents almost 22% of the total cost. As expected, the largest energy drawn from the grid is during winter as illustrated in Figure A-2, and the least energy is drawn from April through August; coincidentally, the months of reduced grid demand for backup coincide with months of higher node prices. The detailed sizing as well as the capital cost of each component are presented in Table A-2.

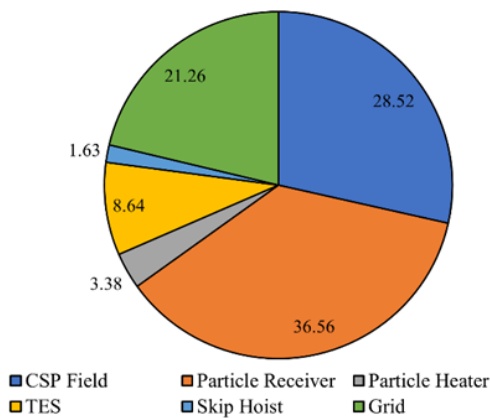


Figure A-1. Cost breakdown of optimal CSP/TES (Scenario 2) SIPH subsystems required for bauxite calcination case study

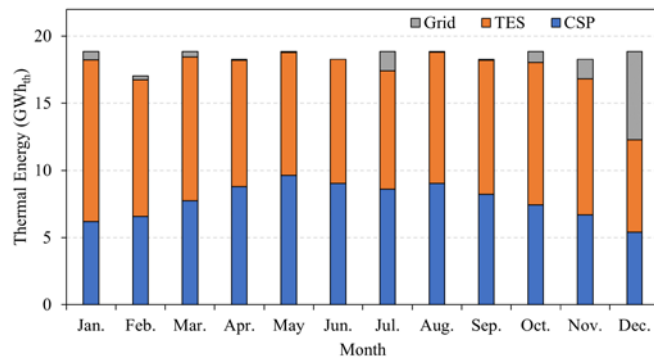


Figure A-2. Monthly thermal energy delivered by the energy sources in the optimal CSP/TES (Scenario 2) SIPH system designed for bauxite calcination case study

Table A-2. Overview of the Optimal CSP/TES (Scenario 2) SIPH Subsystems Sizing and Capital Costs

Component	Subcomponent	Capacity	Unit	Cost (USD)
CSP field	N/A	90.07	MW _{th}	11,207,000
Particle receiver	Receiver	70.04	m ²	11,168,300
	Tower	79.35	m	3,194,000
Particle heater	Heating wire	50.74	MW _{th}	1,076,000
	Insulation material			14,800
	Refractory material			17,488

Component	Subcomponent	Capacity	Unit	Cost (USD)
	Estimated control box			3,000,000
TES	Silo containment	2,898.40	ton	1,732,000
	Insulation material			1,665,000
	Media			—
Skip hoist	N/A	165.51	kg/s	639,910.92
Grid electricity	N/A	For 25 years	N/A	8,354,532.92
Total Estimated Equipment Cost (USD)				32,000,000

We also investigated the potential of reducing the LCOH of the optimal configuration by implementing U.S. Department of Energy (DOE) target solar costs in 2030 as shown in Figure A-3. The DOE thermal energy LCOH target (<0.02 USD/kWh_{th}) may be achievable if component cost reduction goals are realized. Additionally LCOH is most sensitive to the PPA tariff and is followed by the sensitivity factors of the heliostat and receiver costs as shown in Figure A-4.

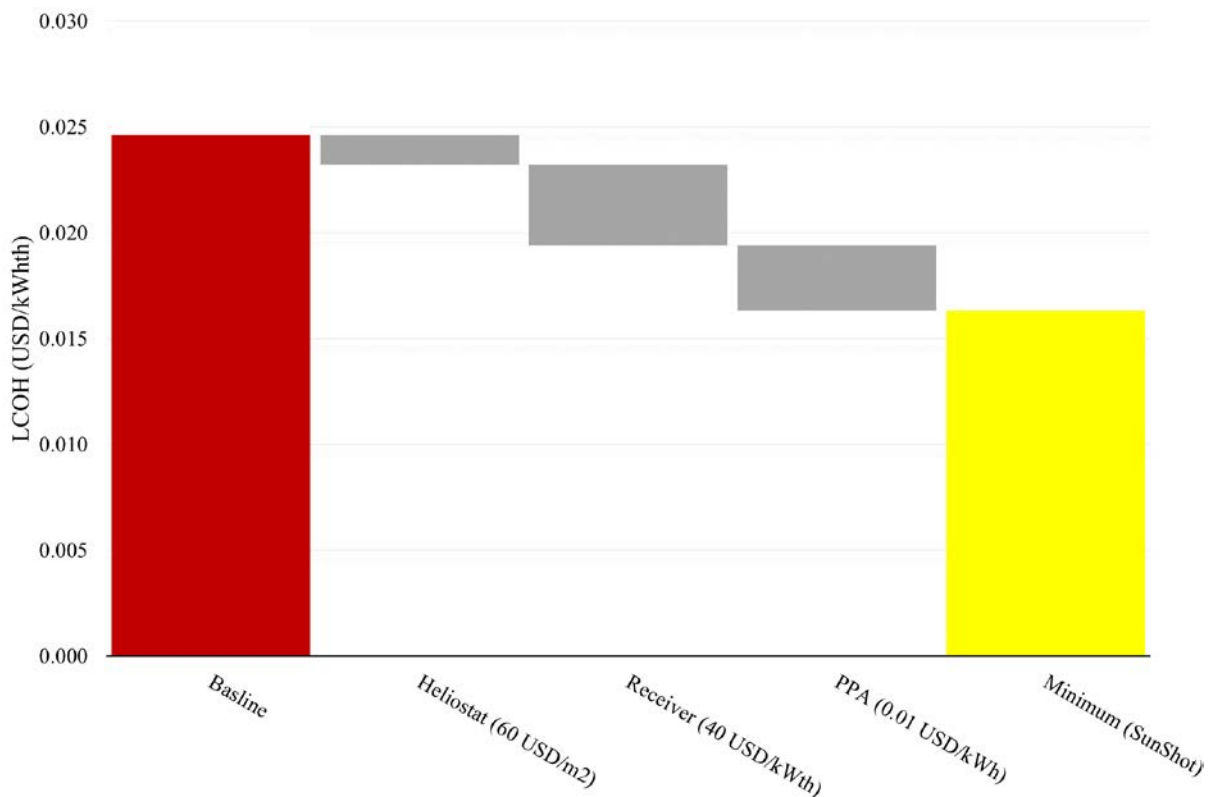


Figure A-3. Potential reduction in the LCOH of the optimal CSP/TES (Scenario 2) SIPH system designed for bauxite calcination case study

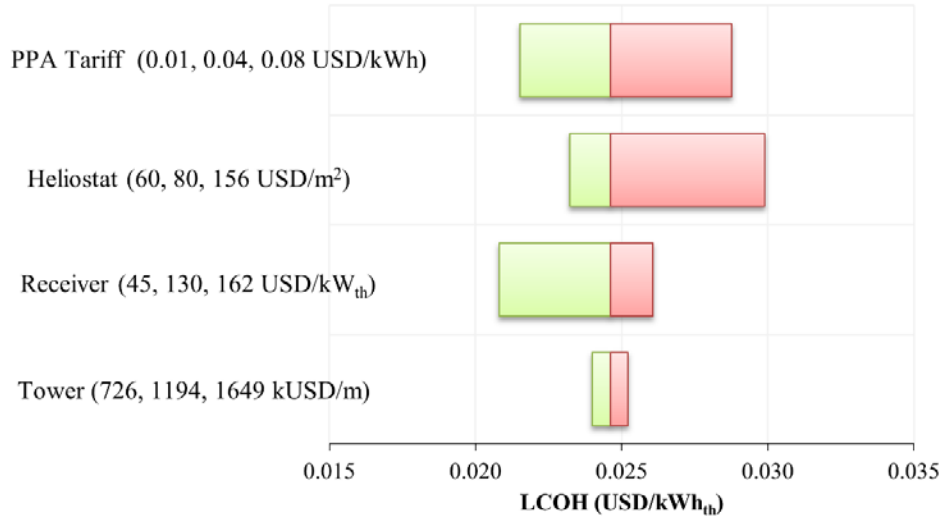


Figure A-4. Sensitivity of the LCOH of the optimal CSP/TES (Scenario 2) SIPH system designed for bauxite calcination case study to the variation in main economic parameters

Using the uncertainties associated with the economic parameters and the Monte Carlo analysis, the minimum LCOH is 0.0250 USD/kWh_{th} (with 90% confidence) with baseline costs and belonging to the CSP/TES configuration (Scenario 4). Using the DOE targeted costs for 2030, the minimum LCOH (with 90% confidence) drops to 0.0224 USD/kWh_{th} and also belongs to the CSP/TES (Scenario 4).

Finally, we investigated maximizing the independency of the SIPH on the utility grid by introducing a new constraint into the optimization—that the amount of demand covered by the grid does not exceed 5% of the total demand. The results of this investigation are presented in Table A-3.

Table A-3. Optimal Configurations of SIPH for Bauxite Calcination Case Study with the Grid Dependency Constraint (<5%)

Variable	Scenario 1	Scenario 2	Scenario 3	Scenario 4
CAP_{CST} (MW _{th})	87	101	92	100
CAP_{PV} (MW)	26	0	25	0
TES duration (hours)	27	40	27	40
TES capacity (MWh _{th})	690	1,010	682	1,020
LCOH (USD/kWh _{th})	0.0271	0.0245	0.0270	0.0245
F _{RES} (%)	96.3	95.0	96.8	95.1

The optimal SIPH system is the CSP/TES system (either Scenario 2 or Scenario 4) for which the lowest LCOH is 0.0245 USD/kWh_{th}, which is slightly higher than the lowest LCOH found previously (without the grid independency constraint; i.e., in the baseline case). This is because the optimal configuration in the baseline case already achieves high independency (around 87%) and hence small increase in the RES/TES capacities is required to meet the 95% independency constraint.

A.3.2. CS2: Industrial Hot Air Supply

The optimal capacities for each configuration for supplying industrial hot air using the SIPH system are shown in Table A-4. Similar to the bauxite calcination case study, CSP/TES (Scenario 2) would be the best SIPH configuration to supply hot air as shown in Table A-4, and the lowest LCOH (0.0317 USD/kWh_{th}) is where the grid is used to run the electrical particle heater during deficit periods and during low tariff periods to charge the TES. The LCOH of the best configuration is more promising and attractive if the thermal demand is met by the grid-powered heater or if the grid is used with TES alone (i.e., Scenario 5 and Scenario 6). Table A-4 does not include the results from Scenario 1 and Scenario 3. In these scenarios, the system was allowed to include a PV array; however, the solver reduced the PV capacity to zero in order to minimize LCOH and thereby replicate the results of Scenario 2 and Scenario 4. These results are sensitive to the relative PV and CSP costs and are, in part, a result of aggressive CSP cost assumptions relative to current costs.

Table A-4. Optimal Configurations of SIPH for Industrial Hot Air Supply Case Study

Variable	Scenario 2	Scenario 4	Scenario 5	Scenario 6
CAP_{CST} (MWth)	48.54	52.60	—	—
CAP_{PV} (MW)	—	—	—	—
TES Duration (hours)	36.17	28.59	6	—
TES Capacity (MWhth)	509.52	402.75	84.53	—
LCOH (USD/kWhth)	0.0317	0.0320	0.050	0.0457
F_{RES} (%)	84.92	92.05	—	—

As shown in Figure A-5, almost 50% of the total cost is associated with the CSP system and is followed by grid costs. As expected, the most energy is drawn from the grid during winter as illustrated in Figure A-6 and the least is drawn during summer. The detailed sizing and the capital cost of each component are presented in Table A-5.

Furthermore, similar to the first case study, we investigated the potential of reducing the LCOH of the optimal configuration by implementing DOE target solar costs in 2030; the results are of that investigation are shown in Figure A-7. They show (1) the minimum achievable LCOH is higher than the DOE thermal energy LCOH target and (2) LCOH is most sensitive to the PPA tariff, which is followed by the heliostat and receiver costs as shown in Figure A-8.

Moreover, the minimum LCOH of 0.0326 USD/kWh_{th} (with 90% confidence) belongs to CSP/TES configuration (Scenario 2) when the baseline costs are used. With the DOE targeted costs, the minimum LCOH with 90% confidence drops to 0.024 USD/kWh_{th}, and it also belongs to the CSP/TES (Scenario 2).

Table A-5. Overview of Optimal CSP/TES (Scenario 2) SIPH Subsystems Sizing and Capital Costs

Component	Subcomponent	Capacity	Unit	Cost (USD)
CSP Field	N/A	48.54	MW _{th}	5,584,808
Particle Receiver	Receiver	34.91	m ²	6,019,427
	Tower	65.39	m	2,686,254
Particle Heater	Heating wire	28.18	MW _{th}	597,103
	Insulation material			8,220
	Refractory material			9,712
	Control box			123,007
TES	Silo containment	15,881.10	ton	2,694,932
	Insulation material			108,517
	Media			555,839
Skip Hoist	N/A	664.24	kg/s	3,281,300
PFB HX	FBPV	6.06	MW _e	43,640
	HX			571,815
	Cyclone			8,527
	Piping			20,277
Grid Electricity	N/A	For 25 years	-	5,539,942
Total Estimated Equipment Cost (USD)				22,314,000

Finally, again, increasing the independence of the SIPH from the grid by introducing the same 5% constraint into the optimization was investigated. The results of this investigation are presented in Table A-6. The best configuration was again Scenario 1 with an LCOH of 0.0323 USD/kW_{hth}.

Table A-6. Optimal Configurations of SIPH for Industrial Hot Air Supply Case Study With the Grid Dependency Constraint (<5%)

Variable	Scenario 1	Scenario 2	Scenario 3	Scenario 4
CAP_{CST} (MW _{th})	46	72	46	56
CAP_{PV} (MW)	21	—	15	—
TES duration (hours)	27	44	22	43
TES capacity (MW _{hth})	384	613	310	601
LCOH (USD/kW _{hth})	0.0323	0.0376	0.0324	0.0324
F _{RES} (%)	95	95	95	95

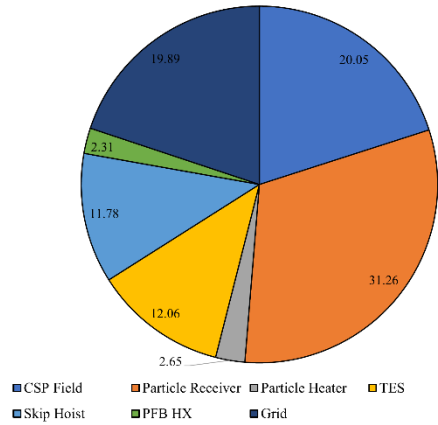


Figure A-5. Cost breakdown of optimal CSP/TES (Scenario 2) SIPH subsystems required for industrial hot air supply case study

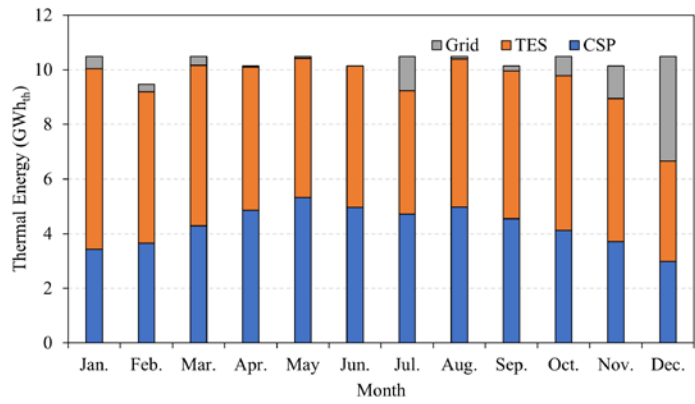


Figure A-6. Monthly thermal energy delivered by the energy sources in the optimal CSP/TES (Scenario 2) SIPH system designed for industrial hot air supply case study

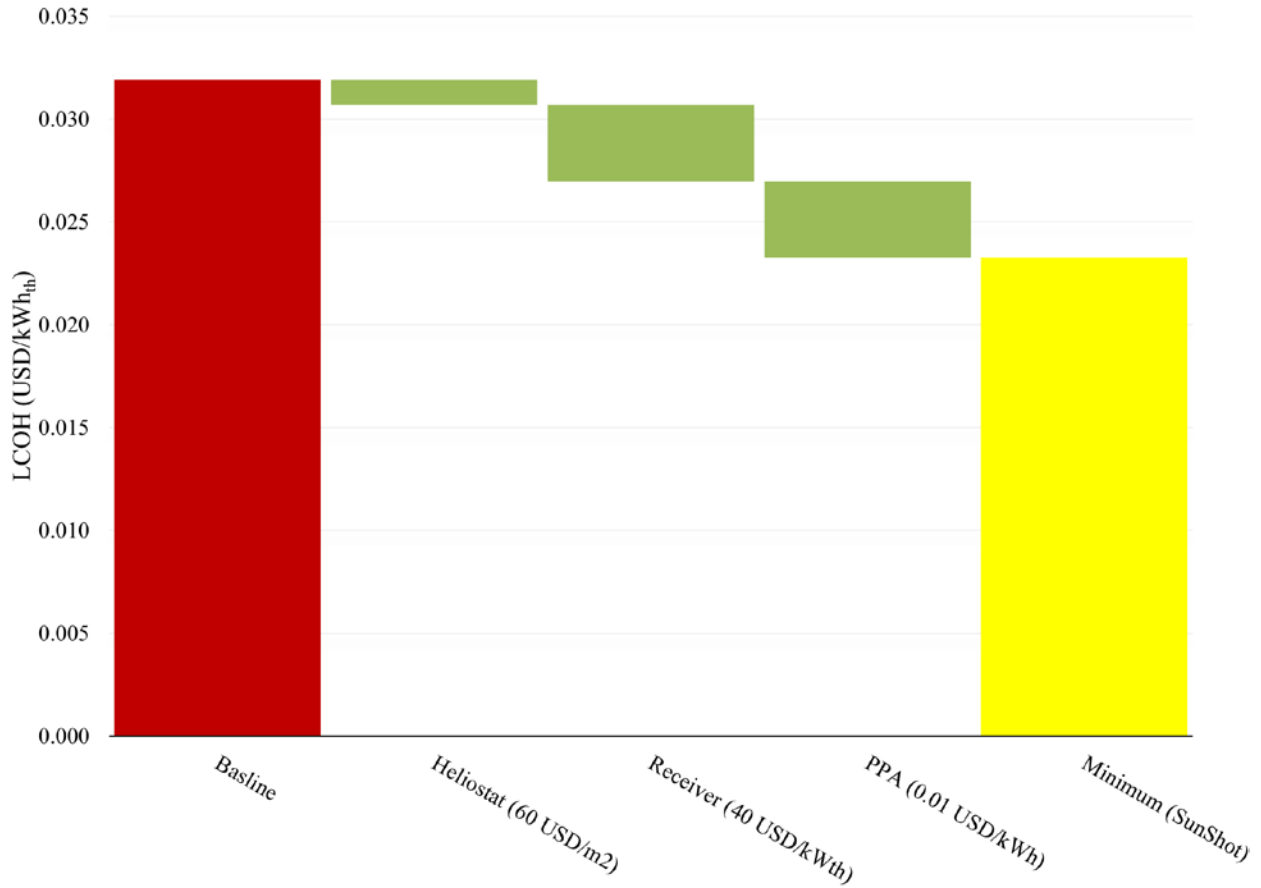


Figure A-7. Potential reduction in the LCOH of the optimal CSP/TES (Scenario 2) SIPH system designed for industrial hot air supply case study

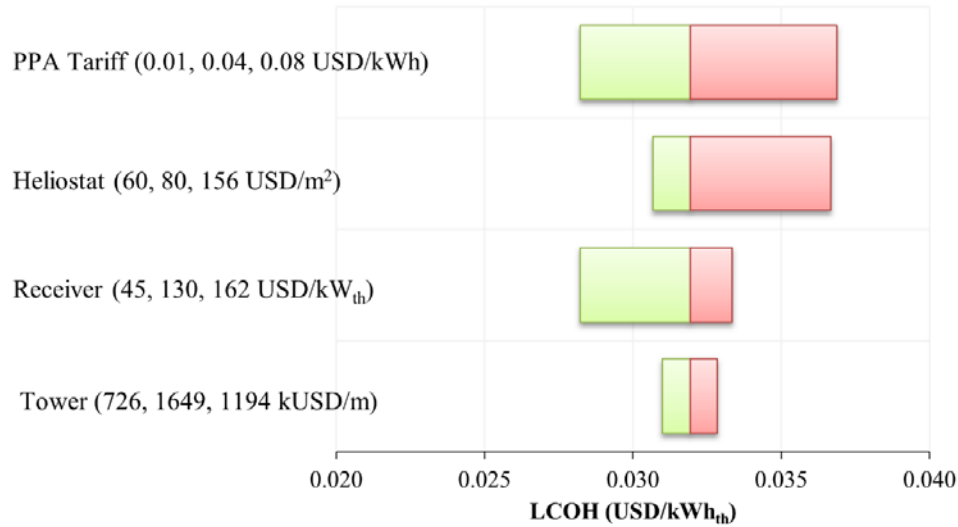


Figure A-8. Sensitivity of the LCOH of the optimal CSP/TES (Scenario 2) SIPH system designed for industrial hot air supply case study to the variation in main economic parameters

A.3.3. CS4: Cogeneration

The optimal capacities for SIPH systems that provide combined heat and power are shown in Table A-7. Similar to the previous case studies, CSP/TES (Scenario 2) would be the best SIPH configuration to supply steam with the lowest LCOH (0.0256 USD/kW_{th}) where the grid will be used only as backup. Similarly, the LCOH dropped compared to the hot air SIPH despite the additional steam generator cost due to the increase in the amount of energy utilized from the CSP/TES (Scenario 2) system to cover the demand. Table A-7 does not include the results from Scenario 1 or Scenario 3. In these scenarios, the system was allowed to include a PV array; however, the solver reduced the PV capacity to zero to minimize LCOH and thereby replicated the results of Scenario 2 and Scenario 4. These results are sensitive to the relative PV and CSP costs and are, in part, a result of aggressive CSP cost assumptions relative to current costs.

Table A-7. Optimal Configurations of SIPH for Cogeneration Case Study

Variable	Scenario 2	Scenario 4	Scenario 5	Scenario 6
CAP_{CST} (MW _{th})	190	207	—	—
CAP_{PV} (MW)	—	—	—	—
TES Duration (hours)	37	30	7	—
TES Capacity (MW _{th})	1,978	1,625	377	—
LCOH (USD/kW _{th})	0.0256	0.0258	0.0485	0.0457
F _{RES} (%)	86.2	92.9	—	—

The cost breakdown of the SIPH in Figure A-9 shows that more than 50% of the total cost is associated with the CSP system followed grid costs. Like the previous case studies and as expected, the largest energy drawn from the grid is during winter as illustrated in Figure A-10

whereas the lowest are during summer: the grid provided almost 14% of the total annual energy demand.

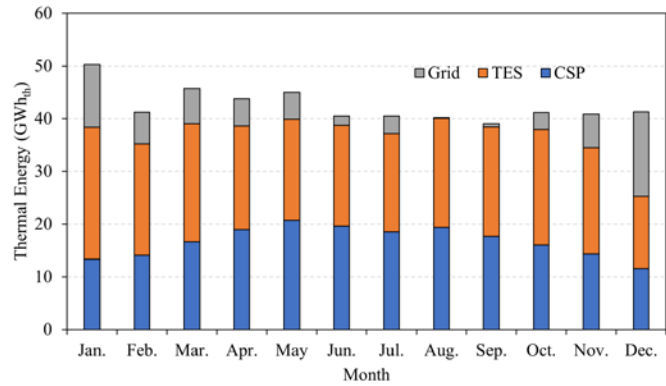
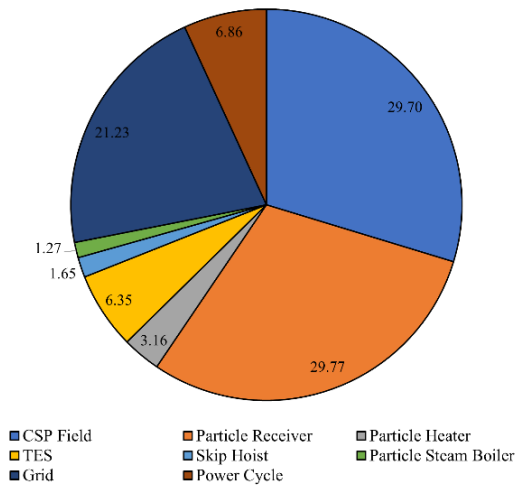


Figure A-9. Cost breakdown of optimal CSP/TES (Scenario 2) SIPH subsystems required for cogeneration case study

Figure A-10. Monthly thermal energy delivered by the energy sources in the optimal CSP/TES (Scenario 2) SIPH system designed for cogeneration

Figure A-11 shows that the minimum achievable LCOH meets the DOE thermal energy LCOH target (<0.02 USD/kW_{th}) based on the future solar costs. The detailed sizing as well as the capital cost of each component are presented in Table A-8.

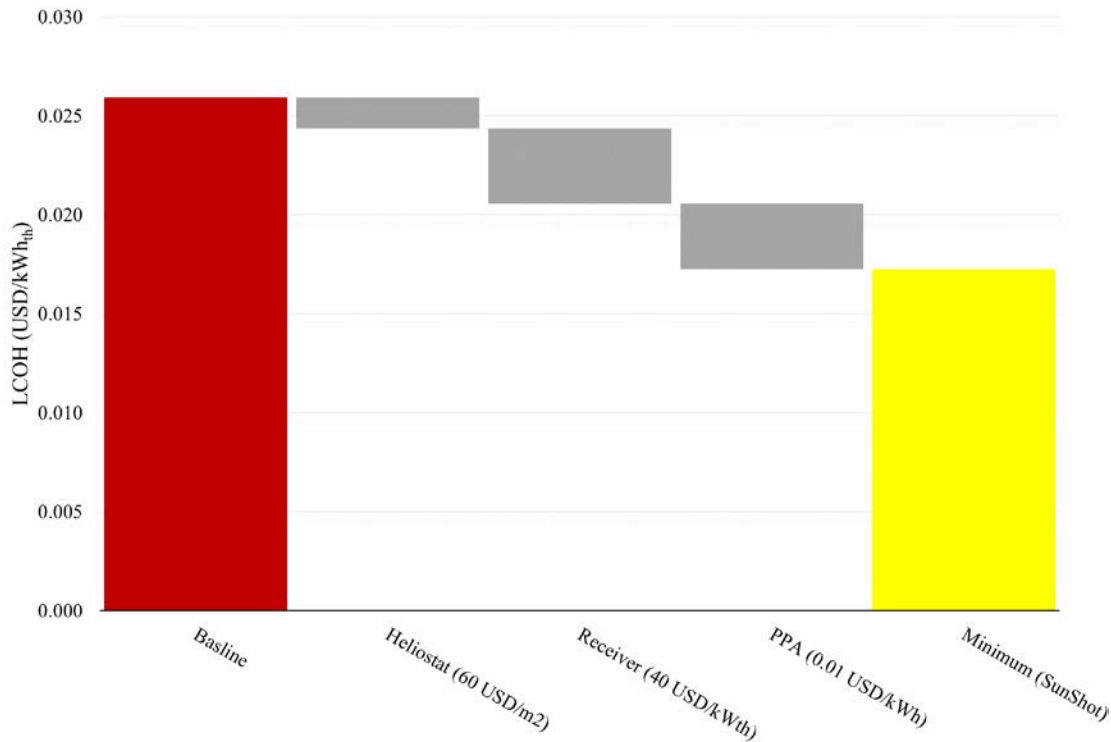


Figure A-11. Potential reduction in the LCOH of the optimal CSP/TES (Scenario 2) SIPH system designed for cogeneration case study

Table A-8. Optimal CSP/TES (Scenario 2) SIPH Subsystems Sizing and Capital Costs

Component	Subcomponent	Capacity	Unit	Cost (USD)
CSP Field	N/A	189.74	MW _{th}	26,474,950
Particle Receiver	Receiver	165.47	m ²	23,527,880
	Tower	74.54	m	3,008,932
Particle Heater	Heating wire	107.61	MW _{th}	2,280,376
	Insulation material			31,390
	Refractory material			37,089
	Control Box			469,771
TES	Silo containment	11,207.1	ton	2,461,428
	Insulation material			2,809,480
	Media			392,250
Skip Hoist	N/A	372.20	kg/s	1,474,981
Particle Steam Boiler	U-tube HX	35.19	m ²	1,129,404
Power Cycle Cost	N/A	8.21	MWe	6,116,104
Grid Electricity	N/A	For 25 years	N/A	18,924,368
Total Estimated Equipment Cost (USD)				70,214,050

The LCOH of the cogeneration SIPH system is most sensitive to the heliostat cost, which is followed by the PPA grid tariff and receiver cost as shown in Figure A-12. Moreover, the minimum LCOH, 0.0269 USD/kWh_{th}, with 90% confidence belongs to CSP/TES configuration (Scenario 2) with the baseline costs. With the DOE targeted costs, the minimum LCOH with 90% confidence drops to 0.0175 USD/kWh_{th} and belongs to the CSP/TES (Scenario 2).

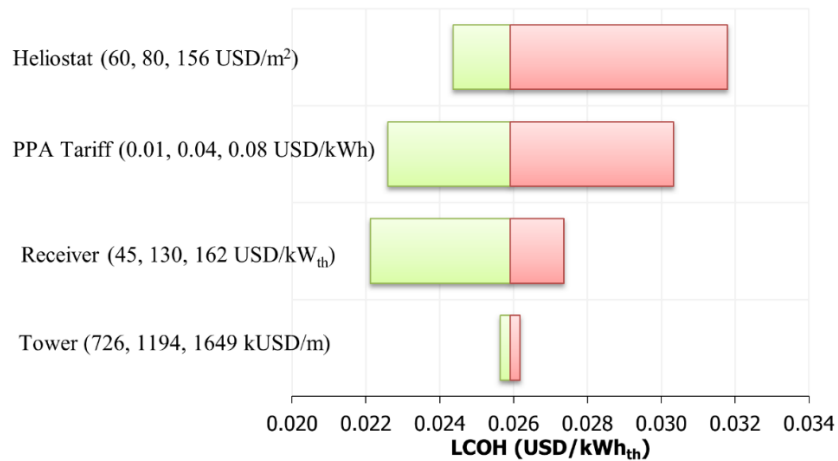


Figure A-12. Sensitivity of the LCOH of the optimal CSP/TES (Scenario 2) SIPH system designed for cogeneration case study to the variation in main economic parameters

In addition, the base analysis presented thus far, the effect of oversizing the power cycle for the cogeneration case was investigated. The oversized power cycle was used to generate additional

electricity and sold to the grid The results of this investigation are illustrated in Figure A-13. It can be concluded that oversizing the power cycle is beneficial and would decrease the LCOH for all scenarios up to 200% oversizing. After this point, further increases in the energy delivered (and the associated profit from selling the excess electricity) are outweighed by the increase in the capital cost of the power cycle.

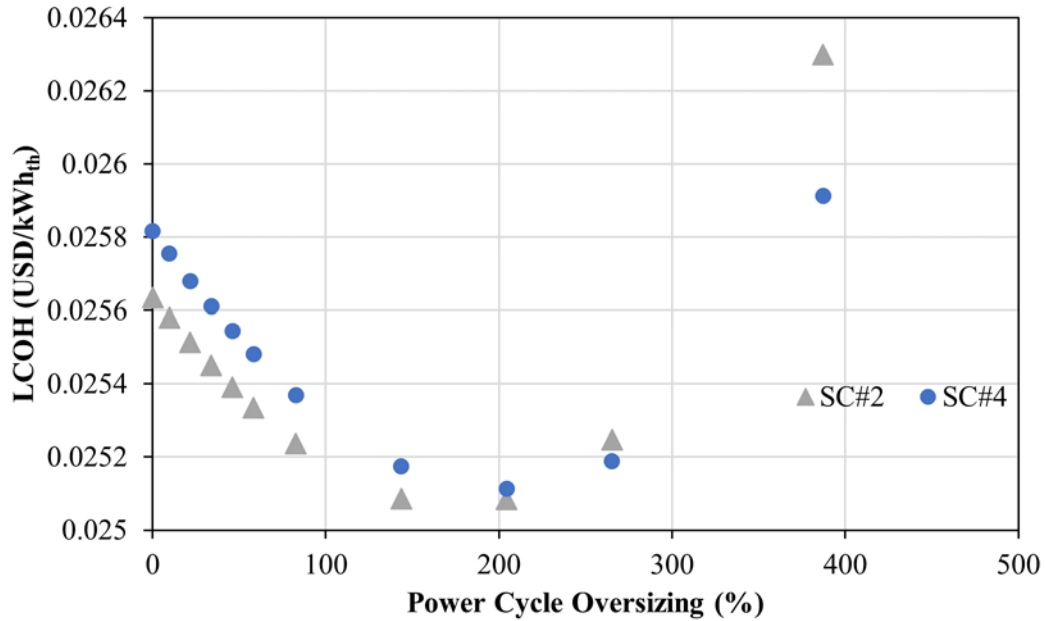


Figure A-13. Effect of oversizing the power cycle on the LCOH of the optimal configurations